

Advances in Civil Engineering

Advanced Optimization Techniques and Their Applications in Civil Engineering

Lead Guest Editor: Tayfun Dede

Guest Editors: Ravipudi V. Rao, Vedat Toğan, Moacir Kripka, and Victor Yepes





Advanced Optimization Techniques and Their Applications in Civil Engineering

Advances in Civil Engineering

Advanced Optimization Techniques and Their Applications in Civil Engineering

Lead Guest Editor: Tayfun Dede

Guest Editors: Ravipudi V. Rao, Vedat Togan, Moacir Kripka,
and Victor Yepes



Copyright © 2018 Hindawi. All rights reserved.

This is a special issue published in “Advances in Civil Engineering.” All articles are open access articles distributed under the Creative Commons Attribution License, which permits unrestricted use, distribution, and reproduction in any medium, provided the original work is properly cited.

Editorial Board

- José Aguiar, Portugal
Shaikh F. U. Ahmed, Australia
Maria Cruz Alonso, Spain
Serji N. Amirkhonian, USA
P. Ch. Anastasopoulos, USA
V. G. M. Annamdas, Singapore
Pedro Arias-Sánchez, Spain
Farhad Aslani, Australia
Chiara Bedon, Italy
Rafik Belarbi, France
Hugo C. Biscaia, Portugal
Giosuè Boscato, Italy
Melina Bosco, Italy
Alberto Campisano, Italy
Francesco Canestrari, Italy
Robert Černý, Czech Republic
Constantin Chalioris, Greece
Noel Challamel, France
Daniel W.M. Chan, Hong Kong
Edwin H W Chan, Hong Kong
Carlos Chastre, Portugal
Ghassan Chehab, Lebanon
Francesco Colangelo, Italy
Ottavia Corbi, Italy
Mario D'Aniello, Italy
Jorge de Brito, Portugal
Gianmarco de Felice, Italy
Stefano de Miranda, Italy
Angelo Di Egidio, Italy
Luigi Di Sarno, Italy
Ahmed Elghazouli, UK
Flora Faleschini, Italy
Antonio Formisano, Italy
- Giovanni Garcea, Italy
Elhem Ghorbel, France
Agathoklis Giaralis, UK
Rodrigo Gonçalves, Portugal
Arturo Gonzalez, Ireland
Kirk Hatfield, USA
Khandaker Hossain, Canada
Dong-Sheng Jeng, Australia
Thibaut Lecompte, France
Eul-Bum Lee, Republic of Korea
Dongsheng Li, China
Li Li, Canada
Sui Pheng Low, Singapore
Lyan-Ywan Lu, Taiwan
Eric Lui, USA
Lorenzo Macorini, UK
Yann Malecot, France
John Mander, USA
Giuseppe Carlo Marano, Italy
Fabio Mazza, Italy
Ahmed Mebarki, France
Shazim A. Memon, Kazakhstan
Hossein Moayedi, Iran
Fabrizio Mollaioli, Italy
Rosario Montuori, Italy
Ayman S. Mosallam, USA
Roberto Nascimbene, Italy
Giuseppe Oliveto, Italy
Alejandro Orfila, Spain
Togay Ozbakkaloglu, Australia
Alessandro Palmeri, UK
Fabrizio Paolacci, Italy
Arnaud Perrot, France
- Christophe Petit, France
Giuseppe Piccardo, Italy
Prodromos Psarropoulos, Greece
Giuseppe Quaranta, Italy
Carlo Rainieri, Italy
Damien Rangedard, France
Dimitris Rizos, USA
Geoffrey W. Rodgers, New Zealand
Hugo Rodrigues, Portugal
Hamid Reza Ronagh, Australia
Pier Paolo Rossi, Italy
Lukasz Sadowski, Poland
Anna Saetta, Italy
Evangelos J. Sapountzakis, Greece
Halil Sezen, USA
M. Shahria Alam, Canada
Sanjay Kumar Shukla, Australia
Stefano Sorace, Italy
Flavio Stochino, Italy
Claudio Tamagnini, Italy
Yaya Tan, China
Patrick W.C. Tang, Australia
Yinshan Tang, UK
Filippo Ubertini, Italy
Humberto Varum, Portugal
Cumaraswamy Vipulanandan, USA
Roman Wan-Wendner, Austria
Wei-Chau Xie, Canada
Michael Yam, Hong Kong
Libo Yan, Germany
Victor Yepes, Spain
Mariano Angelo Zanini, Italy
Annan Zhou, Australia

Contents

Advanced Optimization Techniques and Their Applications in Civil Engineering

Tayfun Dede , Moacir Kripka , Vedat Toğan, Victor Yepes , and Ravipudi V. Rao
Editorial (2 pages), Article ID 5913083, Volume 2018 (2018)

Data-Driven Decision-Making in the Design Optimization of Thin-Walled Steel Perforated Sections: A Case Study

Zhi-Jun Lyu , Qi Lu , YiMing Song, Qian Xiang, and Guanghui Yang
Research Article (14 pages), Article ID 6326049, Volume 2018 (2018)

Pseudodynamic Bearing Capacity Analysis of Shallow Strip Footing Using the Advanced Optimization Technique “Hybrid Symbiosis Organisms Search Algorithm” with Numerical Validation

Arijit Saha , Apu Kumar Saha, and Sima Ghosh
Research Article (18 pages), Article ID 3729360, Volume 2018 (2018)

Optimum Design of Braced Steel Space Frames including Soil-Structure Interaction via Teaching-Learning-Based Optimization and Harmony Search Algorithms

Ayse T. Daloglu , Musa Artar , Korhan Ozgan , and Ali İ. Karakas 
Research Article (16 pages), Article ID 3854620, Volume 2018 (2018)

Development of Future Rule Curves for Multipurpose Reservoir Operation Using Conditional Genetic and Tabu Search Algorithms

Anongrit Kangrang , Haris Prasanchum, and Rattana Hormwichian
Research Article (10 pages), Article ID 6474870, Volume 2018 (2018)

The Optimization of Calcareous Fly Ash-Added Cement Containing Grinding Aids and Strength-Improving Additives

Gökhan Kaplan , Sadık Alper Yildizel , Selçuk Memiş , and Ali Uğur Öztürk
Research Article (9 pages), Article ID 8917059, Volume 2018 (2018)

Optimal Cement Mixtures Containing Mineral Admixtures under Multiple and Conflicting Criteria

Nitza M. García, Hildéliz L. Soto-Toro , Mauricio Cabrera-Ríos, and Oscar Marcelo Suárez 
Research Article (10 pages), Article ID 3780810, Volume 2018 (2018)

Editorial

Advanced Optimization Techniques and Their Applications in Civil Engineering

Tayfun Dede ¹, **Moacir Kripka** ², **Vedat Toğan**,¹ **Victor Yepes** ³ and **Ravipudi V. Rao**⁴

¹Department of Civil Engineering, Karadeniz Technical University, 61080 Trabzon, Turkey

²Department of Civil Engineering, Universidade de Passo Fundo, 99001-970 Passo Fundo, RS, Brazil

³ICITECH, Department of Construction Engineering, Universitat Politècnica de València, Camino de Vera s/n, 46022 Valencia, Spain

⁴Department of Mechanical Engineering, Sardar Vallabhai National Institute of Technology, Gujarat 395007, India

Correspondence should be addressed to Tayfun Dede; tayfundede@gmail.com

Received 17 May 2018; Accepted 19 May 2018; Published 25 June 2018

Copyright © 2018 Tayfun Dede et al. This is an open access article distributed under the Creative Commons Attribution License, which permits unrestricted use, distribution, and reproduction in any medium, provided the original work is properly cited.

Nowadays, a rapid growth of computer performance enables and encourages new developments in civil engineering as well as related areas. For instance, the construction industry investigates new designs with minimum cost, minimum CO₂ emissions, or embodied energy, among other objectives. Applications of optimization techniques are most exciting, challenging, and of truly large scale when it comes to the problems of civil engineering in terms of both quality and quantity. In order to overcome the difficulties, researchers are interested in advanced optimization techniques. The aim of this special issue is to collect the studies using optimization algorithms in civil engineering problems such as structural engineering, construction management, and environmental engineering.

During the call for submissions, many papers were received and some of them were later withdrawn or rejected. The other 6 papers were accepted. The details about the published papers are given below.

The paper written by A. Saha, A. K. Saha, and S. Ghosh presents an upper-bound solution for bearing capacity of shallow strip footing considering composite failure mechanisms by the pseudodynamic approach. In this study, the authors used the hybrid symbiosis organisms search (HSOS) algorithm as an optimization technique and used the dynamic modules of PLAXIS-8.6v for the validation of analytical solution. The results are compared with the available literature. At the end of the study, the authors concluded that the results obtained from analytical analysis are well justified with the numerical solutions.

The study “Optimum Design of Braced Steel Space Frames including Soil-Structure Interaction via Teaching-

Learning-Based Optimization and Harmony Search Algorithms” is presented by A. T. Daloglu, M. Artar, K. Ozgan, and A. İ. Karakas. The authors used MATLAB interacting with SAP2000-OAPI codes to carry out the analysis for the 10-storey braced steel space frame example. When the results obtained by using TLBO and HS are compared with each other, the total weight of the structure can be obtained more lighter with the TLBO algorithm. But the authors stated that the TLBO algorithm requires longer time for the analysis.

Another study is presented by the authors A. Kangrang, H. Prasanchum, and R. Hormwichian. Their study applied the conditional genetic algorithm (CGA) and the conditional tabu search algorithm (CTSA) technique to connect with the reservoir simulation model in order to search optimal reservoir rule curves. The results obtained from their study show that the new obtained rule curves from CTSA are more suitable for reservoir operating than the existing rule curves, and it is an effective method for application to find optimal reservoir rule curves.

An experimental study by taking into account the optimization of calcareous fly ash-added cement containing grinding aids and strength-improving additives is made by G. Kaplan, S. A. Yildizel, S. Memiş, and A. U. Öztürk. Optimization process included only the cement with fly ash and chemical additive. The main purposes of this study are the maximum level of 2-day and 28-day compressive strengths and the minimal cost parameter for the cements produced.

The study “Optimal cement mixtures containing mineral admixtures under multiple and conflicting criteria” is

proposed by N. M. García, H. L. Soto-Toro, M. Cabrera-Ríos, and O. M. Suárez. For this multiobjective optimization problem, proper concrete bulk density, percentage of voids, and compressive strength normally are the different objective functions. Consequently, in the decision-making process, they obtained Pareto-optimal results instead of individual solution for the all objective function. They concluded that the decision makers know the best trade-off mixtures for an individual application with the help of this study.

The last study is presented by Z. Lyu, Q. Lu, Y. Song, Q. Xiang, and G. Yang. They made a case study on the design optimization of thin-walled steel-perforated sections by using artificial neural network (ANN). The main contribution of this study is to present an alternative data-driven model using ANNs to overcome some inherent difficulties associated with the design load of perforated steel members for the constructional steel field.

Acknowledgments

We thank all volunteer reviewers in the review process for this special issue. We hope that the accepted papers for special issue will lead to future works related to advanced optimization techniques.

*Tayfun Dede
Moacir Kripka
Vedat Toğan
Victor Yepes
Ravipudi V. Rao*

Research Article

Data-Driven Decision-Making in the Design Optimization of Thin-Walled Steel Perforated Sections: A Case Study

Zhi-Jun Lyu ^{1,2}, Qi Lu ^{1,2}, YiMing Song,^{1,2} Qian Xiang,^{1,2} and Guanghui Yang^{2,3}

¹College of Mechanical Engineering, Donghua University, Shanghai 201620, China

²Shanghai Engineering Research Centre of Storage & Logistics Equipment, Shanghai 201611, China

³Shanghai Jingxing Storage Equipment Engineering Co., Ltd., Shanghai 201611, China

Correspondence should be addressed to Zhi-Jun Lyu; lvzj@dhu.edu.cn

Received 18 October 2017; Revised 7 February 2018; Accepted 5 March 2018; Published 15 May 2018

Academic Editor: Victor Yepes

Copyright © 2018 Zhi-Jun Lyu et al. This is an open access article distributed under the Creative Commons Attribution License, which permits unrestricted use, distribution, and reproduction in any medium, provided the original work is properly cited.

The rack columns have so distinctive characteristics in their design, which have regular perforations to facilitate installation of the rack system that it is more difficult to be analyzed with traditional cold-formed steel structures design theory or standards. The emergence of industrial “big-data” has created better innovative thinking for those working in various fields including science, engineering, and business. The main contribution of this paper lies in that, with engineering data from finite element simulation and physical test, a novel data-driven model (DDM) using artificial neural network technology is proposed for optimization design of thin-walled steel specific perforated members. The data-driven model based on machine learning is able to provide a more effective help for decision-making of innovative design in steel members. The results of the case study indicate that compared with the traditional finite element simulation and physical test, the DDM for the solving the hard problem of complicated steel perforated column design seems to be very promising.

1. Introduction

The advances in the logistic and storage fields have been promoting the wide application of the automated storage and retrieval system (AS/RS) in China. Acting as critical infrastructure for AS/RS, structural design for pallet rack needs elaborate decision-making between structural systems and a variety of steel members in such a way that the stability behaves as intended by the designer and satisfies the constraints imposed by capital investment, environment, and so on. In virtue of the high strength to weight ratio as well as convenience of fabrication and assembly, thin-walled steel is widely used in many fields such as industrial storage racks, civil engineering, bridges, transmission towers, and others [1]. The diversity of wide products, with many dissimilarities of shapes, sizes, and usages, are manufactured by cold forming techniques including folding and rolling and so on. These techniques evidently improve the tensile strength and yield strength but in the meantime also reduce the ductility of thin-walled steel member. Especially the properties of the

corners within thin-walled steel sections are very different from those of the planar steel sheet, bar, or strip after cold forming. Moreover, the thin-walled steel members often buckle locally at some stress level lower in comparison with the yield strength itself when they are under tremendous compression. Up to now, the ultimate load calculations within thin-walled columns design can be obtained by some specific computer programs such as CUFMS [2] and Thin-Wall [3], using the finite strip method (FSM) and GBTUL [4], applying the generalized beam theory (GBT). The direct strength method can be also applied very effectively in other specific programs [5]. However, unlike traditional civil buildings or commercial facilities, the main load-bearing members in storage racks such as columns usually comprise regular arrays of perforations in length direction, which enable beams to be hung by connectors at adjustable heights along with the bracings to constitute the huge three-dimensional framework (Figure 1). The ultimate load capacity of rack column can vary with perforation size, shape, position, and orientation [6, 7]. The stability behavior is one

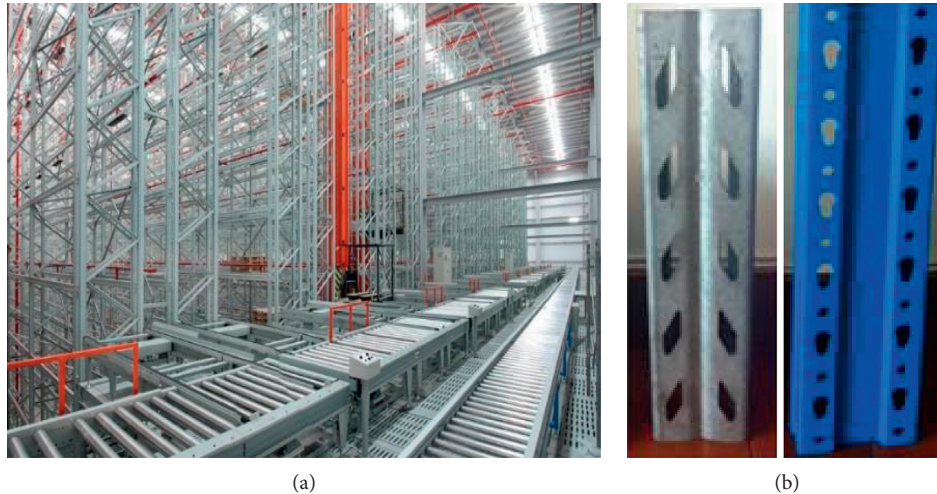


FIGURE 1: (a) Massive automated storage and retrieval system (AS/RS). (b) Arrays of perforations of columns.

of the most prime importance for decision-making of thin-walled steel racks design. Under the influence of continuous perforations, the buckling behavior and load capacity of column may vary so fairly that the various perforations section makes the design procedure of those thin-walled steel columns more complex. Unfortunately, these methods and programs aforementioned cannot be directly used to the perforated steel members because GBT and FSM are essentially 2D theories, but the analysis of these thin-walled perforated sections is a typical 3D problem [8]. The finite element method (FEM) can be naturally used [9], but the computational cost is too expensive to be widely applied in engineering design. In the past years, many investigations [10, 11] were devoted to the study of holes and its arrangement on the ultimate load of rack uprights; however, it has not been achieved in the universally accepted analytical design method for industrial storage racks [12]. For this reason, the current steel member design of pallet rack still mainly depends on physical tests prescribed by specific standards. The increasing demand of cold-formed thin-walled steel in modern industry needs to explore more novel methods of design decision on ultimate load of thin-walled perforated steel member.

Within the design process, the reasoning inherent is to be implemented on different levels with different degrees of uncertainty, abstraction, and impact on product decisions for the elaborate balance between the product quality and manufacturing cost. Actually, the stability analysis for the high-rise steel storage rack structures is becoming even more important, although it has been used for several decades. Furthermore, with advances in various virtual design tools, many engineers and producers have been migrating from physical testing to simulation-based design so that a large number of engineering analytical data have been accumulated so far. The proliferation of industrial “big-data” has been creating many exciting opportunities for those working in various fields such as science, engineering, and business. It has been gradually realized that not only those data from engineering analysis can be used for the product development but also they have the potential to provide

insight and knowledge for the designer to improve the product quality itself. Beyond the specific challenges, technologies and tools have been developed to support decision-making in each phase of product design with relative techniques from the so-called “big data.” In recent years, the machine learning (ML) and data mining (DM) from industrial big data have been rapidly developed as a new discipline in computer science and engineering application [13, 14]. From the perspective of engineering application, the ML and DM focus on analysis and discovery of the potential pattern of the production process and can realize precise prediction of complex engineering problems. Of course, it can also be used to provide a more effective solution for decision-making of enterprises’ innovative design. Among machine learning approaches, artificial neural network (ANN) algorithms have a significant role in predictive modeling because they can be easily utilized to establish the component which learns from existing engineering data in order to make predictions on new engineering data [15].

In constructional steel field, the main contribution of our study is to present an alternative data-driven model using ANNs to overcome some inherent difficulties associated with the design load of perforated steel members and make the optimal design decision of the thin-walled column section with the combination of mechanical performance and fabricating cost factors. In contrast with existing references, the obvious distinctions of our report lie in that the finite element simulation data based on the physical test that are utilized to train BP artificial neural networks in consideration of the perforated effect and uncertainty assessment, and results have been taken comparisons with those of the traditional FEM. The relative model, experiments, and research method are discussed in this paper.

2. Proposed Model Framework

Given conflicting factors (e.g., socioeconomic, safety, environmental, and among others), people often have to make

judgments based on their experience, knowledge, or outcomes of costs-benefits/risk analysis. For a decision maker of the high-rise steel storage rack, achieving the stability goals while meeting the constraints of the production cost is one of the most essential concerns. Up to now, the models available to solve the various design decision problems on steel member can be categorized into two main types: physical-based models and data-driven models. On the one hand, the physical based models are usually considered to be complex, since they require (i) use of knowledge on the physics of interrelationships among various column sectors parameters and the ultimate load, and (ii) adequate data on various tests for model calibration. On the other hand, data-driven models do not consider the physics of the buckling processes but can be effective when large data sets are available on predicting and reasonable number of predictors. The artificial neural networks (ANNs) are one of most widely used data-driven methods based on machine learning. This method has the ability to handle noisy data and thus takes advantage over conventional methods of real-world scenario, where the perforated steel member of compression is typical nonlinear physical relationships underlying various buckling processes that are seemingly not fully understood.

Considering these salient features of ANN, there is a proposed ANN-based data-driven model (DDM) on thin-walled steel perforated member (Figure 2). The model framework is mainly made of four modules, that is, input and output modules, user interface, machine learning approaches, and data acquisition. Being the most critical index on stability design from engineering point of view, the ultimate load ought to be selected as the output of intelligent decision model. The other output is the price of column production that is directly obtained by regular computation. Associated with the mechanical performance of rack column, those important design parameters such as the perforated section, material properties, and fabricating imperfection are chosen as the inputs of DDM. The data acquisition is designed for collecting and transforming the data from the finite element simulations and physical experiments into engineering database. Because the column physical experiments are relatively expensive and real dataset is usually limited in number, and the finite element simulation is employed to expand engineering data as ANN training required in this paper. The user interface is mainly responsible for kind interactive operation with the model, such as feature extraction, model training, parameter optimization, and so on. The machine learning approach is essentially an ANN-based ultimate load prediction toolkit, which can be applied to automatically train the data models and make intelligent design decision in terms of the real thin-walled perforated column inputs. The DDM employs an intelligent decision technique simulating how structure engineer routinely solves problem. When a new AS/RS project is developed, in most cases, the structure engineers firstly need referring to some similar solutions within the existing engineering projects and then obtain a series of similar design parameters of thin-walled steel members including section, material, and others. By means of the ANN-based predictive toolkit, an accurate mechanics

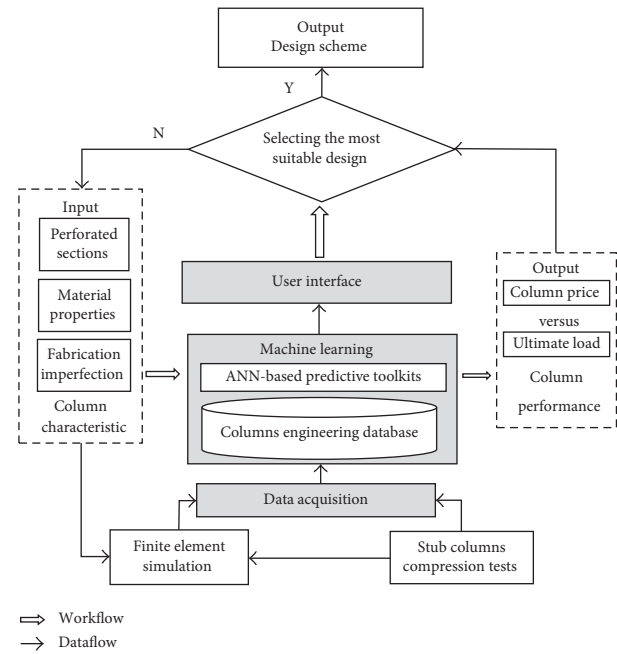


FIGURE 2: Framework of the proposed data-driven design decision based on prediction and optimization of column.

performance of rack column can be predicted very quickly before the new columns are manufactured. These steps usually need continual iterating until some conflicting conditions such as performance and cost can be satisfied at the same time. As a result, the best design decision can be made, and then, the column section parameters optimized. Unlike the existing programs and methods [2–5], the novelties of data-driven model consist the following:

- (i) Encapsulating a great deal of knowledge in a very efficient manner has the capability of updating system knowledge through continuous self-learning.
- (ii) Have robust reasoning mechanism oriented to optimize section parameters according to computer simulation.
- (iii) Take account of factors that are not easily quantifiable (nonnumeric) such as ease of construction, failure mode, and availability, effectively avoiding rule collision as well as trouble from explicit knowledge acquirement.

3. Stub Column Tests

In this paper, the coupon tests of stub column had been performed to synthetically evaluate ultimate load and its strength of these members under consideration of perforations, cold forming processes, various buckling, and its interactions on the basis of EN15512 [16]. The length of specimens is fully satisfied by the code requirements; that is, (1) at the midway between two sets of perforations, it comprises at least five pitches of the perforations. The cap and base plates are welded to each end of the stub upright; (2) the length of specimens is about three times the greatest



FIGURE 3: The experiment setup and supporting system of EN15512 [16].

width of the stub section (without intermediate stiffeners). The end-devices, at both ends, are made of pressure pads of 30 mm thick with around 5 mm indentation and 40 mm diameter ball bearing. The coupon sample is fully grasped at both ends when the tests started. The goal of these experiments was to obtain the precise tensile yield and ultimate load for each thin-walled steel column specimen so that these real engineering data are used to verify the FE model and ANN model. The experiment setup and supporting system are shown in Figure 3. The load was continuously increased until the specimen has buckled and accepted no more load. This load was recorded as the ultimate failure load. The characteristic failure loads (i.e., the ultimate load) were based on a series of tests with the same load position. Nine series of open thin-wall steel sections (Figure 4) chosen as stub columns in pallet racking have been tested and analyzed. The samples parameters of the short column mechanical performance compression test are shown in Table 1 and Figure 5. Dimensions range of upright specimens is relatively wide: flange of 50~145 mm, web of 45~120 mm, and thickness of 1.8~2.5 mm. Nine representative column cross section series selected for the specimen preparation are M45-43, M60-55, M75-58, M90A-65, M90B-78, M100A-90, M100B-100, M100C-130, and M120A-95 which covers the main range of industry manufacturing and application. Among them, five sections have only intermediate stiffener, two sections have edge and intermediate stiffeners, and other sections have none. Total 30 data from different stub columns compression experiments were collected from the Shanghai Jingxing Logistic Equipment Engineering Co., Ltd., China.

Here, the selection of stub columns takes the size of the web, the change of the flange, and reinforcement into consideration to make the DDM much more adaptable. The distribution of tested column sections is illustrated as Figure 6. All experimental data are elaborately divided into two classes

among which 12 data sets are used to verify the finite element model, and the rest are used to make the comparisons with the data-driven model and finite element model.

4. Finite Element Simulation

4.1. Establishment of Geometric Model. The finite element (FE) method has generally accepted to be a very powerful and effective tool for analysis of perforated members and predicting their strength and behavior [9, 10]. In order to develop a high-precision finite element model, however, it is necessary to identify all possible physical actions involved within the structural system under consideration. Referring EN15512 [16], an elaborate finite element model in our study has been built with the professional ANSYS software [17]. Firstly, the 3D models are established based on the actual numerical value of the tested samples using Solidwork software. It is noticed that the cross section and the hole setting are not simplified to ensure the accuracy of the finite element model (Figure 7). After importing the FE model, the element type has been set as SOLID187 which is a high-order solid structural element, including 10 nodes in 3D. The element type SOLID45 is also carefully applied for the load plates modeling. The eight-node three-dimensional solid element with three free degrees per node is often used for linear and nonlinear analysis in the same way.

4.2. Material Properties and Mesh Generation. The materials are setting with nonlinear steel for subsequent buckling analysis by the ANSYS Workbench with Structure Steel NL. Steel yield strength and tensile strength are referred to the Chinese standard GB 50017 2003 [18], where the elastic modulus is 200 GPa, the Poisson ratio is 0.3, and the density is 7850 kg/m³.

Meshing is the basis of finite element analysis. Reasonable meshing can reduce the use of computer memory, and the results were more accurate. Compared to tetrahedral (TET) meshes, hexahedral (HEX) meshes have higher precision and less calculate time. Therefore, HEX dominant has been in the mesh method, the mesh size, smoothness, and other factors are adjusted at the same time. Considering the accuracy of calculation and memory usage, the relevance was adjusted to 50. The imported mesh models are shown in Figure 8.

4.3. Boundary Condition and Loading. Within the column experiments, the test specimen was mounted with the centroid of its gross cross section positioned centrally in the testing machine with one loading platen free to rotate in order to take up any lack of alignment of the end plates of the specimen. In order to simulate the compression test, on a central node of the outer face of two load plates, the displacements shall be properly specified; that is, the line located by these two nodes is the so-called load line (Figure 9). All node displacements of the bottom plate have been set up to zero, and the transversal displacements of the node at the top plate have also been set up to zero. The axial displacement of the load line is gradually increased step by step until the stub

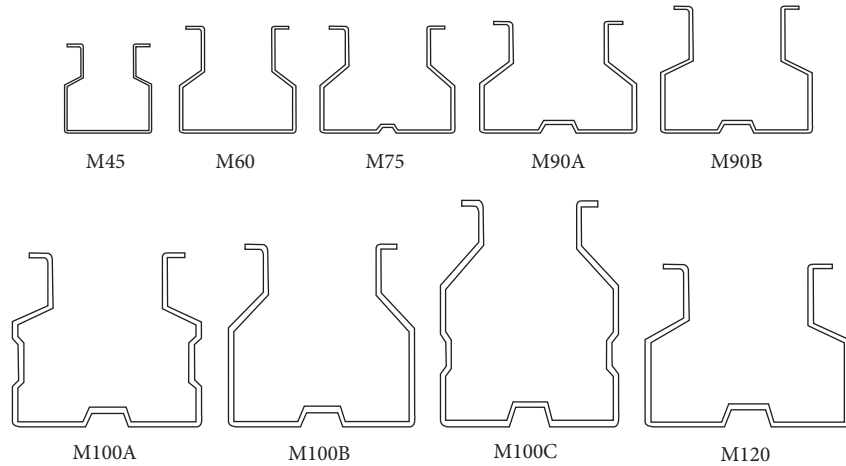


FIGURE 4: Nine series specimen for column tests.

TABLE 1: Dimension of stub test samples (parameters are shown in Figure 5).

Parameter type	a (mm)	b (mm)	c (mm)	L (mm)	d (mm)	e (mm)	f (mm)
M45	45	43	12	300	25	110	125
M60	60	55	12	350	41.8	170	125
M75	75	58	12	400	40.4	170	125
M90A	90	65	12	400	37.1	170	125
M90B	90	78	12	400	33	170	125
M100A	100	90	12	400	25.8	170	125
M100B	100	100	12	400	22.9	170	150
M100C	100	130	12	400	20	170	170
M120A	120	95	12	400	22.5	170	140

can be no longer in force. The controlled displacement method can be applied to simulate the physical test process of ultimate load on the upper plate of the stub column. The displacement is added in continuous increments until it obviously begins to decrease or keep unchanged within a span of time window. At that moment, the maximum load in the stub can be considered the failure force, that is, the ultimate load.

4.4. FE Model Validation. The physical tests for 12 tested stub columns were utilized to calibrate FE simulation models. For example, Figure 10 presents the characteristic failure modes of M90 column compression for experimentally tested and numerically simulated specimens. Obviously, it can be observed that there are good agreements between the modes of the buckling in experiments and analyzed by numerical simulations. It also can be observed in Table 2 that all finite element results were higher than the experimental ones. The reasons for this could be that the geometrical imperfection, residual stress, and nonlinear effects of materials are not fully considered in the finite element model. However, the deviations of FEM simulation have been controlled, not larger than 10% of the real experimental data (Table 2) Therefore, it is concluded that from the point of view of engineering application, the FE

model is able to accurately simulate the experimental tests. The additional 60 data (Table 3) from simulation of different stub columns are obtained by the finite element method based on the physical test, which have been supplementary data for the data-driven model based on ANN.

5. ANN Model Training

In the past years, the application of ANNs has rapidly grown in popularity. The neural networks represent a novel and modern technical conception that can provide solutions in problems for which ordinary algorithms, mathematics, and methodologies are unable to find an acceptable and satisfactory solution [15]. These problems are generally so sophisticated that some of the related mechanisms could not be fully understood by the researchers so far. The internal detailed architecture of ANN for prediction of the ultimate load of thin-walled perforated steel sections is shown in Figure 11.

5.1. Basic Steps of Model Design. The design of the ordinary ANN model may be divided into five steps as follows:

- (i) Step 1: Initialization. Setting the ownership value to random arbitrarily small
- (ii) Step 2: According to the research content, determining input variables and expected output of variables
- (iii) Step 3: Recording the output value which is calculated by passing the function step by step and the final output value
- (iv) Step 4: Adjusting weight. Use recursive methods to adjust weights sequentially from the output node to the intermediate hidden layer.
- (v) Step 5: Returning to the second step and repeating the operation to reduce the error of the output layer.

5.2. The Determination of the Hidden Layers. The determination of the hidden layer in the BP neural network

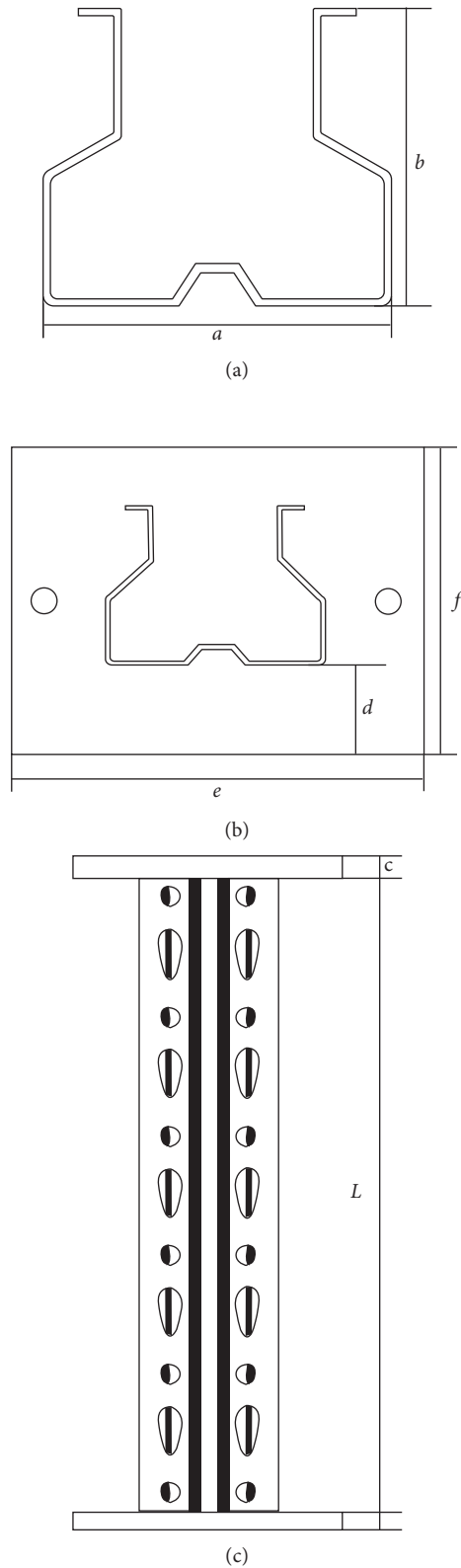


FIGURE 5: Parameters of column test.

model is the key step of modeling which predicts the reliability of steel members. At present, the determination of network parameters (hidden layer number and hidden layer number of neurons) is uncertain. However, in the light of

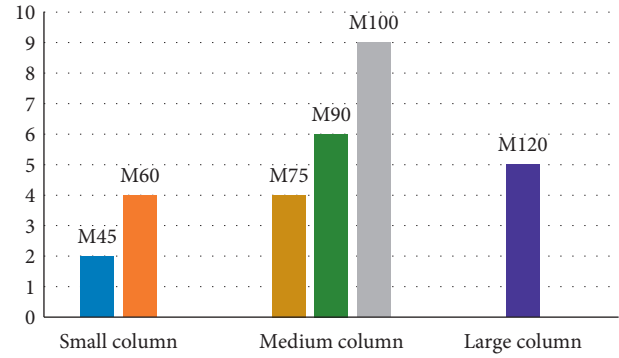


FIGURE 6: The test number of column.

Bishop's report [19], more than one hidden layer is usually not necessary, and the ANN architectures for thin-walled steel design have only one hidden layer. The ANN is trained using a back-propagation algorithm with gradient descent and momentum terms. The number of hidden layers is often related to the number of training samples, the number of neurons in the input layer, and the number of neurons in the output layer in engineering. In literature [15], the node number of hidden layers was obtained as

$$s = \sqrt{0.43mn + 0.12n^2 + 2.54m + 0.77n + 0.35} + 0.51, \quad (1)$$

where m is the number of neurons in the input layer and n is the number of neurons in the output layer.

5.3. The Relational Mapping of Predictive Model Data.

On the basis of current reports [6, 7], there were nine input neurons representation of nine different perforated sections parameters and one output neuron, that is, ultimate load, all listed in Table 4.

The input feature indicators are selected as follows.

5.3.1. Geometric Parameter. The influence of the column length (CL) (L in Figure 5) and the web width (WW) was obvious to the ultimate loading of the column. So the CL and the WW are considered as input variables; based on the parameter sensitivity analysis in literature [19, 20], three parameters which most sensitive (column thickness (CT), opening size (OS), and the flange width (FW)) were put into the forecasting model as input variables.

5.3.2. Structure of Hole. In order to eliminate the effect of the difference on the structure of hole, in this paper, the ratio of the hole area (RHA) was one of the input variables of the prediction model. The equation of RHA is as follows (the formula corresponds to Figure 12):

$$\eta = \frac{S_1 \times n_1 + S_2 \times n_2}{h \times w} \times 100\%, \quad (2)$$

where w is the web width (WW), h is the column length (CL), S_1 is the proportion of the hole shape A, S_2 is the proportion of the hole shape B, n_1 is the number of the hole shape A, and n_2 is the number of the hole shape B.

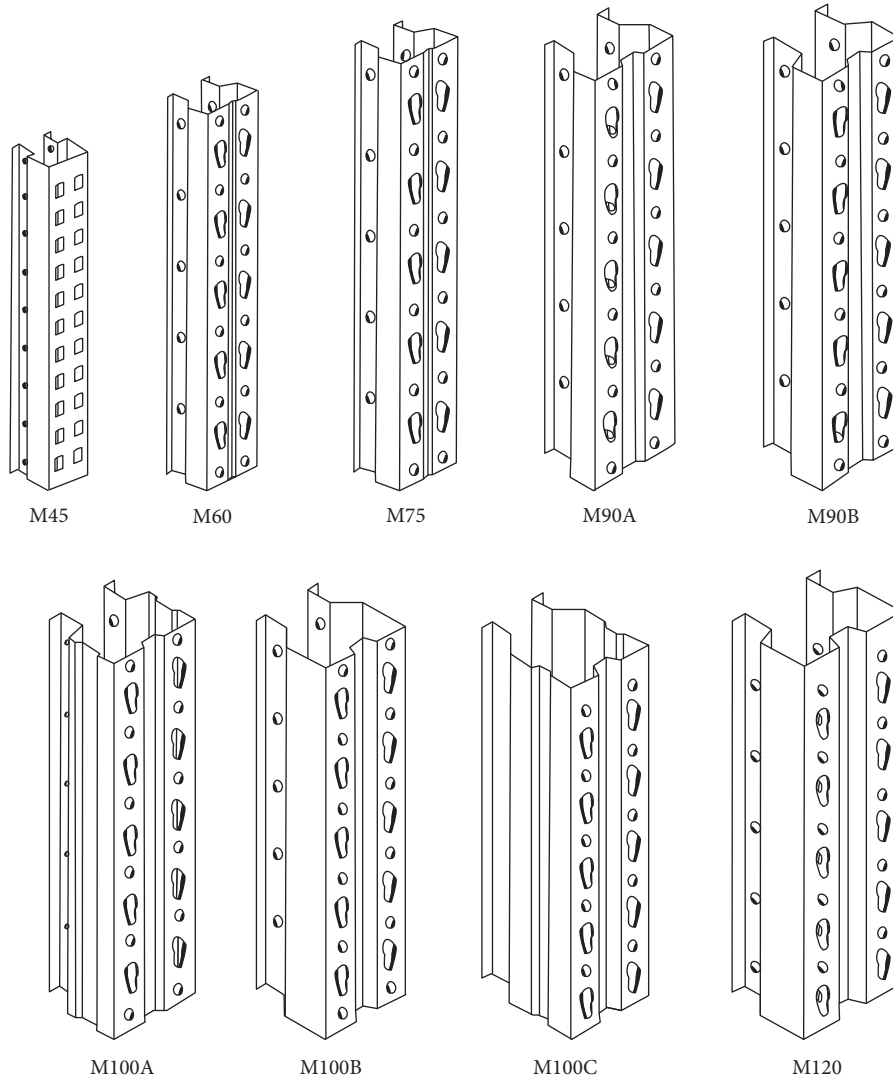


FIGURE 7: 3D models of stub column.

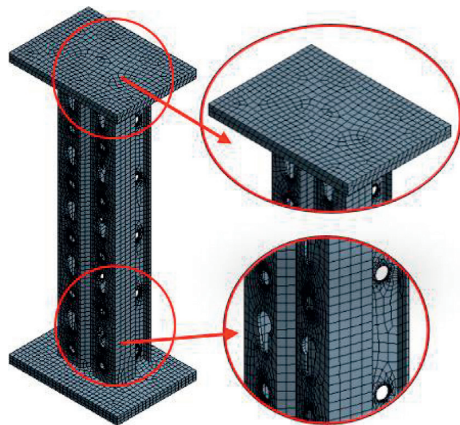


FIGURE 8: Mesh of the FE model on stub column.

5.3.3. *Bending and Right Angles of Section.* GB 50017 2003 [18] is the principle for the design of the storage racking system which considers the number of angles of 90 degrees in the cross section as an essential parameter. The bending

(bending number (BN)) and right angle (right angle number (RAN)) of the column section have influence on prediction results that determined them as the parameters of input variables.

5.3.4. *Reinforcement.* Reinforcement is an effective structural feature to improve the strength of column. The cross section shape of the column series is different, and the reinforcement number (RN) directly affects the ultimate loading of the column (ULC). The dimensional details of the columns are shown in Figure 13.

5.4. *The Training Process of the Model.* Before being fed into ANN, all the data have to be normalized by a preprocessing way where the data are converted in the range $(-1, 1)$. Under feed-forward neural network architecture, each neuron in the hidden layer is responsible for connection of all the neurons in the next and previous layer. Here, the neural network is trained with node number of hidden layers near

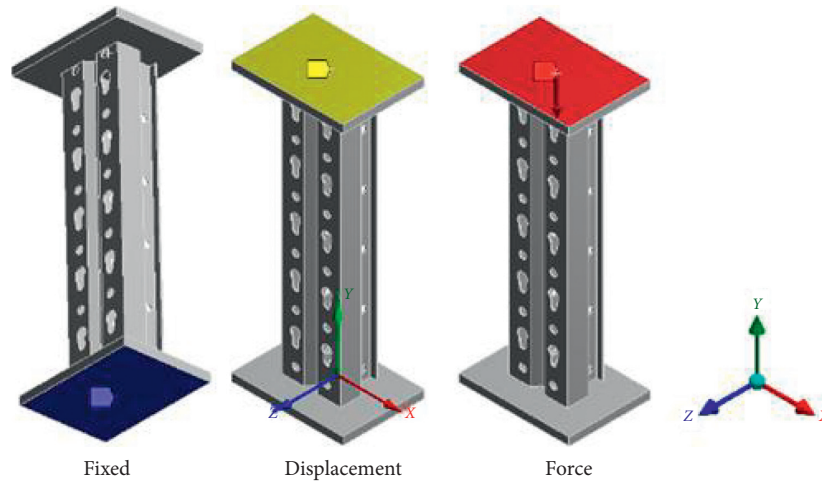


FIGURE 9: Constraint and load setting of the FE model on stub column.

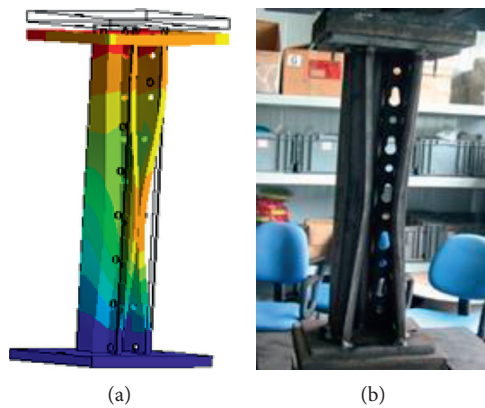


FIGURE 10: The comparison between FEM simulation and physical test (M90 column).

TABLE 2: Comparison among the real measured values and finite element numerical values.

Column type	Measure (N)	FEM (N)	Absolute error (%)
M45-1.5	48735.72	49856.30	2.31
M60-1.8	79771.43	80079.38	0.39
M60-2	107829.81	116348.70	7.90
M75-1.8	120201.30	120906.59	0.58
M75-2	126332.15	133166.10	5.41
M90A-1.8	131635.70	132295.27	0.51
M90B-2	145770.64	156700.50	7.50
M100A-2	184553.71	189905.90	2.91
M100B-2.5	219416.60	220570.64	0.54
M100C-3	341267.70	343081.97	0.53
M120A-2.5	219843.50	238998.70	8.71
M120B-3.5	414820.20	417018.34	0.53
Mean relative error (%)		3.10	
Correlation coefficient, R		0.97	
Proportion of cases with over 5% error		4/12	

In M45-1.5, M45 is the column type, and 1.5 is thickness of the tested stub column.

the one suggested by (1), and finally, nine are found to be most suitable for these specific data sets.

The training function, “trainlm,” has been utilized with the MATLAB ANN toolbox to realize the training of these models. The transformation function of the output layer is “purelin,” and hidden neuron function was “tansig,” which can be obtained from the same ANN toolbox of the MATLAB software [21]. The learning rate η was set from 0.01 to 0.07, which can speed up the convergence of training function on the condition of accepted training precision (Figure 14).

5.5. Uncertainty Assessment. Network training will be automatically terminated if the accepted prediction accuracy of these models such as for the corresponding deviation is not more than 5% between the expected values and the real values. However, with the double purpose of solving the matter of choosing the data to be used in the training and testing phases, a so-called bootstrap resampling method need to be used for uncertainty analysis in statistics and model calibration, by considering an ensemble of ANNs built on different data sets that are sampled with replacement (bootstrapped) from the original one. An obvious merit of this approach is that it provides confidence intervals for a given model output, without making any model assumption (e.g., normality). Here, the entire available data set of N input/output patterns were divided into training, validation, and test data sets equal to 60, 12, and 18 data, respectively. From each bootstrap data set (e.g., resampling times $B = 60$ in this work), a bootstrapped prediction model is trained while the model output of interest can be calculated. Different bootstrap data sets give rise to a distribution of regression functions, and an example of the probability density function (PDF) of the data-driven model output was demonstrated in this paper (Figure 15). So, the model uncertainty of the estimates from the ANNs can be quantified in terms of $(100 \times (1 - 0.05)\%)$ confidence intervals of the obtained model output PDF by the bootstrap algorithm (Figure 16), where

TABLE 3

Column type	Parameter									
	WW (mm)	CT (mm)	FW (mm)	OS (mm)	CL (mm)	RHA (%)	BN	RAN	RN	ULC (N)
M45-1.5	45	1.5	45	25	300	18.205	8	4	0	48458.90
M45-1.5	45	1.5	45	25	300	16.472	8	4	0	49012.59
M45-1.5	45	1.5	45	25	300	15.605	8	4	0	49246.13
M60-1.8	60	1.8	55	34	350	16.525	8	4	0	79349.60
M60-1.8	60	1.8	55	34	350	14.951	8	4	0	80309.17
M60-1.8	60	1.8	55	34	350	14.164	8	4	0	80579.36
M60-2	60	2.0	55	34	350	16.525	8	4	0	107308.45
M60-2	60	2.0	55	34	350	14.951	8	4	0	108429.67
M60-2	60	2.0	55	34	350	14.164	8	4	0	108884.60
M75-1.8	75	1.8	58	45	400	14.222	12	4	1	120201.34
M75-1.8	75	1.8	58	45	400	12.868	12	4	1	121653.31
M75-1.8	75	1.8	58	45	400	12.190	12	4	1	122051.82
M75-2	75	2.0	58	45	400	14.222	12	4	1	125674.21
M75-2	75	2.0	58	45	400	12.868	12	4	1	127122.11
M75-2	75	2.0	58	45	400	12.190	12	4	1	127736.96
M90A-1.8	90	1.8	65	50	400	11.852	12	4	1	131635.78
M90A-1.8	90	1.8	65	50	400	10.723	12	4	1	132952.78
M90A-1.8	90	1.8	65	50	400	10.159	12	4	1	133487.52
M90A-2	90	2.0	65	50	400	11.287	12	4	1	137228.00
M90A-2	90	2.0	65	50	400	11.852	12	4	1	136535.41
M90A-2	90	2.0	65	50	400	10.723	12	4	1	137893.69
M90A-2	90	1.8	78	50	400	11.287	12	4	1	145158.87
M90B-1.8	90	1.8	78	50	400	11.852	12	4	1	144433.37
M90B-1.8	90	1.8	78	50	400	10.723	12	4	1	145882.63
M90B-1.8	90	1.8	78	50	400	10.159	12	4	1	146606.83
M90B-1.8	90	2.0	78	50	400	11.287	12	4	1	145770.64
M90B-2	90	2.0	78	50	400	11.852	12	4	1	145100.68
M90B-2	90	2.0	78	50	400	10.723	12	4	1	146512.32
M90B-2	90	2.0	78	50	400	10.159	12	4	1	147241.47
M100A-2	100	2.0	90	52	400	10.667	20	4	3	183607.50
M100A-2	100	2.0	90	52	400	9.651	20	4	3	185707.72
M100A-2	100	2.0	90	52	400	9.143	20	4	3	186247.73
M100A-2.5	100	2.5	90	52	400	10.667	20	4	3	205633.26
M100A-2.5	100	2.5	90	52	400	9.651	20	4	3	207815.04
M100A-2.5	100	2.5	90	52	400	9.143	20	4	3	208788.40
M100A-2.5	100	2.0	100	52	400	10.159	12	4	1	160872.36
M100B-2	100	2.0	100	52	400	10.667	12	4	1	160047.57
M100B-2	100	2.0	100	52	400	9.651	12	4	1	161711.47
M100B-2	100	2.0	100	52	400	9.143	12	4	1	162635.84
M100B-2	100	2.5	100	52	400	10.159	12	4	1	220570.64
M100B-2.5	100	2.5	100	52	400	10.667	12	4	1	219416.61
M100B-2.5	100	2.5	100	52	400	9.651	12	4	1	221593.87
M100B-2.5	100	2.5	100	52	400	9.143	12	4	1	222748.78
M100C-2	100	2.0	130	52	500	10.159	20	4	3	198040.25
M100C-2	100	2.0	130	52	500	10.667	20	4	3	197057.77
M100C-2	100	2.0	130	52	500	9.651	20	4	3	198989.66
M100C-2	100	2.0	130	52	500	9.143	20	4	3	199955.70
M100C-3	100	3.0	130	52	500	10.667	20	4	3	341267.75
M100C-3	100	3.0	130	52	500	9.651	20	4	3	344931.18
M100C-3	100	3.0	130	52	500	9.143	20	4	3	346865.14
M120A-2.5	120	2.5	95	76	500	8.466	12	4	1	221090.23
M120A-2.5	120	2.5	95	76	500	8.042	12	4	1	222232.38
M120A-2.5	120	2.5	95	76	500	7.619	12	4	1	223289.19
M120A-3	120	3.0	95	76	500	8.466	12	4	1	270660.52
M120A-3	120	3.0	95	76	500	8.889	12	4	1	269336.45
M120A-3	120	3.0	95	76	500	8.042	12	4	1	272240.91
M120A-3	120	3.0	95	76	500	7.619	12	4	1	273437.50
M120B-3.5	120	3.5	150	76	500	8.889	20	4	3	414820.24
M120B-3.5	120	3.5	150	76	500	8.042	20	4	3	419345.72
M120B-3.5	120	3.5	150	76	500	7.619	20	4	3	421089.69

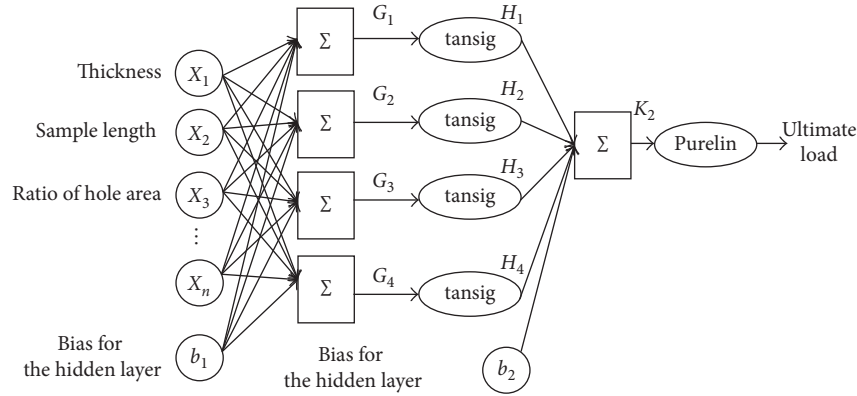


FIGURE 11: ANN architecture.

TABLE 4: Mapping relation of input and output indicators of the prediction model.

Input index	WW	CT	FW	OS	CL	RHA	BN	RAN	RN
Output index									ULC

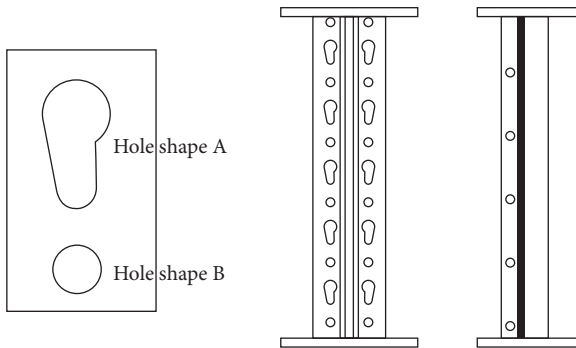


FIGURE 12: Holes' pass and distribution of M90A series column.

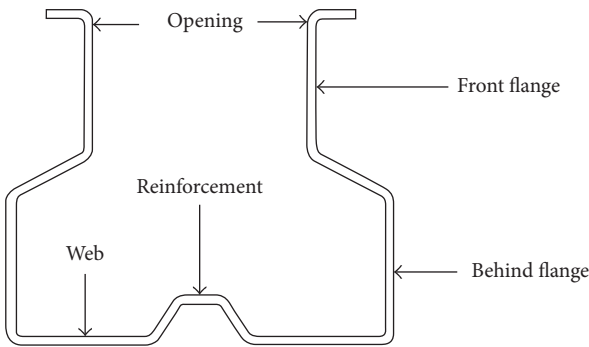


FIGURE 13: Section details of column.

the edges of the box represent the 25th and 75th percentiles and those of the whiskers the 99.3 coverage if the data are normally distributed. The estimates of the best ANN (*dots) and of the bootstrap ensemble of ANNs (red lines) are reported together with the FEM output (plus signs). And these points (represented by a plus sign) are outliers since they are beyond the edges of the box. The presence of

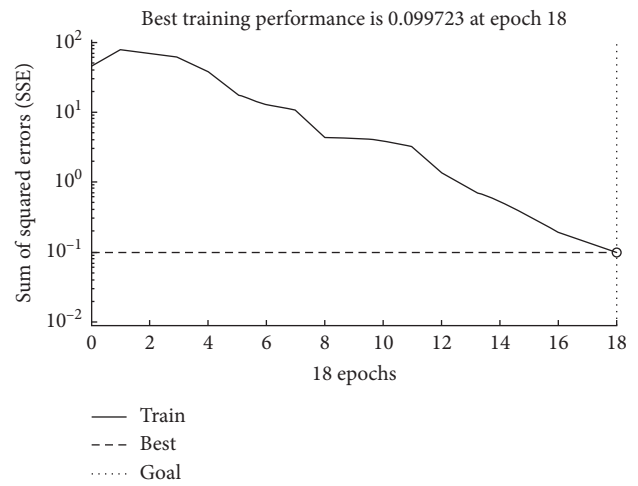


FIGURE 14: The iterative process of predictive model.

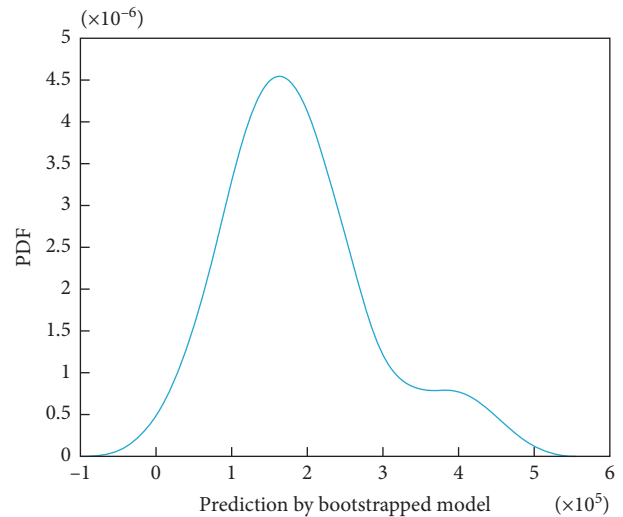


FIGURE 15: PDF curve of the model output.

outliers illustrates that some of the bootstrapped networks could not be well trained because of (i) inefficient calibration of the ANN weights during training (e.g., the back-propagation algorithm maybe falls into a local optimum), or (ii) “unhealthy” configurations of the validation data

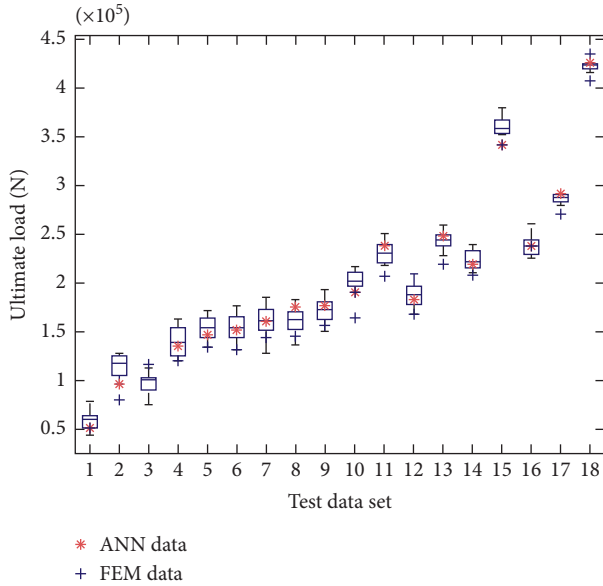


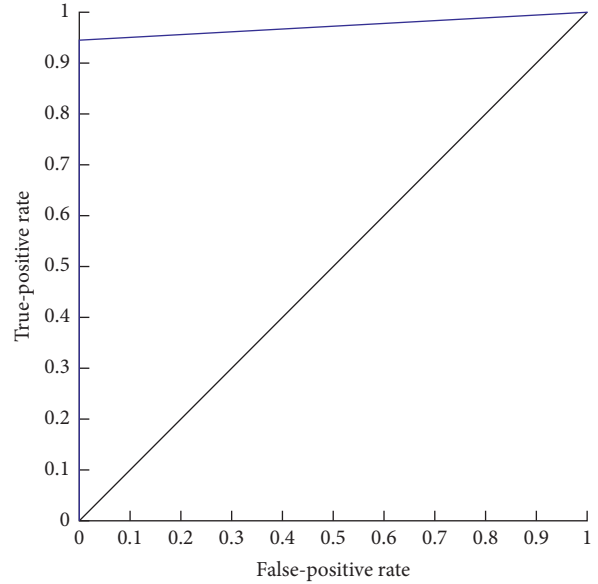
FIGURE 16: Confidence intervals of the ultimate load.

TABLE 5: Comparison among the real measured values, predicted values, and finite element numerical values.

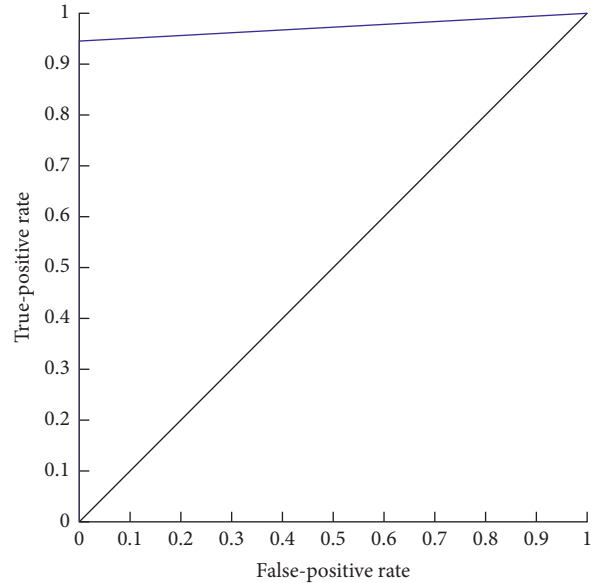
Column type	Measure (N)	Predict (N)	Relative error (%)	FEM (N)	Relative error (%)
M45-1.5	48385.62	48429.20	0.09	49856.37	3.04
M60-1.8	79136.73	83558.23	5.59	80079.43	1.19
M60-2	107142.80	104077.64	2.86	116348.72	8.59
M75-1.8	120057.01	115392.37	3.88	120201.36	0.12
M75-2	125481.44	126375.42	0.71	133166.13	6.12
M90A-1.8	131412.35	131070.89	0.26	131635.72	0.17
M90A-2	136364.28	140316.60	2.89	144199.20	5.75
M90B-1.8	144144.65	135171.32	6.22	145158.93	0.70
M90B-2	144746.99	146277.65	1.06	156700.55	8.26
M100A-2	183358.52	180049.49	1.80	189905.92	3.57
M100A-2.5	205056.90	207739.80	1.31	206744.95	0.82
M100B-2	159740.04	162860.88	1.95	167594.50	4.92
M100B-2.5	219082.27	218138.34	0.43	219416.63	0.15
M100C-2	196641.13	198992.22	1.19	207407.37	5.48
M100C-3	340630.69	342183.74	0.45	341267.72	0.19
M120A-2.5	219349.62	217817.09	0.69	238998.79	8.96
M120A-3	268689.38	271741.82	1.13	270660.52	0.73
M120B-3.5	413894.01	417135.66	0.78	414820.20	0.22
Mean relative error (%)		1.69		3.28	
Correlation coefficient, R		0.99		0.97	
Cases with over 5% error		2		6	

sets owing to random sampling with replacement implied by the bootstrap such as too large number of repeated samples. The bootstrap resampling method-based operative steps to identify the confidence intervals of the distribution of the regression error are detailed in papers [22, 23].

5.6. Result and Discussion. The final results are listed in Table 5, where “Measure,” “Predict,” and “FEM” refer to the



(a)



(b)

FIGURE 17: (a) The ROC curve between real measurement and ANN prediction. (b) The ROC curve between real measurement and FEM simulation.

TABLE 6: Centerline and weight of the sample.

Parameter	Number			
	1	2	3	4
WW (mm)	90	90	90	90
CT (mm)	2.0	2.0	1.8	1.8
FW (mm)	65.0	60.0	72.0	72.5
OS (mm)	50	50	52	45
CL (mm)	400	400	400	400
RHA (%)	11.53	10.92	12.46	12.96
BN	12	20	12	12
RAN	4	4	4	4
RN	1	3	1	1
UCL (N)	136849.52	139997.03	134796.78	133987.94
Fabrication cost	Low	High	Low	Low

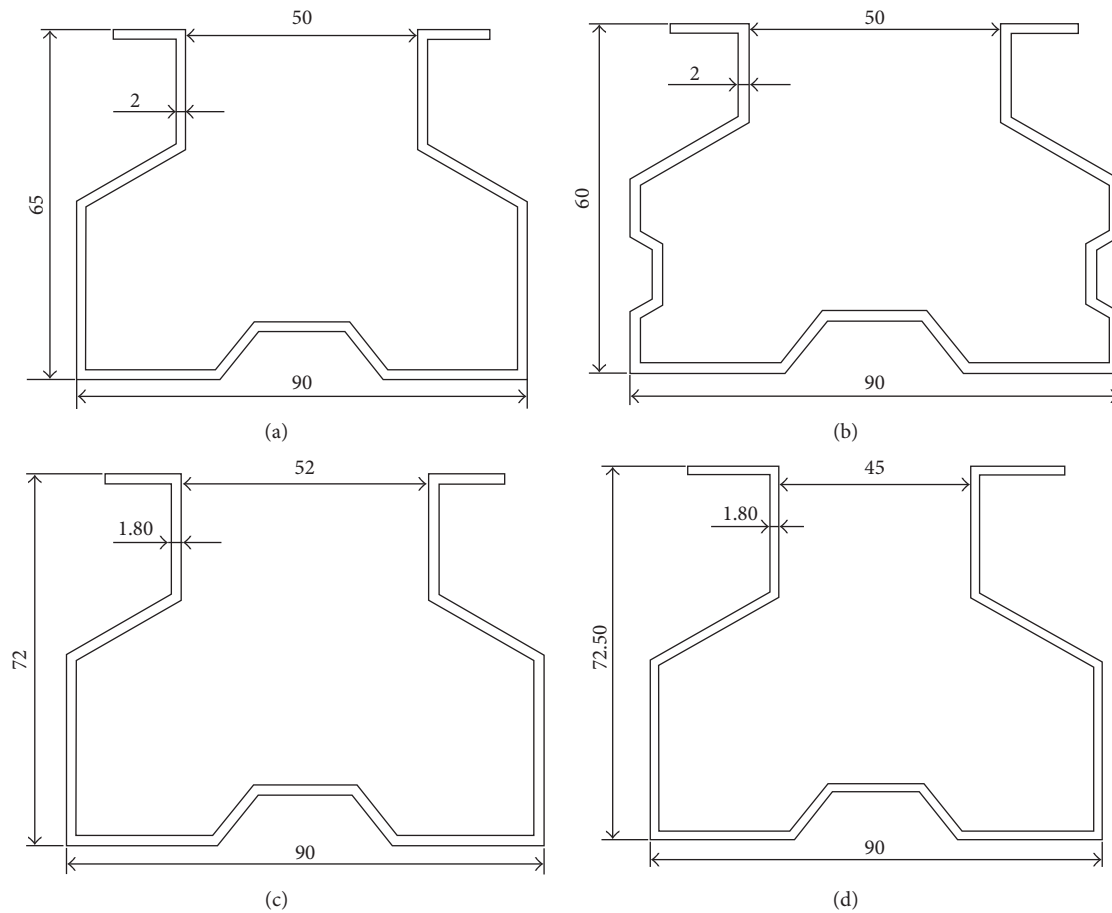


FIGURE 18: Sections of sample (unit: mm).

measured values, the predicted values, and finite element numerical values, respectively. Statistical parameters such as the mean absolute error % and the correlation coefficient R between the expected and real values are used to judge the predictive power of the data-driven models. It is evident that the accuracy of the predictive models is relatively high in all $R > 95\%$, while the ANN model in the mean absolute error and the ratio of the cases with more than 5% error is lower than the FE model. On the contrary, in order to evaluate how good the models and its generalization are made from the ANN model and FEM more clearly, the receiver operating characteristic (ROC) curves are applied to evaluating the proportion of correctly predicted cases as the maximum relative error increases within a prespecified range. A baseline named “normal” was built by the ROC curve (Figure 17) quantized as 1 when the relative error between the observed value is within the range of 5%, and another baseline named “anomaly” is quantized as 1 when the observed value is outside the reference range. The ROC curve evaluating the proportion of correctly predicted cases as the maximum relative error increases within a prespecified range. In this case, it can prove that the ANN prediction is more precise than the FEM simulation for the AUC (area under the ROC curve) of the former is 0.06 than the latter. So, the data-driven models can be more suitable to the

accurate load prediction during the perforated steel member design.

6. Optimization of Design Decision-Making

Considering the social economy, safety, environmental protection, high quality, and other opposing factors, mankind usually makes decisions based on their experience, knowledge, or outcomes of costs-benefits/risk analysis. However, some opposing multiple goals or criteria in decision-making processes may need some optimization because the simple solutions were resisted [24]. Similarly, in the design of racks with thin-walled perforated steel, the engineering projects often involve multiple goals in practice. For example, manufacturers and suppliers are demanding less raw material and more economic efficiency, while consent building authorities require the shelves to have safety coefficients that meet the relevant design code; and end-users hope that the rack will have higher utilization rate for better economic efficiency. These design stakeholders have cross-lights on the appropriate design option within conflicting design decision criteria of safety, economy, and societal considerations [25]. The factors that influence decisions have multiple attributes (e.g., decision goals, diverse criteria, and scope of application), whereby a decision-

TABLE 7: Centerline and weight of the sample.

Number	Thickness (mm)	Centerline length (mm)	Weight (kg)
1	2.0	268.0	1.68
2	2.0	279.0	1.75
3	1.8	289.4	1.64
4	1.8	294.7	1.67

making organ is needed to compare these properties, which assess the applicability of the multifarious decision options. In this paper, a demonstration has been made by the ANN-based data-driven model to perform the optimization of the thin-wall perforated column section. Assuming that the project of the high-rise rack system requires the column which ultimate load is not less than 100000 (N), four design solutions of the thin-walled column perforated section could be empirically taken into consideration in practice, which section parameters are different in detail (Table 6). A column type will be chosen for the highest property-value ratio by the decision-making model.

The consume material of the column may be different considering the shape of different sections (Figure 18). The material calculation equation is as follows:

$$M = t * l * h * g, \quad (3)$$

where M is the material calculation equation, t is the thickness, l is the length of the center line on the cross section, h is the height (400 mm) [16], and g is the material density (7850 kg/m^3) [18].

The results in Table 7 indicate that the difference on the material consumption of four samples between the maximum and the minimum is about 6.28%. The nine parameters of the four different sections are imported into the data-driven model in turn. The results in Table 6 show that all samples meet the requirements, and number 2 has the highest ultimate loading. However, number 1 sample has high property-value ratio could be better solution because it has less reinforcement which leads to less usage of column material and lower fabrication cost in contrast with number 2 column section.

7. Conclusions

As big data techniques are increasingly used in business intelligence and industrial process, there is an urgent need to better understand and really exploit their potentialities on steel structure and civil engineering. To confront the stability challenge of high-rise AR/RS design, this paper presents a novel data-driven decision-making model on the optimization of thin-walled steel perforated sections. Taking thin-walled steel column as an example, the predictions of ultimate load from the data-driven model are made in comparison with those obtained from the FE model and physical test. It is noted that the data-driven model based on the ANN technique is very efficient, while prediction performance is much closer to the physical test than those obtained from the FE models. Of course, the advantages of FEM are determined by the thin-walled section buckling and their mechanization. However, the optimal design solutions

often need very complex decision-making process that cannot be treated adequately by only using conventional CAE tools, unless the designer possesses with full special skills, knowledge, and experience. Here, we only demonstrate that, trained with the engineering data sets from experiment and simulation, the data-driven model is able to predict the design load of different columns through self-learning, which can help the designer to make the better decision for steel member design on pallet rack. Although the results in our paper seem to be preliminary, it has been observed that the data-driven model for solving the hard problem of complicated perforated members design is very promising. With advancement in data mining and deep learning techniques, much of research activities within the civil engineering field are oriented towards making analysis-based design improvement processes more intelligent and less experience dependent, and the producer's subject intuition in industry and society will finally be replaced by smart and friendly expert systems in the future.

Conflicts of Interest

The authors declare that there are no conflicts of interest.

Authors' Contributions

Qi Lu and YiMing Song contributed the FE and predict models. Qian Xiang performed the predict system. Guanghui Yang realized the engineering application. Zhi-Jun Lyu wrote the paper.

Acknowledgments

This paper has been funded by technology innovation program of Shanghai Municipal Science and Technology Commission (15DZ0500400 and 17DZ2283800) and Shanghai Municipal Natural Science Foundation (15ZR1400600).

References

- [1] S. N. R. Shah, N. H. Ramli Sulong, M. Z. Jumaat, and M. Shariati, "State-of-the-art review on the design and performance of steel pallet rack connections," *Engineering Failure Analysis*, vol. 66, pp. 240–258, 2016.
- [2] B. W. Schafer and S. Adany, "Buckling analysis of cold-formed steel members using CUFPM: conventional and constrained finite strip methods," in *Proceedings of the Eighteenth International Specialty Conference on Cold-Formed Steel Structures*, Orlando, FL, USA, October 2006.
- [3] J. P. Papangelis and G. J. Hancock, "Computer analysis of thin-walled structural members," *Computers and Structures*, vol. 56, no. 1, pp. 157–176, 1995.
- [4] R. Bebbiano, P. Pina, N. Silvestre, and D. Camotim, *GBTUL—Buckling And Vibration Analysis of Thin-Walled Members*, DECivil/IST, Technical University of Lisbon, Lisbon, Portugal, 2008, <http://www.civil.ist.utl.pt/gbt>.
- [5] B. W. Schafer, "Review: the direct strength method of cold-formed steel member design," *Journal of Constructional Steel Research*, vol. 64, no. 7-8, pp. 766–778, 2008.
- [6] M. Shariati, M. M. Tahir, T. C. Wee et al., "Experimental investigations on monotonic and cyclic behavior of steel pallet

- rack connections,” *Engineering Failure Analysis*, vol. 85, pp. 149–166, 2017.
- [7] M. P. Kulatunga and M. Macdonald, “Investigation of cold-formed steel structural members with perforations of different arrangements subjected to compression loading,” *Thin-Walled Structures*, vol. 67, pp. 78–87, 2013.
- [8] M. Casafont, M. M. Pastor, F. Roure, and T. Pekoz, “An experimental investigation of distortional buckling of steel storage rack columns,” *Thin-Walled Structures*, vol. 49, no. 8, pp. 933–946, 2011.
- [9] A. Crisan, V. Ungureanu, and D. Dubin, “Behavior of cold-formed steel perforated sections in compression: part 2-numerical investigations and design considerations,” *Thin-Walled Structures*, vol. 61, pp. 97–105, 2012.
- [10] P. Zhang and M. Shahria Alam, “Experimental investigation and numerical simulation of pallet-rack stub columns under compression load,” *Journal of Constructional Steel Research*, vol. 133, pp. 282–299, 2017.
- [11] C. Bernuzzi and F. Maxenti, “European alternatives to design perforated thin-walled cold-formed beam-columns for steel storage systems,” *Journal of Constructional Steel Research*, vol. 110, pp. 121–136, 2015.
- [12] I. Yaqoob, I. A. T. Hashem, A. Gani et al., “Big data: from beginning to future,” *International Journal of Information Management*, vol. 36, no. 6, pp. 1231–1247, 2016.
- [13] L. Zhoua, S. Pana, J. Wanga, and A. V. Vasilakos, “Machine learning on big data: Opportunities and challenges,” *Neurocomputing*, vol. 237, pp. 350–361, 2017.
- [14] A. Prieto, B. Prieto, E. M. Ortigosa et al., “Neural networks: an overview of early research, current frameworks and new challenges,” *Neurocomputing*, vol. 214, pp. 242–268, 2016.
- [15] A. A. Chojaczyka, A. P. Teixeira, L. C. Neves, J. B. Cardoso, and C. Guedes Soares, “Review and application of artificial neural networks models in reliability analysis of steel structures,” *Structural Safety*, vol. 52, pp. 78–89, 2015.
- [16] European Standard EN 15512, *Steel Static Storage Systems—Adjustable Pallet Racking Systems—Principles for Structural Design*, European Committee for Standardization, Brussels, Belgium, 2009.
- [17] ANSYS Inc., *ANSYS Mechanical APDL Structural Analysis Guide: ANSYS Release 13.0*, ANSYS Inc., Canonsburg, PA, USA, 2010.
- [18] *Code for Design of Steel Structures GB 50017-2003*, 2003, in Chinese.
- [19] C. Bishop, *Neural Networks for Pattern Recognition*, Oxford University Press, New York, NY, USA, 1995.
- [20] O. Akaa, A. Abu, M. Spearpoint, and S. Giovinazzi, “Optimising design decision-making for steel structures in fire using a hybrid analysis technique,” *Fire Safety Journal*, vol. 91, pp. 532–541, 2017.
- [21] MathWorks, *MATLAB (R017a) UserGuide 2017.3*, MathWorks, Inc., Natick, MA, USA, 2017, <http://www.mathworks.com/support>.
- [22] E. Ferrario, N. Pedroni, E. Zio, and F. Lopez-Caballero, “Bootstrapped artificial neural networks for the seismic analysis of structural systems,” *Structural Safety*, vol. 67, pp. 70–84, 2017.
- [23] M. R. A. van Gent, H. F. P. van den Boogaard, B. Pozueta, and J. R. Medina, “Neural network modelling of wave overtopping at coastal structures,” *Coastal Engineering*, vol. 54, no. 8, pp. 586–593, 2007.
- [24] T. L. Saaty, “How to make a decision: the analytic hierarchy process,” *Interfaces*, vol. 24, no. 6, pp. 19–43, 1994.
- [25] S. R. Acharya and K. S. Sivakumaran, “Finite element models for thin-walled steel member connections,” *ISRN Civil Engineering*, vol. 2012, Article ID 197170, 7 pages, 2012.

Research Article

Pseudodynamic Bearing Capacity Analysis of Shallow Strip Footing Using the Advanced Optimization Technique “Hybrid Symbiosis Organisms Search Algorithm” with Numerical Validation

Arijit Saha ¹, Apu Kumar Saha,² and Sima Ghosh¹

¹Department of Civil Engineering, National Institute of Technology Agartala, Barjala, Jirania, 799046 West Tripura, India

²Department of Mathematics, National Institute of Technology Agartala, Barjala, Jirania, 799046 West Tripura, India

Correspondence should be addressed to Arijit Saha; sahaarijit20@gmail.com

Received 26 July 2017; Revised 25 September 2017; Accepted 9 October 2017; Published 5 April 2018

Academic Editor: Moacir Kripka

Copyright © 2018 Arijit Saha et al. This is an open access article distributed under the Creative Commons Attribution License, which permits unrestricted use, distribution, and reproduction in any medium, provided the original work is properly cited.

The analysis of shallow foundations subjected to seismic loading has been an important area of research for civil engineers. This paper presents an upper-bound solution for bearing capacity of shallow strip footing considering composite failure mechanisms by the pseudodynamic approach. A recently developed hybrid symbiosis organisms search (HSOS) algorithm has been used to solve this problem. In the HSOS method, the exploration capability of SQI and the exploitation potential of SOS have been combined to increase the robustness of the algorithm. This combination can improve the searching capability of the algorithm for attaining the global optimum. Numerical analysis is also done using dynamic modules of PLAXIS-8.6v for the validation of this analytical solution. The results obtained from the present analysis using HSOS are thoroughly compared with the existing available literature and also with the other optimization techniques. The significance of the present methodology to analyze the bearing capacity is discussed, and the acceptability of HSOS technique is justified to solve such type of engineering problems.

1. Introduction

The subject of bearing capacity is one of the important aspects of geotechnical engineering problems. Loads from buildings are transmitted to the foundation by columns or by load-bearing walls of the structures. Many researchers like Prandtl [1], Terzaghi [2], Meyerhof [3, 4], Vesic [5, 6], and many more have investigated the mechanisms of bearing capacity of foundation under a static loading condition. Due to seismic loading, foundations may experience a reduction in bearing capacity and an increase in settlement. Two sources of loading must be taken into consideration, initial loading due to lateral forces imposed on superstructure and kinematic loading due to ground movements developed during the earthquake. The pioneering works in determining the seismic bearing capacity of shallow strip footings were done by Budhu and Al-Karni [7],

Dormieux and Pecker [8], Soubra [9–11], Richards et al. [12], Choudhury and Subha Rao [13], Kumar and Ghosh [14], and many others using pseudostatic approach with the help of different solution techniques such as method of slices, limit equilibrium, method of stress characteristics, and upper bound limit analysis. Apart from these analytical researchers, Shafiee and Jahanandish [15] and Chakraborty and Kumar [16] used finite element method to estimate the seismic bearing capacity of strip footings on the soil using PLAXIS-2D considering the pseudostatic approach. Since, in the pseudostatic method, the dynamic loading induced by the earthquake is considered as time-independent, which ultimately assumes that the magnitude and phase of acceleration are uniform through the soil layer, pseudodynamic analysis is developed where the effects of both shear and primary waves are considered along with the period of lateral shaking. Ghosh [17] and Saha and Ghosh [18]

evaluated pseudodynamic bearing capacity using limit analysis method and limit equilibrium method, respectively, considering the linear failure surface. In the earlier analyses, the resistance of unit weight, surcharge, and cohesion is considered separately. Therefore, if the solution was done for shallow strip footing resting on c - Φ soil, there will be three separate coefficients: one for unit weight, another for surcharge, and the other for cohesion. But in a practical situation, there will be a single failure mechanism for the simultaneous resistance of unit weight, surcharge, and cohesion. Thus, an attempt is made to present a single seismic bearing capacity coefficient for the simultaneous resistance of unit weight, surcharge, and cohesion. Here, in this paper, the pseudodynamic bearing capacity of shallow strip footing considering composite failure mechanism resting on c - Φ soil is solved using the upper-bound limit analysis method. A relative ease in solving geometrically complex multidimensional problem renders limit analysis, attractive as an alternative to numerical codes. The kinematic method of limit analysis hinges on constructing a velocity field that is admissible for a rigid-perfect plastic material obeying the associative flow rule.

Nowadays, nature-based global optimization algorithms such as genetic algorithms (GA), particle swarm optimization (PSO) algorithm, and many other algorithms have been successfully applied to solve different science and engineering complex optimization problems, especially civil engineering problems such as slope stability [19, 20, 21–28], retaining walls [29–31], and structural design [32]. Cheng and Prayogo [33] introduced a new nature-based optimization technique, called symbiotic organisms search (SOS) algorithm. This technique is based on the interactive relationship among the organism in the ecosystem. It has no algorithm-specific control parameters. The SOS algorithm has been successfully applied to solve different engineering optimization problems [34–38]. Recently, Nama et al. [39] proposed a hybrid algorithm called hybrid symbiotic organisms search (HSOS) algorithm, which is the combination of SOS algorithm and simple quadratic interpolation method [40]. Here, in this paper, HSOS algorithm is used to optimise the pseudodynamic bearing capacity of shallow strip footing considering upper bound limit analysis method. Mathematically, the problem can be represented as a nonlinear hard optimization problem, which can be solved by the HSOS algorithm which is found to be a more satisfactory optimum solution and can be used for designing the shallow strip footing. In the HSOS algorithm, failure surface angle (α , β) and t/T are considered as the search variables. So, it can be applied to obtain optimal solutions in the different fields of science and engineering. Numerical analysis is also done using dynamic module of PLAXIS-8.6v software to validate this analytical solution. Results are presented in tabular form including comparison with other available analyses. Effects of a wide range of variation of parameters like soil friction angle (Φ), cohesion factor ($2c/\gamma B_0$), depth factor (D_f/B_0), and horizontal and vertical seismic accelerations (k_h , k_v) on the normalized reduction factor (N_{ye}/N_{ys}) have been studied.

Therefore, the main contributions of this paper are summarized as follows:

- (i) Evaluation of pseudodynamic bearing capacity coefficient of shallow strip footing resting on c - Φ soil considering composite failure surface using upper bound limit analysis method.
- (ii) A single pseudodynamic bearing capacity coefficient is presented here considering the simultaneous resistance of unit weight, surcharge, and cohesion.
- (iii) A recent hybrid optimization algorithm (called HSOS) is used to solve the pseudodynamic bearing capacity minimization optimization problem.
- (iv) PLAXIS-8.6v software is used to solve this above-mentioned problem numerically for the validation of the analytical formulation.
- (v) The obtained results are compared with the other results which are available in literature and the results obtained by other state-of-the-art algorithms.

The remaining part of the paper is organized as follows: Section 2 discusses the formulation of the real-world geotechnical earthquake engineering optimization problem such as the pseudodynamic bearing capacity of a shallow foundation. The overview of the optimization algorithm HSOS is presented in Section 3. Section 4 presents discussions of the results obtained by the HSOS algorithm to show the efficiency and accuracy of this hybrid algorithm for solving this engineering optimization problem. Numerical analysis of shallow strip footing using the dynamic module of PLAXIS-8.6v software and the validation of analytical formulation are discussed in Section 5, and finally, Section 6 presents the conclusion and the summary of the outcome of the paper.

2. Formulation of Pseudodynamic Bearing Capacity Coefficient

2.1. Consideration of Model. Let us consider a shallow strip footing of width (B_0) resting below the ground surface at a depth of D_f over which a load (P) of column acts. The homogeneous soil of effective unit weight γ has Mohr–Coulomb characteristic c - Φ and can be considered as a rigid plastic body. For shallow foundation ($D_f \leq B_0$), the overburden pressure is idealized as a surcharge ($q = \gamma D_f$) which acts over the length of BC. The classical two-dimensional slip line field obtained by Prandtl [1] is the traditional failure mechanism which has three regions such as active zone, passive zone, and logarithmic radial-fan transition zone. In this composite failure mechanism, half of the failure is assumed to occur along the surface AEDC, which is composed of a triangular elastic zone ABE, triangular passive Rankine zone BDC, and in between them a log spiral radial shear zone BDE shown in Figure 1(a) [41]. It is a composite mechanism that is defined by the angular parameters α and β in which the log-spiral slip surface ED is a tangent to lines AE and DC at E and D, respectively. Figures 2 and 3 show the detailed free

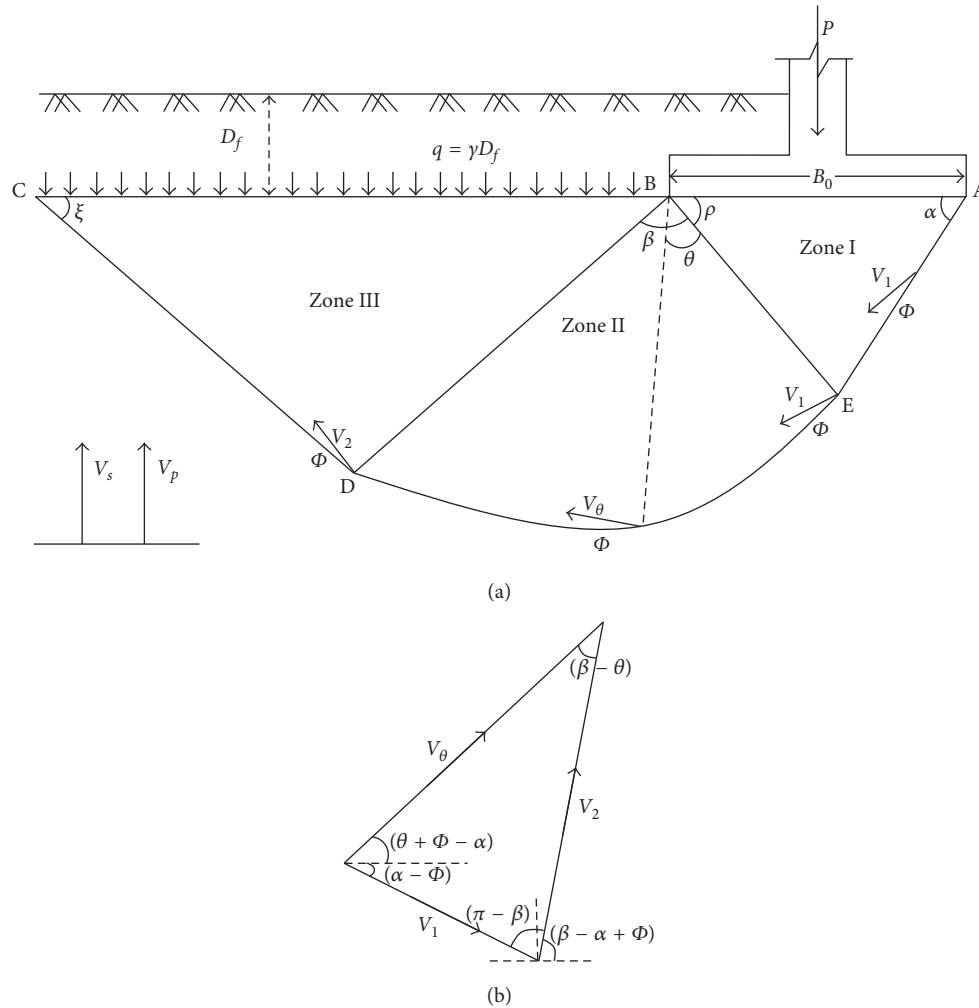


FIGURE 1: Composite failure mechanism [41]. (a) Collapse mechanism. (b) Velocity hodograph.

body diagram of the elastic zone ABE and composite passive Rankine zone and the log-spiral shear zone BEDC, respectively.

2.2. Collapse Mechanism. At collapse, it is assumed that the footing and the underlying zone ABE moves in phase with each other at the same absolute velocity V_1 making an angle Φ with the discontinuity line AE in order to represent the normality condition for an associated flow rule Coulomb material. Hence, there is no dissipation of energy along the soil-structure interface. Whereas the radial log-spiral shearing zone BED is bounded by a log-spiral curve ED. The equation for the curve in polar coordinates (r, θ) is $r = r_0 e^{\theta \tan \phi}$. The centre of this log-spiral ED is at point B, and the radius r_0 is the length of the line BE, where $r_0 = B_0 \sin \alpha / \cos \phi$ and the width of the footing $AB = B_0$. Note that, in this mechanism, we have assumed that the line AE is a tangent to the log-spiral curve at point E; hence, there is no velocity discontinuity along BE. The radial shear zone BED may be considered to be composed of a sequence of rigid triangles, as in the investigations by Chen, using the symmetrical Hill and Prandtl's

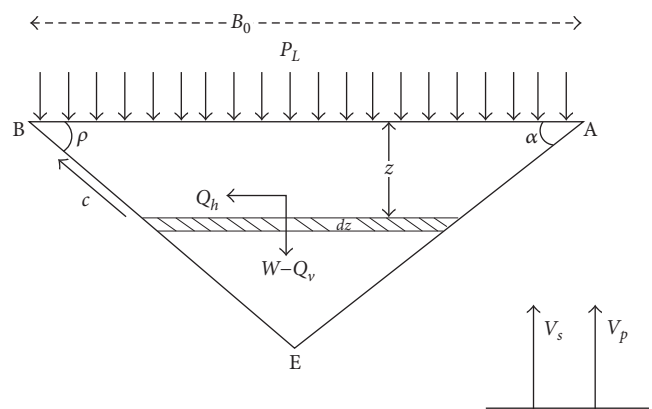


FIGURE 2: Elastic wedge.

mechanisms. All the small triangles move as rigid bodies in directions which make an angle Φ with the discontinuity line ED. The velocity of each small triangle is determined by the condition that the relative velocity between the triangles in contact has the direction which makes an angle Φ to the contact surface. It has been shown

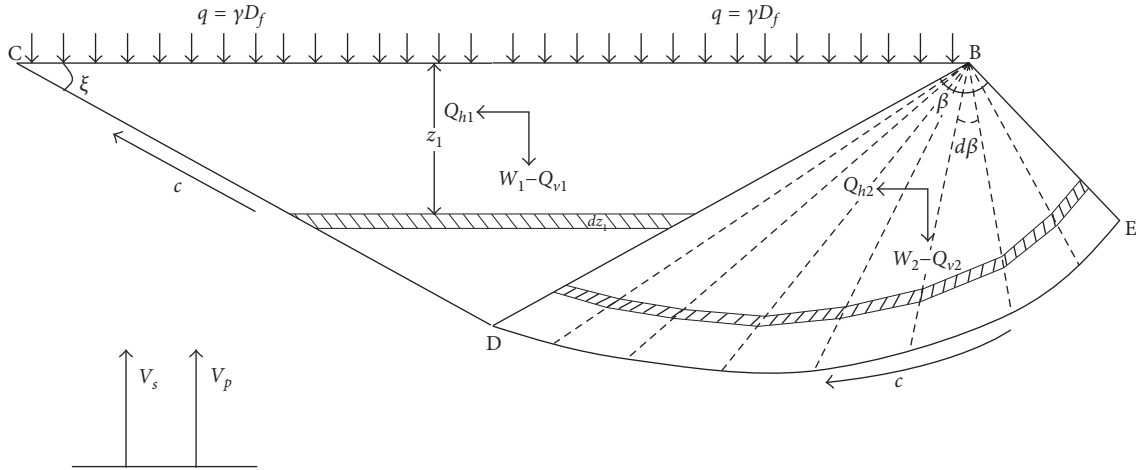


FIGURE 3: Log-spiral zone.

that the velocity V of each triangle is $V_1 = V_0 e^{\theta \tan \phi}$. The log-spiral curve ED is assumed to be tangent to the line DE at D; hence, there is no velocity discontinuity along the line BD. Finally, the triangular wedge BCD is assumed to be rigid, moving with velocity, $V_2 = V(\beta) = V_1 e^{\beta \tan \phi}$. Therefore, the velocities so determined constitute a kinematically admissible velocity field. Velocity hodograph of this composite failure mechanism is shown in Figure 1(b). Having established the velocity field of the kinematically admissible failure mechanism, the incremental external work done and the incremental internal energy dissipation are calculated following the procedure as mentioned in [42].

2.3. Analysis of Bearing Capacity

2.3.1. Elastic Wedge. Weight of the wedge ABE,

$$W = \frac{\gamma B_0^2 \sin \alpha \sin \rho}{2 \cos \phi}, \quad (1)$$

where $\rho = (\pi/2) - (\alpha - \phi)$.

If the base of the wedge is subjected to harmonic horizontal and vertical seismic accelerations of amplitude $a_h g$ and $a_v g$, respectively, the acceleration at any depth z and time t , below the top of the surface, can be expressed as

$$a_h(z, t) = a_h \sin \omega \left(t - \frac{r_0 \sin \rho - z}{V_s} \right), \quad (2)$$

$$a_v(z, t) = a_v \sin \omega \left(t - \frac{r_0 \sin \rho - z}{V_p} \right). \quad (3)$$

The mass of a thin element of the elastic wedge at depth z is

$$m(z) = \frac{\gamma}{g} \left(\frac{1}{\tan \alpha} + \frac{1}{\tan \rho} \right) (r_0 \sin \rho - z) dz. \quad (4)$$

The total horizontal and vertical inertia forces acting within the elastic zone can be expressed as follows:

$$\begin{aligned} Q_h &= \gamma k_h \left(\frac{1}{\tan \alpha} + \frac{1}{\tan \rho} \right) \int_0^{r_0 \sin \rho} (r_0 \sin \rho - z) \sin \omega \left(t - \frac{r_0 \sin \rho - z}{V_s} \right) dz \\ &= \frac{\gamma B_0^2 \lambda k_h \sin^2 \rho \sin^2 \alpha}{2 \pi r_0 \sin \rho \cos^2 \phi} \left(\frac{1}{\tan \alpha} + \frac{1}{\tan \rho} \right) \left[\cos 2\pi \left(\frac{t}{T} - \frac{r_0 \sin \rho}{\lambda} \right) + \frac{r_0 \sin \rho}{2\pi \lambda} \left\{ \sin 2\pi \left(\frac{t}{T} - \frac{r_0 \sin \rho}{\lambda} \right) - \sin 2\pi \frac{t}{T} \right\} \right] = \frac{\gamma}{2} B_0^2 q_h, \end{aligned} \quad (5)$$

$$\begin{aligned} Q_v &= \gamma k_v \left(\frac{1}{\tan \alpha} + \frac{1}{\tan \rho} \right) \int_0^{r_0 \sin \rho} (r_0 \sin \rho - z) \sin \omega \left(t - \frac{r_0 \sin \rho - z}{V_p} \right) dz \\ &= \frac{\gamma B_0^2 \eta k_v \sin^2 \rho \sin^2 \alpha}{2 \pi r_0 \sin \rho \cos^2 \phi} \left(\frac{1}{\tan \alpha} + \frac{1}{\tan \rho} \right) \left[\cos 2\pi \left(\frac{t}{T} - \frac{r_0 \sin \rho}{\eta} \right) + \frac{r_0 \sin \rho}{2\pi \eta} \left\{ \sin 2\pi \left(\frac{t}{T} - \frac{r_0 \sin \rho}{\eta} \right) - \sin 2\pi \frac{t}{T} \right\} \right] = \frac{\gamma}{2} B_0^2 q_v. \end{aligned} \quad (6)$$

2.3.2. *Passive Rankine Zone.* Weight of the wedge BCD,

$$W_1 = \frac{\gamma}{2} \frac{B_0^2 e^{2\beta \tan \phi} \sin^2 \alpha \cos(\beta - \alpha + \phi)}{\cos \phi \sin \xi}. \quad (7)$$

The mass of a thin element of the elastic wedge at depth z_1 is

$$m(z_1) = \frac{\gamma}{g} \left[\left\{ \tan(\beta + \phi - \alpha) + \frac{1}{\tan(\beta - \alpha)} \right\} \times \left\{ r_0 e^{\beta \tan \phi} \cos(\beta + \phi - \alpha) - z \right\} \right] dz. \quad (8)$$

The acceleration at any depth z_1 and time t , below the top of the surface, can be expressed as

$$a_h(z_1, t) = a_h \sin \omega \left(t - \frac{r_0 e^{\beta \tan \phi} \cos(\beta + \phi - \alpha) - z_1}{V_s} \right), \quad (9)$$

$$a_v(z_1, t) = a_v \sin \omega \left(t - \frac{r_0 e^{\beta \tan \phi} \cos(\beta + \phi - \alpha) - z_1}{V_p} \right). \quad (10)$$

The total horizontal and vertical inertia force acting within the passive Rankine zone can be expressed as follows:

$$\begin{aligned} Q_{h1} &= \gamma k_h \left\{ \tan(\beta + \phi - \alpha) + \frac{1}{\tan(\beta - \alpha)} \right\} \int_0^{r_0 e^{\beta \tan \phi} \cos(\beta + \phi - \alpha)} \left[\left\{ r_0 e^{\beta \tan \phi} \cos(\beta + \phi - \alpha) - z \right\} \sin \omega \left(t - \frac{r_0 e^{\beta \tan \phi} \cos(\beta + \phi - \alpha) - z_1}{V_s} \right) \right] dz_1 \\ &= \frac{\gamma B_0^2 \lambda k_h e^{2\beta \tan \phi} \cos^2(\beta + \phi - \alpha) \sin^2 \alpha}{2\pi r_0 e^{\beta \tan \phi} \cos(\beta + \phi - \alpha) \cos^2 \phi} \left\{ \tan(\beta + \phi - \alpha) + \frac{1}{\tan(\beta - \alpha)} \right\} \left[\cos 2\pi \left(\frac{t}{T} - \frac{r_0 e^{\beta \tan \phi} \cos(\beta + \phi - \alpha)}{\lambda} \right) \right. \\ &\quad \left. + \frac{r_0 e^{\beta \tan \phi} \cos(\beta + \phi - \alpha)}{2\pi \lambda} \left\{ \sin 2\pi \left(\frac{t}{T} - \frac{r_0 e^{\beta \tan \phi} \cos(\beta + \phi - \alpha)}{\lambda} \right) - \sin 2\pi \frac{t}{T} \right\} \right] \\ &= \frac{\gamma}{2} B_0^2 q_{h1}, \end{aligned} \quad (11)$$

$$\begin{aligned} Q_{v1} &= \gamma k_v \left\{ \tan(\beta + \phi - \alpha) + \frac{1}{\tan(\beta - \alpha)} \right\} \int_0^{r_0 e^{\beta \tan \phi} \cos(\beta + \phi - \alpha)} \left[\left\{ r_0 e^{\beta \tan \phi} \cos(\beta + \phi - \alpha) - z \right\} \sin \omega \left(t - \frac{r_0 e^{\beta \tan \phi} \cos(\beta + \phi - \alpha) - z_1}{V_p} \right) \right] dz_1 \\ &= \frac{\gamma B_0^2 \eta k_v e^{2\beta \tan \phi} \cos^2(\beta + \phi - \alpha) \sin^2 \alpha}{2\pi r_0 e^{\beta \tan \phi} \cos(\beta + \phi - \alpha) \cos^2 \phi} \left\{ \tan(\beta + \phi - \alpha) + \frac{1}{\tan(\beta - \alpha)} \right\} \left[\cos 2\pi \left(\frac{t}{T} - \frac{r_0 e^{\beta \tan \phi} \cos(\beta + \phi - \alpha)}{\eta} \right) \right. \\ &\quad \left. + \frac{r_0 e^{\beta \tan \phi} \cos(\beta + \phi - \alpha)}{2\pi \eta} \left\{ \sin 2\pi \left(\frac{t}{T} - \frac{r_0 e^{\beta \tan \phi} \cos(\beta + \phi - \alpha)}{\eta} \right) - \sin 2\pi \frac{t}{T} \right\} \right] \\ &= \frac{\gamma}{2} B_0^2 q_{v1}. \end{aligned} \quad (12)$$

2.3.3. *Log-Spiral Shear Zone.* Weight of the log-spiral shear zone BDE,

$$W_2 = \frac{1}{2} \int_0^\beta r_0^2 d\theta = \frac{r_0^2 (e^{2\beta \tan \phi} - 1)}{4 \tan \phi} = \frac{B_0^2 \sin^2 \alpha (e^{2\beta \tan \phi} - 1)}{2 \sin 2\phi}. \quad (13)$$

The log-spiral zone BDE is divided into “ n ” number of slices which makes the angle of log-spiral center β into “ n ” number of $d\beta$ angles, that is, $\beta = nd\beta$, as shown in Figure 4.

Mass of strip on the i th slice of the log-spiral zone BDE,

$$m(z)_i = \frac{\gamma}{g} \frac{2\pi d\beta}{360^\circ \sin^2(\rho + (i - 0.5)d\beta)} \int_0^{H_i} z_i(z) dz, \quad (14)$$

where $H_i = (r_0/2) (e^{(i-1)d\beta \tan \phi} + e^{id\beta \tan \phi}) \sin(\rho + (i - 0.5)d\beta)$.

The acceleration at any depth z_i and time t of any i th slice of the log-spiral shear zone, below the top of the surface, can be expressed as

$$a_h(z, t)_i = k_h g \sin \omega \left(t - \frac{H_i - z_i}{V_s} \right), \quad (15)$$

$$a_v(z, t)_i = k_v g \sin \omega \left(t - \frac{H_i - z_i}{V_p} \right). \quad (16)$$

The total horizontal and vertical inertia force acting within this i th slice can be expressed as follows:

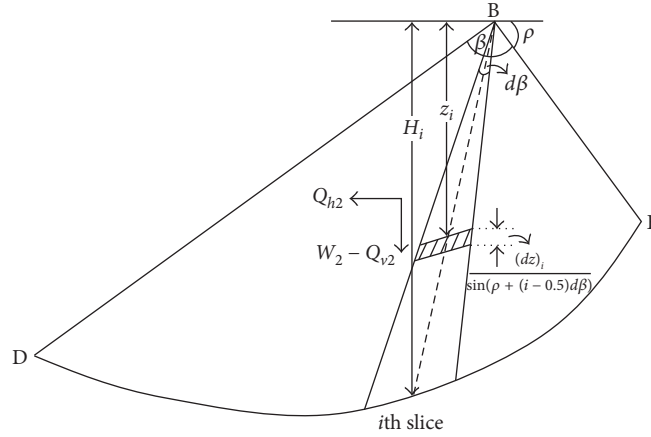


FIGURE 4: Generalized slice and centre of gravity of the log-spiral zone.

$$\begin{aligned}
 (Q_h)_i &= \frac{2\pi\gamma d\beta k_h}{360^\circ \sin^2(\rho + (i - 0.5)d\beta)} \int_0^{H_i} z_i \sin \omega \left(t - \frac{H_i - z_i}{V_s} \right) (dz)_i \\
 &= \frac{\gamma d\beta k_h \lambda B_0^2 \sin^2 \alpha (e^{(i-1)d\beta \tan \phi} + e^{id\beta \tan \phi})^2}{360^\circ * 4H_i \cos^2 \phi} \left[\frac{\lambda}{H_i 2\pi} \left\{ \sin 2\pi \frac{t}{T} - \sin 2\pi \left(\frac{t}{T} - \frac{H_i}{\lambda} \right) \right\} - \cos 2\pi \frac{t}{T} \right] \\
 &= \frac{\gamma}{2} B_0^2 q_{h2} (e^{(i-1)d\beta \tan \phi} + e^{id\beta \tan \phi})^2,
 \end{aligned} \tag{17}$$

$$\begin{aligned}
 (Q_v)_i &= \frac{2\pi\gamma d\beta k_v}{360^\circ \sin^2(\rho + (i - 0.5)d\beta)} \int_0^{H_i} z_i \sin \omega \left(t - \frac{H_i - z_i}{V_p} \right) (dz)_i \\
 &= \frac{\gamma d\beta k_v \eta B_0^2 \sin^2 \alpha (e^{(i-1)d\beta \tan \phi} + e^{id\beta \tan \phi})^2}{360^\circ * 4H_i \cos^2 \phi} \left[\frac{\eta}{H_i 2\pi} \left\{ \sin 2\pi \frac{t}{T} - \sin 2\pi \left(\frac{t}{T} - \frac{H_i}{\eta} \right) \right\} - \cos 2\pi \frac{t}{T} \right] \\
 &= \frac{\gamma}{2} B_0^2 q_{v2} (e^{(i-1)d\beta \tan \phi} + e^{id\beta \tan \phi})^2.
 \end{aligned} \tag{18}$$

Now, the total horizontal and vertical inertia force acting on log-spiral shear zone is expressed as

$$Q_{h2} = \sum_{i=1}^n (Q_h)_i = \frac{\gamma}{2} B_0^2 q_{h2} \sum_{i=1}^n (e^{(i-1)d\beta \tan \phi} + e^{id\beta \tan \phi})^2, \tag{19}$$

$$Q_{v2} = \sum_{i=1}^n (Q_v)_i = \frac{\gamma}{2} B_0^2 q_{v2} \sum_{i=1}^n (e^{(i-1)d\beta \tan \phi} + e^{id\beta \tan \phi})^2. \tag{20}$$

The incremental external works due to the foundation load P , surcharge load q , the weight of the soil wedges ABE, BCD, and BDE, and their corresponding inertial forces are

$$W_P = P_L B_0 V_1 \left[\sin(\alpha - \phi) + k_h \sin 2\pi \left(\frac{t}{T} - \frac{H}{\lambda} \right) \cos(\alpha - \phi) - k_v \sin 2\pi \left(\frac{t}{T} - \frac{H}{\eta} \right) \sin(\alpha - \phi) \right], \tag{21}$$

$$W_{ABE} = \frac{\gamma}{4} B_0^2 \frac{\sin \alpha \sin 2\rho}{\cos \phi} V_1, \tag{22}$$

$$W_{BCD} = -\frac{\gamma}{4} B_0^2 \frac{e^{3\beta \tan \phi} \sin^2 \alpha \sin 2(\beta - \alpha + \phi)}{\cos \phi \sin \xi} V_1, \tag{23}$$

$$W_Q = -\gamma D_f \frac{B_0 \sin \alpha e^{2\beta \tan \phi}}{\sin \xi} \left[\left\{ -k_h \sin 2\pi \left(\frac{t}{T} - \frac{H}{\lambda} \right) \cos(\beta - \alpha + \phi) \right\} + \left\{ \left(1 - k_v \sin 2\pi \left(\frac{t}{T} - \frac{H}{\eta} \right) \right) \sin(\beta - \alpha + \phi) \right\} \right] V_1, \tag{24}$$

$$\begin{aligned}
 W_{BDE} &= \frac{\gamma}{2} \int_0^\beta r_0^2 d\theta V_\theta \sin(\theta + \phi - \alpha) \\
 &= \frac{\gamma}{2} B_0^2 \frac{\sin^2 \alpha}{\cos^2 \phi (1 + 9 \tan^2 \phi)} \left[3 \tan \phi \left\{ e^{3\beta \tan \phi} \sin(\beta + \phi - \alpha) - \sin(\phi - \alpha) \right\} - e^{3\beta \tan \phi} \cos(\beta + \phi - \alpha) + \cos(\phi - \alpha) \right] V_1,
 \end{aligned} \tag{25}$$

$$\begin{aligned} W_{Qh} &= Q_h V_1 \cos(\alpha - \phi), \\ W_{Qv} &= -Q_v V_1 \sin(\alpha - \phi), \end{aligned} \quad (26)$$

$$\begin{aligned} W_{Qh1} &= Q_{h1} V_1 e^{\beta \tan \phi} \cos(\beta - \alpha + \phi), \\ W_{Qv1} &= Q_{v1} V_1 e^{\beta \tan \phi} \sin(\beta - \alpha + \phi), \end{aligned} \quad (27)$$

$$\begin{aligned} W_{Qh2} &= \frac{\gamma}{2} B_0^2 q_{h2} \sum_{i=1}^n \left[\left(e^{(i-1)d\beta \tan \phi} + e^{id\beta \tan \phi} \right)^2 \int_{(i-1)d\beta}^{id\beta} V_\theta \cos(\theta + \phi - \alpha) d\theta \right] \\ &= \frac{\gamma}{2} B_0^2 q_{h2} \frac{V_1}{(1 + \tan \phi)} \sum_{i=1}^n \left[\left(e^{(i-1)d\beta \tan \phi} + e^{id\beta \tan \phi} \right)^2 \left\{ e^{id\beta \tan \phi} (\sin(id\beta + \phi - \alpha) + \tan \phi \cos(id\beta + \phi - \alpha)) \right. \right. \\ &\quad \left. \left. - e^{(i-1)d\beta \tan \phi} (\sin((i-1)d\beta + \phi - \alpha) + \tan \phi \cos((i-1)d\beta + \phi - \alpha)) \right\} \right], \end{aligned} \quad (28)$$

$$\begin{aligned} W_{Qv2} &= \frac{\gamma}{2} B_0^2 q_{v2} \sum_{i=1}^n \left[\left(e^{(i-1)d\beta \tan \phi} + e^{id\beta \tan \phi} \right)^2 \int_{(i-1)d\beta}^{id\beta} V_\theta \sin(\theta + \phi - \alpha) d\theta \right] \\ &= \frac{\gamma}{2} B_0^2 q_{v2} \frac{V_1}{(1 + \tan^2 \phi)} \sum_{i=1}^n \left[\left(e^{(i-1)d\beta \tan \phi} + e^{id\beta \tan \phi} \right)^2 \left\{ e^{id\beta \tan \phi} (-\cos(id\beta + \phi - \alpha) + \tan \phi \sin(id\beta + \phi - \alpha)) \right. \right. \\ &\quad \left. \left. - e^{(i-1)d\beta \tan \phi} (-\cos((i-1)d\beta + \phi - \alpha) + \tan \phi \sin((i-1)d\beta + \phi - \alpha)) \right\} \right]. \end{aligned} \quad (29)$$

The incremental internal energy dissipation along the velocity discontinuities AE and CD and the radial line DE is

$$D_{AE} = cACV_1 \cos \phi = cB_0 \sin \rho V_1, \quad (30)$$

$$D_{CD} = cCDV_2 \cos \phi = \frac{cB_0 e^{2\beta \tan \phi} \sin \alpha \cos(\beta - \alpha + \phi)}{\sin(\beta - \alpha)} V_1, \quad (31)$$

$$D_{DE} = c \int_0^\beta r_0 d\theta V_\theta \cos \phi = \frac{cB_0 \sin \alpha (e^{2\beta \tan \phi} - 1)}{2 \tan \phi} V_1. \quad (32)$$

Equating the work expended by the external loads to the power dissipated internally for a kinematically admissible velocity field, we can get the expression of pseudodynamic ultimate bearing capacity of shallow strip footing. The classical ultimate bearing capacity equation of shallow strip footing,

$$P_L = Q_{ult} = cN_c + \gamma D_f N_q + 0.5 \gamma B_0 N_\gamma. \quad (33)$$

After solving the above equations, the simplified form of the bearing capacity coefficients is as follows:

$$N_c = \left[\frac{\sin \alpha}{2 \tan \phi} (e^{2\beta \tan \phi} - 1) + \cos(\alpha - \phi) + \frac{e^{2\beta \tan \phi} \sin \alpha \cos(\beta - \alpha + \phi)}{\sin(\beta - \alpha)} \right], \quad (34)$$

$$N_q = \left[\frac{\sin \alpha e^{2\beta \tan \phi}}{\sin \xi} \left[\left\{ -k_h \sin 2\pi \left(\frac{t}{T} - \frac{H}{\lambda} \right) \cos(\beta - \alpha + \phi) \right\} + \left\{ \left(1 - k_v \sin 2\pi \left(\frac{t}{T} - \frac{H}{\eta} \right) \right) \sin(\beta - \alpha + \phi) \right\} \right] \right], \quad (35)$$

$$\begin{aligned} N_\gamma &= \left[\frac{\sin^2 \alpha}{\cos^2 \phi (1 + 9 \tan^2 \phi)} \left[3 \tan \phi \left\{ e^{3\beta \tan \phi} \sin(\beta + \phi - \alpha) - \sin(\phi - \alpha) \right\} - e^{3\beta \tan \phi} \cos(\beta + \phi - \alpha) + \cos(\phi - \alpha) \right] \right. \\ &\quad \left. - \frac{\sin \alpha \sin 2\rho}{2 \cos \phi} + \frac{e^{3\beta \tan \phi} \sin^2 \alpha \sin 2(\beta - \alpha + \phi)}{2 \cos \phi \sin \xi} - q_h \cos(\alpha - \phi) + q_v \sin(\alpha - \phi) - q_{h1} e^{\beta \tan \phi} \cos(\beta + \phi - \alpha) - q_{v1} e^{\beta \tan \phi} \sin(\beta + \phi - \alpha) \right. \\ &\quad \left. - \frac{\sum_{i=1}^n \left(e^{(i-1)d\beta \tan \phi} + e^{id\beta \tan \phi} \right)^2}{(1 + \tan^2 \phi)} \left[q_{h2} \sum_{i=1}^n \left\{ e^{id\beta \tan \phi} (\sin(id\beta + \phi - \alpha) + \tan \phi \cos(id\beta + \phi - \alpha)) - e^{(i-1)d\beta \tan \phi} (\sin((i-1)d\beta + \phi - \alpha) \right. \right. \right. \\ &\quad \left. \left. + \tan \phi \cos((i-1)d\beta + \phi - \alpha)) \right\} + q_{v2} \sum_{i=1}^n \left\{ e^{id\beta \tan \phi} (\sin(id\beta + \phi - \alpha) + \tan \phi \cos(id\beta + \phi - \alpha)) \right. \right. \\ &\quad \left. \left. - e^{(i-1)d\beta \tan \phi} (\sin((i-1)d\beta + \phi - \alpha) + \tan \phi \cos((i-1)d\beta + \phi - \alpha)) \right\} \right] \right]. \end{aligned} \quad (36)$$

An attempt is made to present 'single seismic bearing capacity coefficient' for simultaneous resistance of unit weight, surcharge and cohesion as in a practical situation, there will be a single failure mechanism for the simultaneous resistance of unit weight, surcharge, and cohesion. So, we get

$$P_L = \frac{\gamma}{2} B_0 N. \quad (37)$$

After simplification of equations, the expression of N is given below.

$$\begin{aligned} N = & \left[\frac{\sin^2 \alpha}{\cos^2 \phi (1 + 9 \tan^2 \phi)} \left[3 \tan \phi \left\{ e^{3\beta \tan \phi} \sin (\beta + \phi - \alpha) - \sin (\phi - \alpha) \right\} - e^{3\beta \tan \phi} \cos (\beta + \phi - \alpha) + \cos (\phi - \alpha) \right] \right. \\ & + \frac{e^{3\beta \tan \phi} \sin^2 \alpha \sin 2(\beta - \alpha + \phi)}{2 \cos \phi \sin \xi} - \frac{\sin \alpha \sin 2\rho}{2 \cos \phi} + 2 \frac{D_f}{B_0} \frac{\sin \alpha e^{2\beta \tan \phi}}{\sin \xi} \left[\left\{ -k_h \sin 2\pi \left(\frac{t}{T} - \frac{H}{\lambda} \right) \cos (\beta - \alpha + \phi) \right\} \right. \\ & + \left. \left. \left\{ \left(1 - k_v \sin 2\pi \left(\frac{t}{T} - \frac{H}{\eta} \right) \right) \sin (\beta - \alpha + \phi) \right\} \right] - q_h \cos (\alpha - \phi) + q_v \sin (\alpha - \phi) - q_{h1} e^{\beta \tan \phi} \cos (\beta + \phi - \alpha) \right. \\ & - q_{v1} e^{\beta \tan \phi} \sin (\beta + \phi - \alpha) - \frac{\sum_{i=1}^n (e^{(i-1)d\beta \tan \phi} + e^{id\beta \tan \phi})^2}{(1 + \tan^2 \phi)} \left[q_{h2} \sum_{i=1}^n e^{id\beta \tan \phi} (\sin (id\beta + \phi - \alpha)) \right. \\ & + \tan \phi \cos (id\beta + \phi - \alpha) - e^{(i-1)d\beta \tan \phi} (\sin ((i-1)d\beta + \phi - \alpha) + \tan \phi \cos ((i-1)d\beta + \phi - \alpha)) \\ & + q_{v2} \sum_{i=1}^n \left\{ e^{id\beta \tan \phi} (\sin (id\beta + \phi - \alpha) + \tan \phi \cos (id\beta + \phi - \alpha)) - e^{(i-1)d\beta \tan \phi} (\sin ((i-1)d\beta + \phi - \alpha) \right. \\ & \left. \left. + \tan \phi \cos ((i-1)d\beta + \phi - \alpha)) \right\} \right] + \frac{2c}{\gamma B_0} \left\{ \frac{\sin \alpha}{2 \tan \phi} (e^{2\beta \tan \phi} - 1) + \cos (\alpha - \phi) + \frac{e^{2\beta \tan \phi} \sin \alpha \cos (\beta - \alpha + \phi)}{\sin (\beta - \alpha)} \right\} \left. \right]. \quad (38) \end{aligned}$$

Here, N is the single pseudodynamic bearing capacity coefficient of shallow strip footing under seismic loading condition. In this formulation, the objective function pseudodynamic bearing capacity coefficient depends on these Φ , c , α , β , t/T , k_h , k_v , H/λ , and H/η functions. For a particular soil and seismic condition, all other terms are constant except α , β , and t/T . So, optimization of pseudodynamic bearing capacity coefficient is done with respect to α , β , and t/T using the HSOS algorithm. The advantage of this HSOS algorithm is that it can improve the searching capability of the algorithm for attaining the global optimization. Here, the optimum value of N is represented as N_{ye} . Now, pseudodynamic ultimate bearing capacity,

$$Q_{ult} = 0.5\gamma B_0 N_{ye}. \quad (39)$$

3. The Hybrid Symbiosis Organisms Search Algorithm

The hybrid symbiosis organisms search (HSOS) algorithm is a recently developed hybrid optimization algorithm which is used to solve this pseudodynamic bearing capacity of shallow strip footing minimal optimization problem.

3.1. The Symbiosis Organisms Search Algorithm. Symbiosis organisms search (SOS) algorithm is a population-based iterative global optimization algorithm for solving global optimization problems, proposed by Cheng and Prayogo [33].

This algorithm is based on the basic concept of symbiotic relationships among the organisms in nature (ecosystem). Three types of symbiotic relationships are occurring in an ecosystem. These are mutualism relationship, commensalism relationship, and parasitism relationship. Mutualism relationship describes the relationship where both organisms get benefits from the interaction. Commensalism relationship is a symbiotic relationship between two different organisms where one organism gets the benefit and the other is not significantly affected. In the symbiotic parasitism relationship, one organism gets the benefit and the other is harmed, but not always killed. Based on the concept of three relationships, the SOS algorithm is executed. In the SOS algorithm, a group of organisms in an ecosystem is considered as a population size of the solution. Each organism is analogous to one solution vector, and the fitness value of each organism represents the degree of adaptation to the desired objective. Initially, a set of organisms in the ecosystem is generated randomly within the search region. The new candidate solution is generated through the biological interaction between two organisms in the ecosystem which contains the mutualism, commensalism, and parasitism phases, and the process of interaction is continued until the termination criterion is satisfied. A detailed description of SOS algorithm can be seen in [33].

3.2. The Simple Quadratic Interpolation (SQI) Method. In this section, the three-point quadratic interpolation is discussed.

Considering the two organisms Org_j and Org_k , where $\text{Org}_j = (\text{org}_j^1, \text{org}_j^2, \text{org}_j^3, \dots, \text{org}_j^D)$ and $\text{Org}_k = (\text{org}_k^1, \text{org}_k^2, \text{org}_k^3, \dots, \text{org}_k^D)$ from the ecosystem, the organism Org_i is updated

$$\overline{\text{Org}_i^m} = 0.5 \frac{\left((\text{Org}_i^m)^2 - (\text{Org}_j^m)^2 \right) f_k + \left((\text{Org}_j^m)^2 - (\text{Org}_k^m)^2 \right) f_i + \left((\text{Org}_k^m)^2 - (\text{Org}_i^m)^2 \right) f_j}{(\text{Org}_i^m - \text{Org}_j^m) f_k + (\text{Org}_j^m - \text{Org}_k^m) f_i + (\text{Org}_k^m - \text{Org}_i^m) f_j}, \quad (40)$$

where $m = 1, 2, 3, \dots, D$.

The SQI is intended to enhance the entire search capability of the algorithm. Here, f_i , f_j , and f_k are the fitness values of i th, j th, and k th organisms, respectively.

3.3. The Hybrid Symbiosis Organisms Search Algorithm. In the development of heuristic global optimization algorithm, the balance of exploration and exploitation capability plays a major role [43], where ‘‘Exploration is the process of visiting entirely new regions of a search space, whilst exploitation is the process of visiting those regions of a search space within the neighborhood of previously visited points’’ [43]. As discussed above, the SQI method may be used for the better exploration when executing the optimization process. On the other hand, Cheng and Prayoga [33] have elaborately discussed the better exploitation ability of SOS for global optimization. To balance the exploration capability of SQI and the exploitation potential of SOS, the hybrid symbiosis organisms search (HSOS) algorithm has been proposed. This hybrid method can increase the robustness as well as the searching capability of the algorithm for attaining the global optimization. By incorporating the SQI into the SOS algorithm, the HSOS algorithm is developed and the flowchart of the HSOS algorithm is shown in Figure 5. The HSOS algorithm is able to explore the new search region with the SOS algorithm and to exploit the population information with the SQI.

If an organism is going to an infeasible region, then the organism is reflected back to the feasible region using the following equation [44]:

$$\text{Org}_i = \begin{cases} \text{UB}_i + \text{rand}(0, 1) * (\text{UB}_i - \text{LB}_i) & \text{if } \text{Org}_i < \text{LB}_i, \\ \text{UB}_i - \text{rand}(0, 1) * (\text{UB}_i - \text{LB}_i) & \text{if } \text{Org}_i > \text{UB}_i, \end{cases} \quad (41)$$

where LB_i and UB_i are, respectively, the lower and upper bounds of the i th organism.

The algorithmic steps of hsos are given below:

Step 1. Ecosystem initialization: initialize the algorithm parameters and ecosystem organisms and evaluate the fitness value for each corresponding organism.

Step 2. Main loop.

Step 2.1. Mutualism phase: select one organism Org_j randomly from the ecosystem. The organism Org_i intersects with

according to the three-point quadratic interpolation [40]. The three-point approximate minimal point for organism Org_i is determined by the following equation:

the organism Org_j and then they try to improve the survival capabilities in the ecosystem. The new organism for each of Org_i and Org_j is calculated by the following equations:

$$\text{Org}_i^{\text{new}} = \text{Org}_i + \text{rand}(0, 1) * (\text{Org}_{\text{best}} - \text{Mutual}_{\text{Vector}} * \text{BF1}), \quad (42)$$

$$\text{Org}_j^{\text{new}} = \text{Org}_j + \text{rand}(0, 1) * (\text{Org}_{\text{best}} - \text{Mutual}_{\text{Vector}} * \text{BF2}), \quad (43)$$

where $\text{Mutual}_{\text{Vector}} = (\text{Org}_i + \text{Org}_j)/2$. Here, BF1 and BF2 are called the benefit factors, the value of which be either 1 or 2. The level of benefits of the organism represents these factors, that is, whether an organism gets, respectively, partial or full benefit from the interaction. Org_{best} is the best organism in the ecosystem. $\text{Mutual}_{\text{Vector}}$ represents the relationship characteristic between the organisms Org_i and Org_j .

Step 2.2. Commensalism phase: between the interaction of the organisms Org_i and Org_j , the organism Org_i gets benefit by the organism Org_j and try to improve the beneficial advantage in the ecosystem to the higher degree of adaption. The new organism Org_i is determined by the following equation:

$$\text{Org}_i^{\text{new}} = \text{Org}_i + \text{rand}(-1, 1) * (\text{Org}_{\text{best}} - \text{Org}_j), \quad (44)$$

where $i \neq j$ and Org_{best} is the best organism in the ecosystem.

Step 2.3. Parasitism phase: by duplicating randomly selected dimensions of the organism Org_j , an artificial parasite (Parasite_Vector) is created. From the ecosystem, another organism Org_i is selected randomly that is treated as a host to the Parasite_Vector. If the objective function value of the Parasite_Vector is better than the organism Org_i , it can kill the organism Org_i and adopt its position in the ecosystem. If the objective function value of Org_i is better than the Parasite_Vector, Org_i will have resistance to the parasite and the Parasite_Vector will not be able to reside in that ecosystem.

Step 2.4. Simple quadratic interpolation: the two organisms Org_j and Org_k ($j \neq k$) are selected randomly from the ecosystem, and then the organism Org_i is updated by quadratic interpolation passing through these three organisms which can be expressed by (40).

Step 3. If the stopping criteria are not satisfied to go to Step 2, then it will proceed until the best objective function value is obtained.

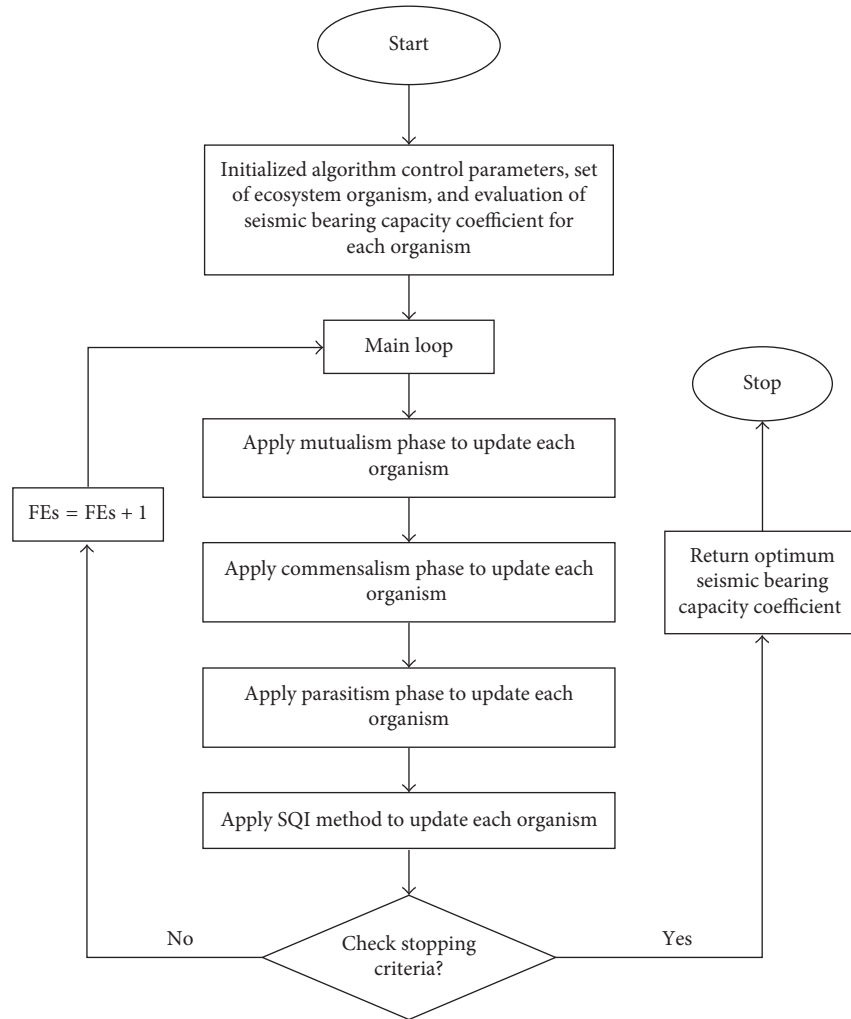


FIGURE 5: Flowchart of the HSOS algorithm.

4. Discussion on Results Obtained by the HSOS Algorithm

The pseudodynamic bearing capacity coefficient (N_{ye}) has been optimized using the HSOS algorithm with respect to α , β , and t/T variables. The algorithm was performed with 1000 fitness evaluations, 30 independent runs, and 50 eco-sizes. The best result has been taken among these 30 results. This optimized single seismic bearing capacity coefficient (N_{ye}) is presented in Tables 1 and 2 for static and seismic conditions ($k_{hi} = 0.1, 0.2, \text{ and } 0.3$), respectively, which can be used by the field engineers in earthquake-prone areas for the simultaneous resistance of unit weight, surcharge, and cohesion.

4.1. Parametric Study. In this section, a brief parametric study and a comparative study have been presented. The effect of soil friction angle (Φ), depth factor (D_f/B_0), cohesion factor ($2c/\gamma B_0$), and seismic accelerations (k_{hi} and k_v) on normalized reduction factor (N_{ye}/N_{ys}) is discussed. Normalized reduction factor (N_{ye}/N_{ys}) is the ratio of optimized seismic and static bearing capacity coefficient. The variations of parameters are as follows: $\Phi = 20^\circ, 30^\circ, \text{ and } 40^\circ$; $k_{hi} = 0.1, 0.2, \text{ and } 0.3$; $k_v = 0$,

TABLE 1: Static condition.

Φ	$2c/\gamma B_0$	D_f/B_0			
		0.25	0.5	0.75	1
20°	0	8.349	11.756	15.087	18.377
	0.25	11.175	14.488	17.769	21.029
	0.5	13.886	17.155	20.407	23.649
30°	0	30.439	40.168	49.719	59.177
	0.25	35.903	45.497	54.975	64.391
	0.5	41.263	50.771	60.189	69.557
40°	0	144.24	178.37	211.78	244.89
	0.25	157.48	191.17	224.5	257.5
	0.5	170.47	203.94	237.1	270.1

$k_{hi}/2$, and k_{hi} ; $2c/\gamma B_0 = 0, 0.25, \text{ and } 0.5$; and $D_f/B_0 = 0.25, 0.75, 0.5, \text{ and } 1$. A detailed comparative study with other available previous research is also discussed in this section.

4.1.1. Effect on N_{ye}/N_{ys} due to Variation of Φ . Figure 6 shows the variations of the normalized reduction factor (N_{ye}/N_{ys}) with respect to horizontal seismic acceleration (k_{hi}) at different soil friction angles ($\Phi = 20^\circ, 30^\circ, \text{ and } 40^\circ$) at

TABLE 2: Pseudodynamic bearing capacity coefficient (N_{γ_e}) for $k_h=0.1, 0.2,$ and 0.3 .

Φ	$2c/\gamma B_0$	$k_h=0.1$											
		$k_v=0$				$k_v=k_h/2$				$k_v=k_h$			
		D_f/B_0				D_f/B_0				D_f/B_0			
		0.25	0.5	0.75	1	0.25	0.5	0.75	1	0.25	0.5	0.75	1
20°	0	5.881	8.559	11.172	13.753	5.882	8.538	11.128	13.687	5.878	8.51	11.079	13.614
	0.25	8.589	11.17	13.73	16.277	8.69	11.247	13.782	16.303	8.797	11.323	13.832	16.329
	0.5	11.146	13.688	16.224	18.754	11.331	13.851	16.359	18.865	11.523	14.015	16.502	18.98
30°	0	21.98	29.575	37.021	44.385	22.107	29.638	37.028	44.331	22.223	29.691	37.07	44.243
	0.25	26.85	34.306	41.675	48.996	27.128	34.529	41.834	49.081	27.415	34.739	41.979	49.169
	0.5	31.59	38.965	46.287	53.564	32.016	39.325	46.573	53.793	32.447	39.688	46.879	54.028
40°	0	101.41	127.17	152.55	177.72	102.32	127.86	153.02	177.89	103.17	128.49	153.41	178.11
	0.25	112.36	137.9	163.11	188.16	113.51	138.82	163.85	188.69	114.74	139.83	164.61	189.16
	0.5	123.12	148.5	173.67	198.58	124.63	149.79	174.65	199.42	126.15	151.03	175.72	200.21
Φ	$2c/\gamma B_0$	$k_h=0.2$											
		$k_v=0$				$k_v=k_h/2$				$k_v=k_h$			
		D_f/B_0				D_f/B_0				D_f/B_0			
		0.25	0.5	0.75	1	0.25	0.5	0.75	1	0.25	0.5	0.75	1
20°	0	3.627	5.554	7.437	9.299	3.495	5.257	7.019	8.781	3.45	5.049	6.644	8.24
	0.25	6.254	8.093	9.926	11.754	6.276	8.01	9.739	11.464	6.345	7.94	9.535	11.131
	0.5	8.672	10.493	12.312	14.129	8.889	10.605	12.321	14.036	9.201	10.801	12.394	13.987
30°	0	14.856	20.524	26.077	31.56	14.451	19.881	25.193	30.44	13.88	19.024	24.045	29.002
	0.25	19.156	24.697	30.169	35.606	19.026	24.314	29.539	34.734	18.803	23.785	28.716	33.621
	0.5	23.312	28.779	34.201	39.615	23.416	28.634	33.811	38.98	23.505	28.422	33.304	38.169
40°	0	68.468	87.465	106.13	124.61	67.336	85.521	103.4	121.14	65.74	82.948	99.846	116.59
	0.25	77.438	96.227	114.79	133.22	76.783	94.766	112.51	130.11	75.728	92.708	109.51	126.1
	0.5	86.315	104.98	123.41	141.79	86.076	103.87	121.54	139.08	85.49	102.38	119.02	135.61
Φ	$2c/\gamma B_0$	$k_h=0.3$											
		$k_v=0$				$k_v=k_h/2$				$k_v=k_h$			
		D_f/B_0				D_f/B_0				D_f/B_0			
		0.25	0.5	0.75	1	0.25	0.5	0.75	1	0.25	0.5	0.75	1
20°	0	2.843	4.058	5.268	6.471	4.291	5.476	6.642	7.792	—	—	—	—
	0.25	5.178	6.389	7.592	8.794	9.036	10.181	11.325	12.468	—	—	—	—
	0.5	7.51	8.713	9.915	11.118	13.713	14.848	15.984	17.119	—	—	—	—
30°	0	9.3	13.312	17.24	21.118	8.356	11.737	15.116	18.496	8.15	10.853	13.557	16.261
	0.25	13.109	17	20.856	24.684	12.336	15.716	19.085	22.433	12.366	15.074	17.783	20.492
	0.5	16.736	20.57	24.389	28.195	16.285	19.633	22.96	26.286	16.541	19.25	21.958	24.667
40°	0	44.498	58.106	71.465	84.714	40.605	52.714	64.622	76.375	35	45.195	55.199	65.068
	0.25	51.859	65.283	78.574	91.7	48.428	60.359	72.112	83.809	43.394	53.371	63.261	73.021
	0.5	59	72.396	85.56	98.686	56.083	67.85	79.556	91.165	51.543	61.416	71.164	80.912

$2c/\gamma B_0=0.25$, $D_f=0.5$, and $k_v=k_h/2$. It is seen that the normalized reduction factor ($N_{\gamma_e}/N_{\gamma_s}$) increases with increase in soil friction angle (Φ). Due to an increase in Φ , the internal resistance of the soil particles will be increased, which resembles the fact that there is an increase in the seismic bearing capacity factor.

4.1.2. *Effect on $N_{\gamma_e}/N_{\gamma_s}$ due to Variation of $2c/\gamma B_0$.* Figure 7 shows the variations of the normalized reduction factor ($N_{\gamma_e}/N_{\gamma_s}$) with respect to seismic acceleration (k_h) at different cohesion factors ($2c/\gamma B_0=0, 0.25,$ and 0.5) at $\Phi=30^\circ$, $D_f/B_0=0.5$, and $k_v=k_h/2$. It is seen that the normalized reduction factor ($N_{\gamma_e}/N_{\gamma_s}$) increases with an increase in the cohesion factor ($2c/\gamma B_0$). Due to an increase in cohesion, the seismic bearing capacity factor will be increased as the increase in cohesion causes an increase in intermolecular

attraction among the soil particle, which offers more resistance against the shearing failure of the foundation.

4.1.3. *Effect on $N_{\gamma_e}/N_{\gamma_s}$ due to Variation of D_f/B_0 .* Figure 8 shows the variations of the normalized reduction factor ($N_{\gamma_e}/N_{\gamma_s}$) with respect to seismic acceleration (k_h) for different depth factors ($D_f/B_0=0.25, 0.5,$ and 1) at $\Phi=30^\circ$, $2c/\gamma B_0=0.25$, and $k_v=k_h/2$. It is seen that the normalized reduction factor ($N_{\gamma_e}/N_{\gamma_s}$) increases with an increase in the depth factor (D_f/B_0). Due to an increase in the depth factor (D_f/B_0), surcharge weight increases, which increases the passive resistance and hence increases the seismic bearing capacity factor.

4.1.4. *Effect on $N_{\gamma_e}/N_{\gamma_s}$ due to Variation of Seismic Accelerations (k_h and k_v).* From Figures 6–9, it is seen that the normalized reduction factor ($N_{\gamma_e}/N_{\gamma_s}$) decreases along

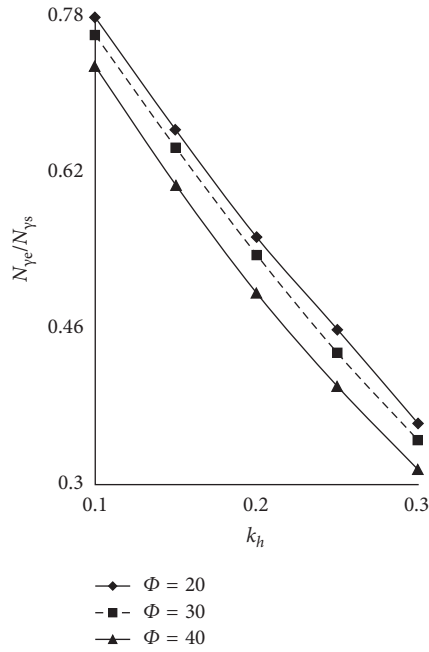


FIGURE 6: The variations of the bearing capacity coefficient with respect to seismic acceleration (k_h) at different soil friction angles ($\Phi = 20^\circ, 30^\circ,$ and 40°) for $2c/B_0 = 0.25, D_f/B_0 = 0.5,$ and $k_v = k_h/2$.

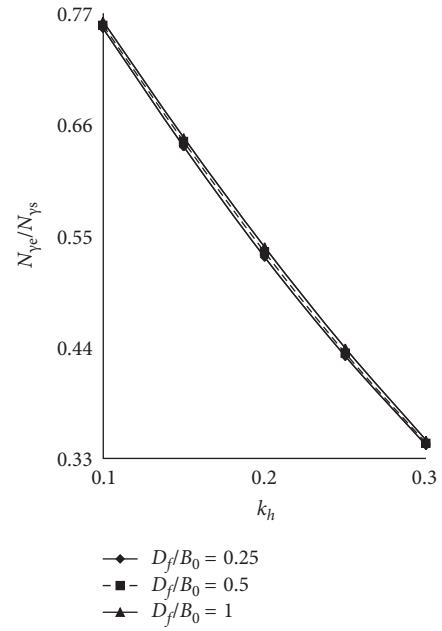


FIGURE 8: The variations of the bearing capacity coefficient with respect to seismic acceleration (k_h) at different depth factors ($D_f/B_0 = 0.25, 0.5,$ and 1) for $\Phi = 30^\circ, \delta = \Phi/2, 2c/B_0 = 0.25,$ and $k_v = k_h/2$.

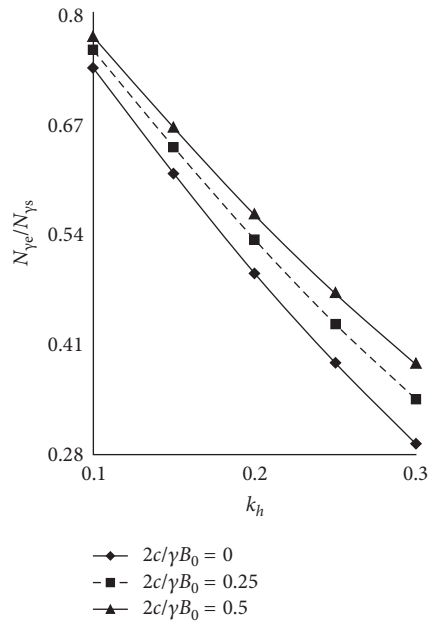


FIGURE 7: The variations of the bearing capacity coefficient with respect to seismic acceleration (k_h) at different cohesion factors ($2c/B_0 = 0, 0.25,$ and 0.5) for $\Phi = 30^\circ, \delta = \Phi/2, D_f/B_0 = 0.5,$ and $k_v = k_h/2$.

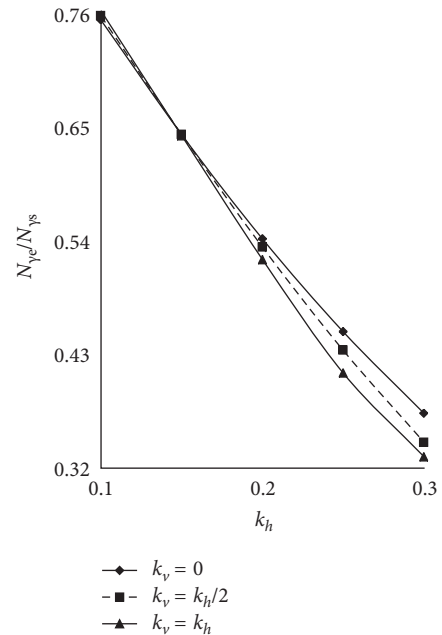


FIGURE 9: The variations of the bearing capacity coefficient with respect to seismic acceleration (k_h) at different vertical seismic accelerations ($k_v = 0, k_h/2,$ and k_h) for $\Phi = 30^\circ, 2c/B_0 = 0.25, D_f/B_0 = 0.5,$ and $\delta = \Phi/2$.

with an increase in horizontal seismic acceleration (k_h). And Figure 9 shows the variations of the normalized reduction factor ($N_{\gamma e}/N_{\gamma s}$) with respect to seismic acceleration (k_h) at different vertical seismic accelerations ($k_v = 0, k_h/2,$ and k_h) for $\Phi = 30^\circ, D_f = 0.5,$ and $2c/\gamma B_0 = 0.25$. It is seen that the normalized reduction factor ($N_{\gamma e}/N_{\gamma s}$) decreases with the increase

in vertical seismic acceleration (k_v) also. Due to an increase in seismic acceleration and due to the sudden movement of different waves, the disturbance in the soil particles increases, which allows more soil mass to participate in the vibration and hence decreases its resistance against bearing capacity.

4.1.5. Comparison of Result. A detailed comparative study of the present analysis with previous research on similar type of works with different approaches is done here. Figure 10 and Table 3 show the comparison of a pseudodynamic bearing capacity coefficient obtained from the present analysis with previous seismic analyses with respect to different seismic accelerations ($k_h = 0.1, 0.2,$ and 0.3) for $\Phi = 30^\circ$. It is seen that, for the lower value of seismic accelerations here in Figure 10, $k_h = 0.2$, the values obtained from the present study are less than the values obtained from Soubra [10] (M1 and M2) [17]. But when horizontal seismic acceleration increases from 0.2, the bearing capacity coefficient also increases gradually, and at $k_h = 0.3$, the present analysis provides greater value in comparison to all the compared methods. At $k_h = 0.1$, around 7.5%, 24%, and 29% decrease in N_{ye} coefficient, and at $k_h = 0.2$, around 2%, 15%, and 12% decrease in N_{ye} coefficient in comparison to that in Soubra [10] (M1 and M2) and Ghosh [17], respectively. But at $k_h = 0.3$, it increases around 26%, 16%, and 48%, respectively, in comparison with the respective analyses.

The performance results, that is, pseudodynamic bearing capacity coefficients obtained by the HSOS algorithm are compared with other metaheuristic optimization algorithms. Table 4 shows the performance result obtained by DE [45], PSO [46], ABC [47], HS [48], BSA [49], ABSA [50], SOS [33], and HSOS [39] algorithms at different conditions that are compared here. From this table, it is observed that the performance result, that is, pseudodynamic bearing capacity coefficient (N_{ye}) obtained from this HSOS algorithm is lesser than the other compared algorithms in different soil and seismic conditions. From the above investigations, it can be said that HSOS algorithm can satisfactorily be used to evaluate the seismic bearing capacity of shallow strip footing suggested here.

5. Numerical Analysis

The numerical modeling of dynamic analysis of shallow strip footing is performed using a finite element software, PLAXIS 2D (v-8.6), which is equipped with features to deal with various aspects of complex structures and study the soil-structure interaction effect. In addition to static loads, the dynamic module of PLAXIS also provides a powerful tool for modeling the dynamic response of a soil structure during an earthquake.

5.1. Numerical Modeling. A two-dimensional geometrical model is prepared that is to be composed of points, lines, and other components in the x - y plane. The PLAXIS mesh generator based on the input of the geometry model automatically performs the generation of a mesh at an element level. The shallow strip footing was modeled as a plane strain, and 15 noded triangular elements are used to simulate the foundation soil. The extension of the mesh was taken 100 m wide and 30 m depth as the earthquake forces cannot affect the vertical boundaries. Standard earthquake boundaries are applied for earthquake loading conditions using SMC files, and then the mesh is generated. Cluster refinement of the

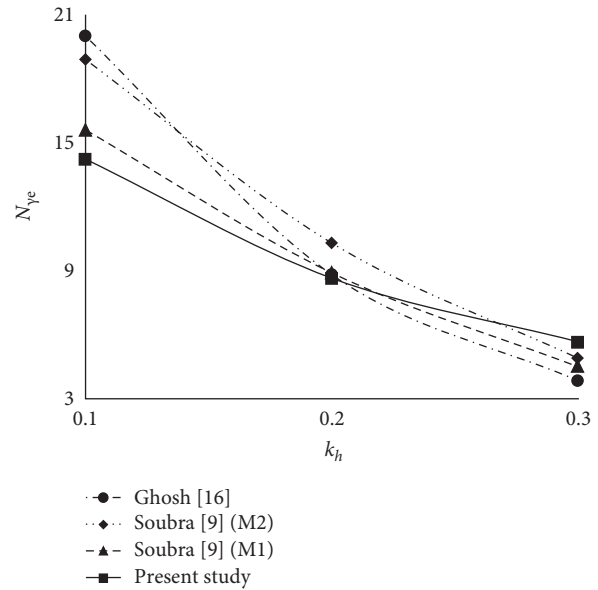


FIGURE 10: The comparison of pseudodynamic bearing capacity coefficient obtained from present analysis with previous seismic analyses with respect to different seismic accelerations ($k_h = 0.1, 0.2,$ and 0.3) for $\Phi = 30^\circ$.

mesh is followed to obtain precise medium-sized mesh. HS small model was used to incorporate dynamic soil properties of the soil samples. Two different soil samples were used to analyze the shallow strip footing under seismic loading condition as shown in Table 5. A uniformly distributed load of 100 kN/m applying on the section of the foundation along with different surcharge loads to represent the load coming from superstructure is analyzed in this paper as shown in Figure 11. Initial stresses are generated after turning off the initial pore water pressure tool.

5.2. Calculation. During the calculation stage, three steps are adopted where, in the first step, calculations are done for plastic analysis where applied vertical load and weight of soil are activated. In the second step, calculations are made for dynamic analysis where earthquake data are incorporated as SMS file. And, in the final step, FOS is determined by the c - Φ reduction method. El Salvador 2001 earthquake data (moment magnitude, $M_w = 7.6$) are given as input in the dynamic calculation as SMC file as shown in Figure 12. The vertical settlement of the foundation and the corresponding factor at safety of each condition obtained from the numerical modeling are obtained. Figures 13 and 14 show the deformed mesh and vertical displacement contour, respectively, after undergoing staged calculations.

5.3. Numerical Validation. Finite element model of shallow strip footing embedded in c - Φ soil is analyzed in PLAXIS-8.6v for the validation of the analytical solution. The results obtained from this analytical analysis are compared with the numerical solutions to validate the analysis. At first,

TABLE 3: Comparison of seismic bearing capacity coefficient (N_{γ_e}) for different values of k_h and k_v with $\Phi = 30^\circ$.

k_h	Present study		Ghosh [17]		Budhu and Al-Karni [7]		Choudhury and Subba Rao [13]		Soubra [10]	
	$k_v = k_h/2$	$k_v = k_h$	$k_v = k_h/2$	$k_v = k_h$	$k_v = k_h/2$	$k_v = k_h$	$k_v = k_h/2$	$k_v = k_h$	M1	M2
0.1	14.43	14.23	20.39	20.04	10.21	9.46	8.4	7.76	15.6	18.9
0.2	8.78	8.65	9.98	8.82	3.81	2.86	2.85	2	8.9	10.3
0.3	5.68	5.67	3.85	2.35	1.21	0.56	0.98	0.29	4.5	4.9

TABLE 4: Comparison of seismic bearing capacity coefficient (N_{γ_e}) obtained by different standard algorithms.

Φ	k_h	DE	PSO	ABC	HS	BSA	ABSA	SOS	HSOS
(a) $2c/\gamma B_0 = 0.25$, $D_f/B_0 = 0.5$, and $k_v = k_h/2$									
20°	0.1	11.54	11.771	11.255	11.62	11.25	11.284	11.248	11.247
	0.2	8.714	8.524	8.11	8.73	8.1	8.51	8.02	8.01
30°	0.1	34.681	34.854	34.535	34.942	34.53	34.591	34.53	34.529
	0.2	24.514	24.641	24.319	24.43	24.319	24.361	24.32	24.314
40°	0.1	138.90	139.12	138.85	139.54	138.83	138.99	138.9	138.82
	0.2	94.768	95.546	94.78	94.89	94.77	94.82	94.77	94.766
(b) $2c/\gamma B_0 = 0.5$, $D_f/B_0 = 0.75$, and $k_v = k_h/2$									
20°	0.1	16.46	16.363	16.359	16.512	16.37	16.45	16.361	16.359
	0.2	12.53	12.325	12.581	12.524	12.33	12.812	12.324	12.321
30°	0.1	46.91	46.579	46.942	46.76	46.59	46.751	46.575	46.573
	0.2	33.931	33.823	34.15	33.99	33.83	33.97	33.816	33.811
40°	0.1	174.76	174.68	174.691	174.93	174.67	174.81	174.69	174.65
	0.2	121.69	121.59	121.61	121.59	121.58	121.561	121.58	121.54

TABLE 5: HS small model soil parameters for PLAXIS-8.6v.

Sample	γ (kPa)	c (kPa)	Φ	ψ	ν	E_{50}^{ref} (kPa)	$E_{\text{oed}}^{\text{ref}}$ (kPa)	$E_{\text{ur}}^{\text{ref}}$ (kPa)	m	G_0 (kPa)	$\gamma_{0.7}$
S1	20.9	0.5	32	2	0.2	1.00E+4	1.00E+4	3.00E+4	0.5	1.00E+5	1.00E-4
S2	19.9	0.2	28	0	0.2	1.25E+4	1.00E+4	3.75E+4	0.5	1.30E+5	1.25E-4

settlement of foundation is calculated analytically using two classical equations, such as

Richards et al.'s [12] seismic settlement equation:

$$s_e = 0.174 \frac{V^2}{Ag} \left[\frac{k_h}{A} \right]^{-4} \tan \alpha_{\text{AE}}, \quad (45)$$

where V is the peak velocity for the design earthquake (m/sec), A is the acceleration coefficient for the design earthquake, and g is the acceleration due to gravity, and the value of α_{AE} depends on Φ and critical acceleration k_h^* .

Terzaghi's [2] immediate settlement equation:

$$s_i = q_n B_0 \frac{(1 - \nu^2)}{E} I_f, \quad (46)$$

where q_n is the net foundation pressure, $q_n = [Q_{\text{ult}} - \gamma D_f]/\text{FOS}$, ν is the Poisson ratio, E is the Young modulus of soil, and I_f is the influence factor for shallow strip footing. Here, Q_{ult} is the pseudodynamic ultimate bearing capacity which is obtained from (39).

The dynamic soil properties taken in numerical modeling [Plaxis-8.6v] are used same in the analytical formulation to

validate it. Results obtained from the analytical solution and numerical modeling have been tabulated in Table 6. Two different types of soil models have been analyzed. Settlement of shallow foundation for the corresponding soil model is calculated using (41) and (42). Settlement values obtained from the finite element model in PLAXIS are also tabulated. It is seen that settlement obtained from analytical solution is slightly in lower side in comparison with the settlement obtained from PLAXIS-8.6v as in the analytical settlement calculation, the only initial settlement is considered. So, the formulation of pseudodynamic bearing capacity is well justified after the numerical validation.

6. Conclusion

Using the pseudodynamic approach, the effect of the shear wave and primary wave velocities traveling through the soil layer and the time and phase difference along with the horizontal and vertical seismic accelerations are used to evaluate the seismic bearing capacity of the shallow strip footing. A mathematical formulation is suggested for simultaneous resistance of unit weight, surcharge and cohesion

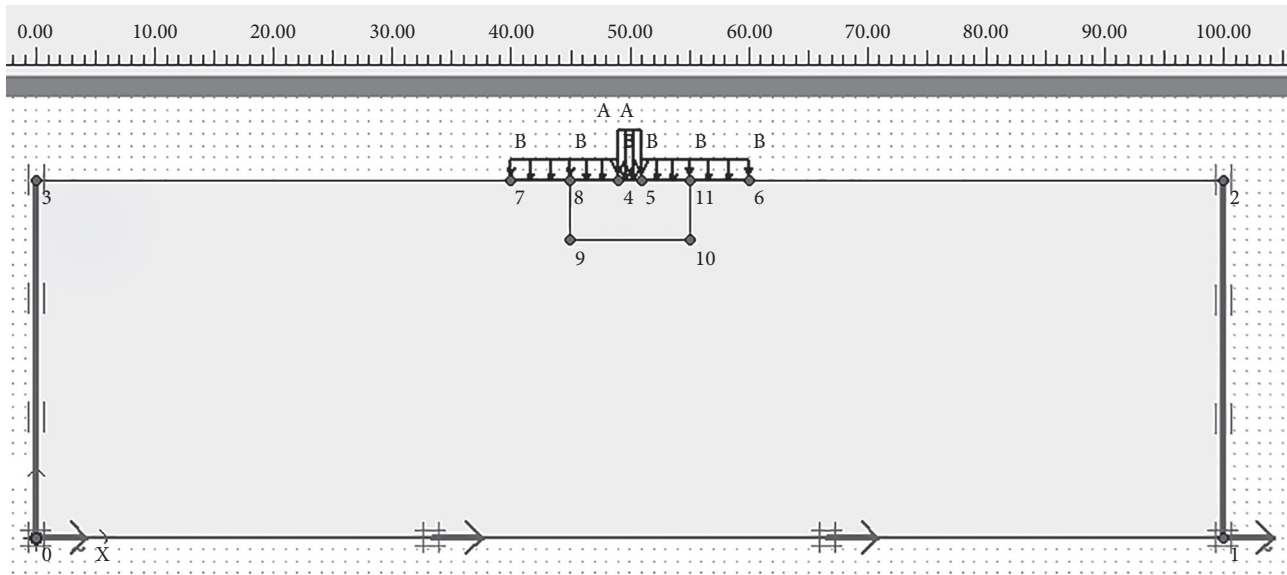


FIGURE 11: Finite element geometry and foundation load along with surcharge load.

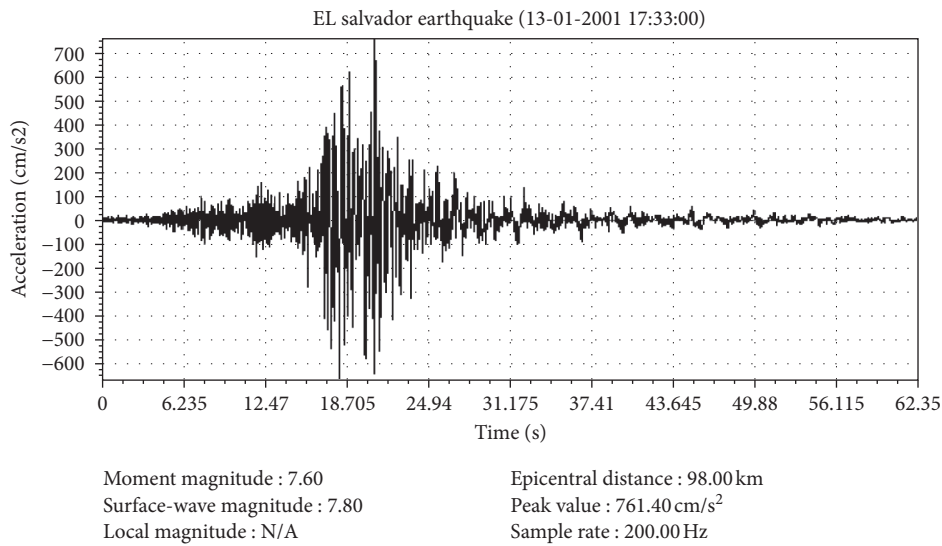


FIGURE 12: El Salvador 2001 earthquake data.

using upper-bound limit analysis method. A composite failure mechanism which includes both planer and log-spiral zone is considered here to develop this mathematical model for the shallow strip footing resting on $c-\Phi$ soil. The HSOS algorithm is used to solve this problem. The advantage of this HSOS algorithm is that it can improve the searching capability of the algorithm for attaining the global optimum. From the comparison, the results obtained by the HSOS algorithm with other standard algorithms show the acceptability of the results in all soil and seismic conditions. Hence, using the HSOS algorithm, the coefficient of seismic bearing capacity is presented in a tabular form. Numerical modeling of shallow strip footing is also analyzed using PLAXIS-8.6v software for the validation of the analytical solution. It is observed that the results obtained from this

analytical analysis are well justified with the numerical solutions. The effect of various parameters such as soil friction angle (Φ), seismic accelerations (k_h and k_v), cohesion factor ($2c/\gamma B_0$), and depth factor (D_f/B_0) is studied here. It is seen that the pseudodynamic bearing capacity coefficient (N_{ye}) increases with the increase in Φ , $2c/\gamma B_0$, and D_f/B_0 , but it decreases with the increase in horizontal and vertical seismic accelerations (k_h and k_v). The values obtained from the present analysis are thoroughly compared with the available pseudostatic analysis as well as pseudodynamic analysis values, and it is seen that the values obtained from the present study are comparable reasonably. Using the values as provided in Tables 1 and 2, the ultimate bearing capacity of foundation under seismic loading condition can be evaluated.

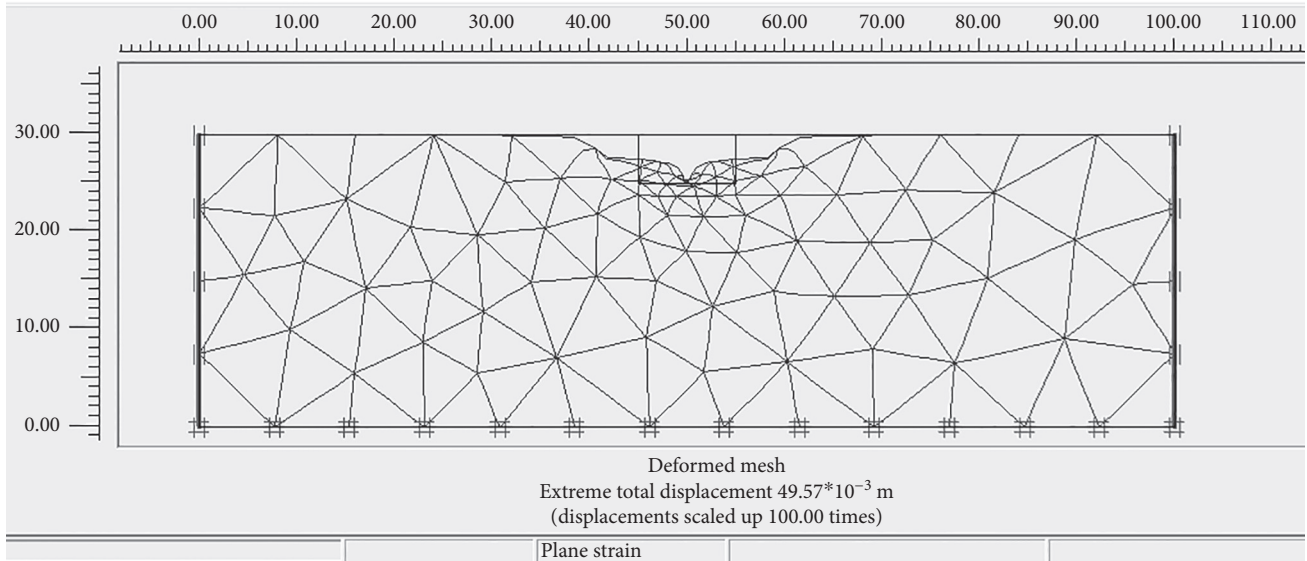


FIGURE 13: The deformed mesh of model after calculation.

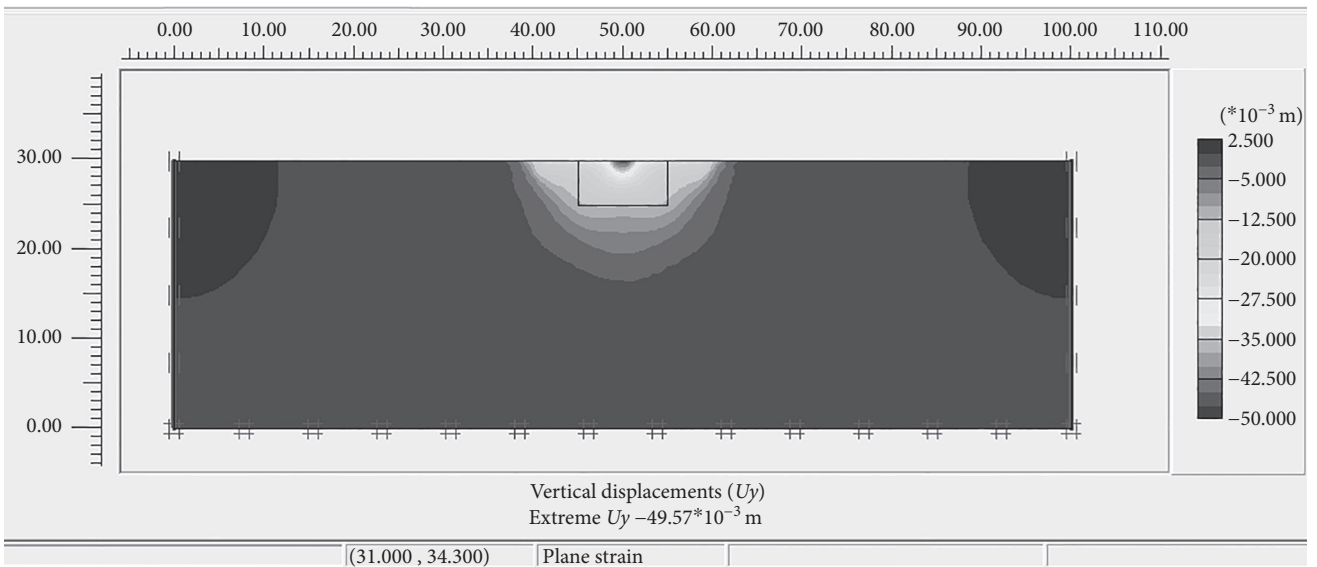


FIGURE 14: Vertical displacement contour after calculation.

TABLE 6: Comparison of settlements obtained from numerical and analytical analyses.

Soil samples	Depth factor (D_f/B_0)	Numerical solution			Analytical solution		
		PLAXIS-8.6v		Richards et al. [12]	Present analysis		Terzaghi [2]
		FOS	Settlement (mm)	k_h^*	Settlement (mm)	N_{ye}	Settlement (mm)
Sample 1	0	1.12	49.57	0.02	127	41	48.97
	0.25	1.95	42.82	0.14	18.27	53	36.01
	0.5	2.71	41.47	0.24	10.65	68	33.07
	1	3.19	40.1	0.28	9.13	75	30.61
Sample 2	0	1.03	47.45	0.01	255	37	36.6
	0.25	1.59	40.99	0.1	25.58	49	31.08
	0.5	2.14	38.22	0.18	18.27	64	30.0
	1	2.61	34.47	0.25	10.23	72	27.33

Nomenclature

$2c/\gamma B_0$:	Cohesion factor
B_0 :	Width of the footing
C :	Cohesion of soil
D_f :	Depth of footing below ground surface
D_f/B_0 :	Depth factor
g :	Acceleration due to gravity
G :	Shear modulus of soil
k_h, k_v :	Horizontal and vertical seismic accelerations
N_c, N_q, N_γ :	Bearing capacity coefficients
$N_{\gamma e}$:	Optimized single seismic bearing capacity coefficient
$N_{\gamma s}$:	Optimized single static bearing capacity coefficient
$N_{\gamma e}/N_{\gamma s}$:	Normalized reduction factor
PL:	Uniformly distributed column load
q :	Surcharge loadings
r_0, r :	Initial and final radii of the log-spiral zone (i.e., BE and BD), respectively
t :	Time of vibration
T :	Period of lateral shaking
V_1, V_2 , and V_θ :	Absolute and relative velocities, respectively
V_p :	Primary wave velocity
V_s :	Shear wave velocity
α_1, α_2 :	Base angles of triangular elastic zone under the foundation
β :	Angle that makes the log-spiral part in log-spiral mechanism
γ :	Unit weight of soil medium
λ, η :	Lame's constant
ν :	Poisson's ratio of the soil medium
Φ :	Angle of internal friction of the soil
ω :	Angular frequency
SOS:	Symbiosis organisms search
SQI:	Simple quadratic interpolation
HSOS:	Hybrid symbiosis organisms search.

Conflicts of Interest

The authors declare that there are no conflicts of interest regarding the publication of this paper.

References

- [1] L. Prandtl, "Über die Eindringungstestigkeit Plastischer Baustoffe und Die Festigkeit von Schneiden," *Zeitschrift Für Angewandte Mathematik und Mechanik*, vol. 1, no. 1, pp. 15–30, 1921, (in German).
- [2] K. Terzaghi, *Theoretical Soil Mechanics*, John Wiley & Sons, New York, NY, USA, 1943.
- [3] G. G. Meyerhof, "The ultimate bearing capacity of foundations on slopes," in *Proceedings of the 4th International Conference on Soil Mechanics and Foundation Engineering*, pp. 384–386, London, UK, August 1957.
- [4] G. G. Meyerhof, "Some recent research on the bearing capacity of foundations," *Canadian Geotechnical Journal*, vol. 1, no. 1, pp. 16–26, 1963.
- [5] A. S. Vesic, "Analysis of ultimate loads of shallow foundations," *Journal of the Soil Mechanics and Foundations Division*, vol. 99, no. 1, pp. 45–43, 1973.
- [6] S. Saran and R. K. Agarwal, "Bearing capacity of eccentrically obliquely loaded footing," *Journal of Geotechnical Engineering*, vol. 117, no. 11, pp. 1669–1690, 1991.
- [7] M. Budhu and A. Al-Karni, "Seismic bearing capacity of soils," *Geotechnique*, vol. 43, no. 1, pp. 181–187, 1993.
- [8] L. Dormieux and A. Pecker, "Seismic bearing capacity of foundation on cohesionless soil," *Journal of Geotechnical Engineering*, vol. 121, no. 3, pp. 300–303, 1995.
- [9] A. H. Soubra, "Discussion of "seismic bearing capacity and settlements of foundations"," *Journal of Geotechnical Engineering*, vol. 120, no. 9, pp. 1634–1636, 1994.
- [10] A. H. Soubra, "Seismic bearing capacity of shallow strip footings in seismic conditions," *Proceedings of the Institution of Civil Engineers-Geotechnical Engineering*, vol. 125, no. 4, pp. 230–241, 1997.
- [11] A. H. Soubra, "Upper bound solutions for bearing capacity of foundations," *Journal of Geotechnical and Geoenvironmental Engineering*, vol. 125, no. 1, pp. 59–69, 1999.
- [12] R. Richards, D. G. Elms, and M. Budhu, "Seismic bearing capacity and settlements of foundations," *Journal of Geotechnical Engineering*, vol. 119, no. 4, pp. 662–674, 1993.
- [13] D. Choudhury and K. S. Subba Rao, "Seismic bearing capacity of shallow strip footings," *Geotechnical and Geological Engineering*, vol. 23, no. 4, pp. 403–418, 2005.
- [14] J. Kumar and P. Ghosh, "Seismic bearing capacity for embedded footing on sloping ground," *Geotechnique*, vol. 56, no. 2, pp. 133–140, 2006.
- [15] A. H. Shafiee and M. Jahanandish, "Seismic bearing capacity factors for strip footings," in *Proceedings of the National Congress on Civil Engineering*, Ferdowsi University of Mashhad, Mashhad, Iran, 2010.
- [16] D. Chakraborty and J. Kumar, "Seismic bearing capacity of shallow embedded foundations on a sloping ground surface," *International Journal of Geomechanics*, vol. 15, no. 1, p. 04014035, 2014.
- [17] P. Ghosh, "Upper bound solutions of bearing capacity of strip footing by pseudo-dynamic approach," *Acta Geotechnica*, vol. 3, pp. 115–123, 2008.
- [18] A. Saha and S. Ghosh, "Pseudo-dynamic analysis for bearing capacity of foundation resting on $c-\Phi$ soil," *International Journal of Geotechnical Engineering*, vol. 9, no. 4, pp. 379–387, 2014.
- [19] A. Sengupta and A. Upadhyay, "Locating the critical failure surface in a slope stability analysis by genetic algorithm," *Applied Soft Computing*, vol. 9, no. 1, pp. 387–392, 2009.
- [20] Y. M. Cheng, L. Chi, S. Li, and W. B. Wei, "Particle swarm optimization algorithm for location of critical non-circular failure surface in two-dimensional slope stability analysis," *Computer and Geotechnics*, vol. 34, no. 2, pp. 92–103, 2007.
- [21] S. K. Das, "Slope stability analysis using genetic algorithm," *Electronic Journal of Geotechnical Engineering*, vol. 10A, 2005.
- [22] K. Deb and M. Goyal, "Optimizing engineering designs using combined genetic search," in *Proceedings of Seventh International Conference on Genetic Algorithms*, pp. 512–528, Michigan State University, East Lansing, MI, 1997.
- [23] A. H. Gandomi, A. R. Kashani, M. Mousavi, and M. Jalalvandi, "Slope stability analyzing using recent swarm intelligence techniques," *International Journal for Numerical and Analytical Methods in Geomechanics*, vol. 39, no. 3, pp. 295–309, 2015.

- [24] A. T. C. Goh, "Genetic algorithm search for critical slip surface in multiple-wedge stability analysis," *Canadian Geotechnical Journal*, vol. 36, pp. 382–391, 1999.
- [25] K. S. Kahatadeniya, P. Nanakorn, and K. M. Neaupane, "Determination of the critical failure surface for slope stability analysis using ant colony optimization," *Engineering Geology*, vol. 108, no. 1-2, pp. 133–141, 2009.
- [26] Y.-C. Li, Y.-M. Chen, T. L. T. Zhan, D.-S. Ling, and P. J. Cleall, "An efficient approach for locating the critical slip surface in slope stability analysis using a real-coded genetic algorithm," *Canadian Geotechnical Journal*, vol. 47, no. 7, pp. 806–820, 2010.
- [27] P. McCombie and P. Wilkinson, "The use of the simple genetic algorithm in finding the critical factor of safety in slope stability analysis," *Computers and Geotechnics*, vol. 29, no. 8, pp. 699–714, 2002.
- [28] A. R. Zolfaghari, A. C. Heath, and P. F. McCombie, "Simple genetic algorithm search for critical non-circular failure surface in slope stability analysis," *Computer and Geotechnics*, vol. 32, no. 3, pp. 139–152, 2005.
- [29] M. Ghazavi and S. Bazzazian Bonab, Optimization of reinforced concrete retaining walls using ant colony method, in *Proceedings of the 3rd International Symposium on Geotechnical Safety and Risk (ISGSR 2011)*, N. Vogt, B. Schuppener, D. Straub, and G. Bräu, Eds., Bundesanstalt für Wasserbau, Munich, Germany, June 2011.
- [30] S. Nama, A. K. Saha, and S. Ghosh, "Parameters optimization of geotechnical problem using different optimization algorithm," *Geotechnical and Geological Engineering*, vol. 33, no. 5, pp. 1235–1253, 2015.
- [31] S. Nama, A. K. Saha, and S. Ghosh, "Improved backtracking search algorithm for pseudo dynamic active earth pressure on retaining wall supporting $c-\Phi$ backfill," *Applied Soft Computing Journal*, vol. 52, pp. 885–897, 2017.
- [32] L. Li and F. Liu, *Group Search Optimization for Applications in Structural Design*, Springer-Verlag, Berlin, Heidelberg, Germany, 2011.
- [33] M.-Y. Cheng and D. Prayogo, "Symbiotic organisms search: a new metaheuristic optimization algorithm," *Computers & Structures*, vol. 139, pp. 98–112, 2014.
- [34] S. Nama, A. K. Saha, and S. Ghosh, "Improved symbiotic organisms search algorithm for solving unconstrained function optimization," *Decision Science Letters*, vol. 5, no. 2016, pp. 361–380, 2016.
- [35] M. Abdullahi, M. A. Ngadi, and S. M. Abdulhamid, "Symbiotic organism search optimization based task scheduling in cloud computing environment," *Future Generation Computer Systems*, vol. 56, pp. 640–650, 2016.
- [36] G. G. Tejani, V. J. Savsanin, and V. K. Patel, "Adaptive symbiotic organisms search (SOS) algorithm for structural design optimization," *Journal of Computational Design and Engineering*, vol. 3, no. 3, pp. 226–249, 2016.
- [37] M. Y. Cheng, D. Prayogo, and D. H. Tran, "Optimizing multiple-resources leveling in multiple projects using discrete symbiotic organisms search," *Journal of Computing in Civil Engineering*, vol. 30, no. 3, 2016.
- [38] D. Prasad and V. Mukherjee, "A novel symbiotic organisms search algorithm for optimal power flow of power system with FACTS devices," *Engineering Science and Technology, An International Journal*, vol. 19, no. 1, pp. 79–89, 2016.
- [39] S. Nama, A. K. Saha, and S. Ghosh, "A hybrid symbiosis organisms search algorithm and its application to real world problems," *Memetic Computing*, vol. 9, no. 3, pp. 261–280, 2017.
- [40] K. Deep and K. N. Das, "Quadratic approximation based hybrid genetic algorithm for function optimization," *Applied Mathematics and Computation*, vol. 203, no. 1, pp. 86–98, 2008.
- [41] A. Saha and S. Ghosh, "Pseudo-dynamic bearing capacity of shallow strip footing resting on $c-\Phi$ soil considering composite failure surface: bearing capacity analysis using pseudo-dynamic method," *International Journal of Geotechnical Earthquake Engineering*, vol. 6, no. 2, pp. 12–34, 2015.
- [42] W. F. Chen and X. L. Liu, *Limit Analysis in Soil Mechanics*, Elsevier Science Publications Company, New York, NY, USA, 1990.
- [43] M. Crepinšek, S. H. Liu, and M. Mernik, "Exploration and exploitation in evolutionary algorithms: a survey," *ACM Computing Surveys*, vol. 45, no. 3, p. 33, 2013.
- [44] W. Gong, Z. Cai, and C. X. Ling, "DE/BBO: a hybrid differential evolution with biogeography-based optimization for global numerical optimization," *Soft Computing*, vol. 15, pp. 645–665, 2011.
- [45] R. Storn and K. Price, "Differential evolution—a simple and efficient heuristic for global optimization over continuous spaces," *Journal of Global Optimization*, vol. 11, no. 4, pp. 341–359, 1997.
- [46] Y. Shi and R. Eberhart, "A modified particle swarm optimizer," in *Proceedings of the IEEE World Congress on Computational Intelligence Evolutionary Computation*, Anchorage, AK, USA, 1998.
- [47] D. Karaboga and B. Basturk, "A powerful and efficient algorithm for numerical function optimization: artificial bee colony (ABC) algorithm," *Journal of Global Optimization*, vol. 39, no. 3, pp. 459–471, 2007.
- [48] M. Mahdavi, M. Fesanghary, and E. Damangir, "An improved harmony search algorithm for solving optimization problems," *Applied Mathematics and Computation*, vol. 188, no. 2, pp. 1567–1579, 2007.
- [49] P. Civicioglu, "Backtracking search optimization algorithm for numerical optimization problems," *Applied Mathematics and Computation*, vol. 219, no. 15, pp. 8121–8144, 2013.
- [50] H. Duan and Q. Luo, "Adaptive backtracking search algorithm for induction magnetometer optimization," *IEEE Transactions on Magnetics*, vol. 50, no. 12, pp. 1–6, 2014.

Research Article

Optimum Design of Braced Steel Space Frames including Soil-Structure Interaction via Teaching-Learning-Based Optimization and Harmony Search Algorithms

Ayşe T. Daloglu ¹, Musa Artar ², Korhan Ozgan ¹, and Ali İ. Karakas ¹

¹Department of Civil Engineering, Karadeniz Technical University, Trabzon, Turkey

²Department of Civil Engineering, Bayburt University, Bayburt, Turkey

Correspondence should be addressed to Korhan Ozgan; korhanozgan@yahoo.com

Received 19 August 2017; Revised 13 November 2017; Accepted 6 December 2017; Published 3 April 2018

Academic Editor: Moacir Kriпка

Copyright © 2018 Ayşe T. Daloglu et al. This is an open access article distributed under the Creative Commons Attribution License, which permits unrestricted use, distribution, and reproduction in any medium, provided the original work is properly cited.

Optimum design of braced steel space frames including soil-structure interaction is studied by using harmony search (HS) and teaching-learning-based optimization (TLBO) algorithms. A three-parameter elastic foundation model is used to incorporate the soil-structure interaction effect. A 10-storey braced steel space frame example taken from literature is investigated according to four different bracing types for the cases with/without soil-structure interaction. X, V, Z, and eccentric V-shaped bracing types are considered in the study. Optimum solutions of examples are carried out by a computer program coded in MATLAB interacting with SAP2000-OAPI for two-way data exchange. The stress constraints according to AISC-ASD (American Institute of Steel Construction-Allowable Stress Design), maximum lateral displacement constraints, interstorey drift constraints, and beam-to-column connection constraints are taken into consideration in the optimum design process. The parameters of the foundation model are calculated depending on soil surface displacements by using an iterative approach. The results obtained in the study show that bracing types and soil-structure interaction play very important roles in the optimum design of steel space frames. Finally, the techniques used in the optimum design seem to be quite suitable for practical applications.

1. Introduction

Optimum design of steel structures prevents excessive consumption of the steel material. Suitable cross sections must be selected automatically from a predefined list. Moreover, selected profiles should satisfy some required constraints such as stress, displacement, and geometric size. Metaheuristic search techniques are highly preferred for problems with discrete design variables. There are many metaheuristic techniques developed recently. Some of them are genetic algorithm, harmony search algorithm, tabu search algorithm, particle swarm optimization, ant colony algorithm, artificial bee colony algorithm, teaching-learning-based optimization, simulated annealing algorithm, bat-inspired algorithm, cuckoo search algorithm, and evolutionary structural optimization. In literature, there are many studies available for the optimum design of structures using

these algorithms. For example, Daloglu and Armutcu [1] used the genetic algorithm method for the optimum design of plane steel frames. Kameshki and Saka [2] carried out the optimum design of nonlinear steel frames with semirigid connections using the genetic algorithm. Lee and Geem [3] developed a new structural optimization method based on the harmony search algorithm. Hayalioglu and Degertekin [4] applied genetic optimization on minimum cost design of steel frames with semirigid connections and column bases. Kelesoglu and Ülker [5] searched for multiobjective fuzzy optimization of space trusses by MS Excel. Degertekin [6] compared simulated annealing and genetic algorithms for the optimum design of nonlinear steel space frames. Esen and Ülker [7] optimized multistorey space steel frames considering the nonlinear material and geometrical properties. Saka [8] used the harmony search algorithm method to get the optimum design of steel sway frames

in accordance with BS5950. Degertekin and Hayalioglu [9] applied the harmony search algorithm for minimum cost design of steel frames with semirigid connections and column bases. Hasancebi et al. [10] investigated non-deterministic search techniques in the optimum design of real-size steel frames. Hasançebi et al. [11] used the simulated annealing algorithm in structural optimization. Hasancebi et al. [12] investigated the optimum design of high-rise steel buildings using an evolutionary strategy integrated with parallel algorithm. Togan [13] used one of the latest stochastic methods, teaching-learning-based optimization, for design of planar steel frames. Aydogdu and Saka [14] used ant colony optimization for irregular steel frames including the elemental warping effect. Dede and Ayvaz [15] studied structural optimization problems using the teaching-learning-based optimization algorithm. Dede [16] applied teaching-learning-based optimization on the optimum design of grillage structures with respect to LRFD-AISC. Hasançebi et al. [17] used a bat-inspired algorithm for structural optimization. Saka and Geem [18] prepared an extensive review study on mathematical and metaheuristic applications in design optimization of steel frame structures. Hasançebi and Çarbaş [19] studied the bat-inspired algorithm for discrete-size optimization of steel frames. Dede [20] focused on the application of the teaching-learning-based optimization algorithm for the discrete optimization of truss structures. Azad and Hasancebi [21] focused on discrete-size optimization of steel trusses under multiple displacement constraints and load case using the guided stochastic search technique. Artar and Daloğlu [22] obtained the optimum design of composite steel frames with semirigid connections and column bases. Artar [23] used the harmony search algorithm for the optimum design of steel space frames under earthquake loading. Artar [24] used the teaching-learning-based optimization algorithm for the optimum design of braced steel frames. Carbas [25] studied design optimization of steel frames using an enhanced firefly algorithm. Daloglu et al. [26] investigated the optimum design of steel space frames including soil-structure interaction. Saka et al. [27] researched metaheuristics in structural optimization and discussions on the harmony search algorithm. Aydogdu [28] used a biogeography-based optimization algorithm with Levy flights for cost optimization of reinforced concrete cantilever retaining walls under seismic loading.

In literature, there are several researches available for optimum structural design, as mentioned above. On the other hand, there are a few researches on the optimum design of braced steel space frames including soil-structure interaction. So, this study investigates a 10-storey braced steel space frame structure studied previously in literature, which is investigated for four different bracing types and soil-structure interaction. These bracing types are X, V, Z, and eccentric V-shaped bracings. Optimum design solutions are obtained using a computer program developed in MATLAB [29] interacting with SAP2000-OAPI (open application programming interface) [30]. Suitable cross sections are automatically selected from a list including 128 W profiles taken from AISC (American Institute of Steel Construction). The frame model

is subjected to wind loads according to ASCE7-05 [31] as well as dead, live, and snow loads. The analysis results are found to be quite consistent with the literature results. In this study, the vertical displacements on soil surfaces are also calculated. It is observed that minimum weights of space frames vary depending on the bracing type. Also, it can be concluded that incorporation of soil-structure interaction results in heavier steel weight.

2. Optimum Design Formulation

The optimum design problem of braced steel space frames is calculated as follows:

$$\min W = \sum_{k=1}^{ng} A_k \sum_{i=1}^{nk} \rho_i L_i, \quad (1)$$

where W is the weight of the frame, A_k is the cross-sectional area of group k , ρ_i and L_i are the density and length of member i , ng is the total number of groups, and nk is the total number of members in group k .

The stress constraints according to AISC-ASD [32] are defined as follows:

$$g_i(x) = \left[\frac{f_a}{F_a} + \frac{C_{mx} f_{bx}}{(1 - (f_a/F'_{ex})) F_{bx}} \right] - 1.0 \leq 0, \quad i = 1, \dots, nc,$$

$$g_i(x) = \left[\frac{f_a}{0.60 F_y} + \frac{f_{bx}}{F_{bx}} \right] - 1.0 \leq 0, \quad i = 1, \dots, nc. \quad (2)$$

If $(f_a/F_a) \leq 0.15$, instead of using (2), the stress constraint is calculated as follows:

$$g_i(x) = \left[\frac{f_a}{F_a} + \frac{f_{bx}}{F_{bx}} \right] - 1.0 \leq 0, \quad i = 1, \dots, nc, \quad (3)$$

where nc is the total number of members subjected to both axial compression and bending stresses, f_a is the computed axial stress, F_a is the allowable axial stress under axial compression force alone, f_{bx} is the computed bending stress due to bending of the member about its major (x), F_{bx} is the allowable compressive bending stress about major, F'_{ex} is the Euler stress, F_y is the yield stress of the steel, and C_{mx} is a factor. It is calculated from $C_{mx} = 0.6 - 0.4(M1/M2)$ for the braced frame member without transverse loading between the ends and $C_{mx} = 1 + \psi(f_a/F'_e)$ for the braced frame member with transverse loading.

The effective length factors of columns in braced frames are calculated as follows [33]:

$$K = \frac{3G_A G_B + 1.4(G_A + G_B) + 0.64}{3G_A G_B + 2.0(G_A + G_B) + 1.28}, \quad (4)$$

where G_A and G_B are the relative stiffness factors at the Ath and Bth ends of columns.

The maximum lateral displacement and interstorey drift constraints are defined as follows:

$$g_{jl}(x) = \frac{\delta_{jl}}{\delta_{ju}} - 1 \leq 0, \quad j = 1, \dots, m, \quad l = 1, \dots, nl, \quad (5)$$

where δ_{jl} is the displacement of the j th degree of freedom under load case l , δ_{ju} is the displacement at the upper bound, m is the number of restricted displacements, and nl is the total number of loading cases.

$$g_{jil}(x) = \frac{\Delta_{jil}}{\Delta_{ju}} - 1 \leq 0, \quad j = 1, \dots, ns, \quad i = 1, \dots, nsc, \quad (6)$$

$$l = 1, \dots, nl,$$

where Δ_{jil} is the interstorey drift of the i th column in the j th storey under load case l , Δ_{ju} is the limit value, ns is the number of storeys, and nsc is the number of columns in a storey.

The beam-to-column connection geometric constraint is determined as follows:

$$g_{bf,i}(x) = \frac{b'_{fbk,i}}{d_{c,i} - 2t_{fl,i}} - 1 \leq 0, \quad i = 1, \dots, n_{bw}, \quad (7)$$

$$g_{bb,i}(x) = \frac{b_{fbk,i}}{b_{fck,i}} - 1 \leq 0, \quad i = 1, \dots, n_{bf},$$

where n_{bw} is the number of joints where beams are connected to the web of the column, $b'_{fbk,i}$ is the flange width of the beam, $d_{c,i}$ is the depth of the column, $t_{fl,i}$ is the flange thickness of the column, n_{bf} is the number of joints where beams are connected to the flange of the column, and $b_{fbk,i}$ and $b_{fck,i}$ are flange widths of the beam and column, respectively (Figure 1).

3. Three-Parameter Vlasov Elastic Foundation Model

The soil reaction exerted on a structure resting on a two-parameter elastic soil is expressed in

$$q_z = kw - 2t\nabla^2 w. \quad (8)$$

The reaction depends on the soil surface vertical displacement w , soil reaction modulus k , and soil shear parameter $2t$. These two soil parameters, k and $2t$, can be defined by

$$k = \int_0^H \frac{E_s(1-\nu_s)}{(1+\nu_s)(1-2\nu_s)} \cdot \left(\frac{\partial \phi(z)}{\partial z} \right)^2 dz, \quad (9)$$

$$2t = \int_0^H G_s \phi(z)^2 dz,$$

in which H , ν_s , and G_s are the depth, Poisson's ratio, and shear modulus of the soil, respectively. In most of the classical two-parameter soil foundation models such as Pasternak, Hetenyi, and Vlasov models, the soil parameters are constants obtained by experimental tests or arbitrarily defined. However, it is highly difficult to determine these

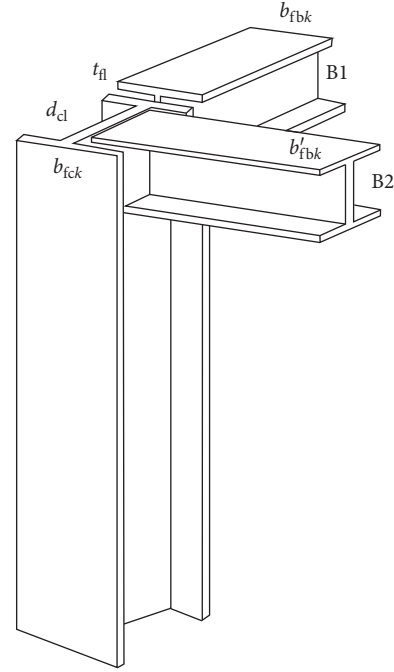


FIGURE 1: Beam-to-column connection geometric constraints.

parameters experimentally. Therefore, Vallabhan and Daloglu [34] developed an additional parameter γ to characterize the vertical displacement profile within subsoil. They called this model including the third parameter γ as a three-parameter Vlasov model. This model eliminates the necessity of experimental tests to determine soil parameters since these values are determined iteratively in terms of the new parameter, γ . The vertical deformation profile of the subsoil is described via a mode shape function as given in

$$\phi(z) = \frac{\sinh \gamma(1-(z/H))}{\sinh \gamma}. \quad (10)$$

The boundary values of $\phi(z)$ are assumed to be $\phi(0) = 1$ and $\phi(H) = 0$, as shown in Figure 2. The γ parameter can be calculated using

$$\left(\frac{\gamma}{H} \right)^2 = \frac{(1-2\nu_s)}{2(1-\nu_s)} \cdot \frac{\int_{-\infty}^{+\infty} \int_{-\infty}^{+\infty} (\nabla w)^2 dx dy}{\int_{-\infty}^{+\infty} \int_{-\infty}^{+\infty} w^2 dx dy}. \quad (11)$$

Equation (9) indicates that the soil parameters (k and $2t$) are calculated based on the material properties and mode shape function ($\phi(z)$). Also, it is necessary to compute the γ parameter to calculate the mode shape function. It is necessary to know the soil vertical surface displacements obtained from the structural analysis to calculate the γ parameter. So, it can be stated that k , $2t$, ϕ , γ , and w are interdependent. That is why the analysis requires an iterative procedure. For this purpose, a computer program is coded in MATLAB interacting with SAP2000 structural analysis program via OAPI (open application programming interface) to perform this iterative procedure in the three-parameter foundation model.

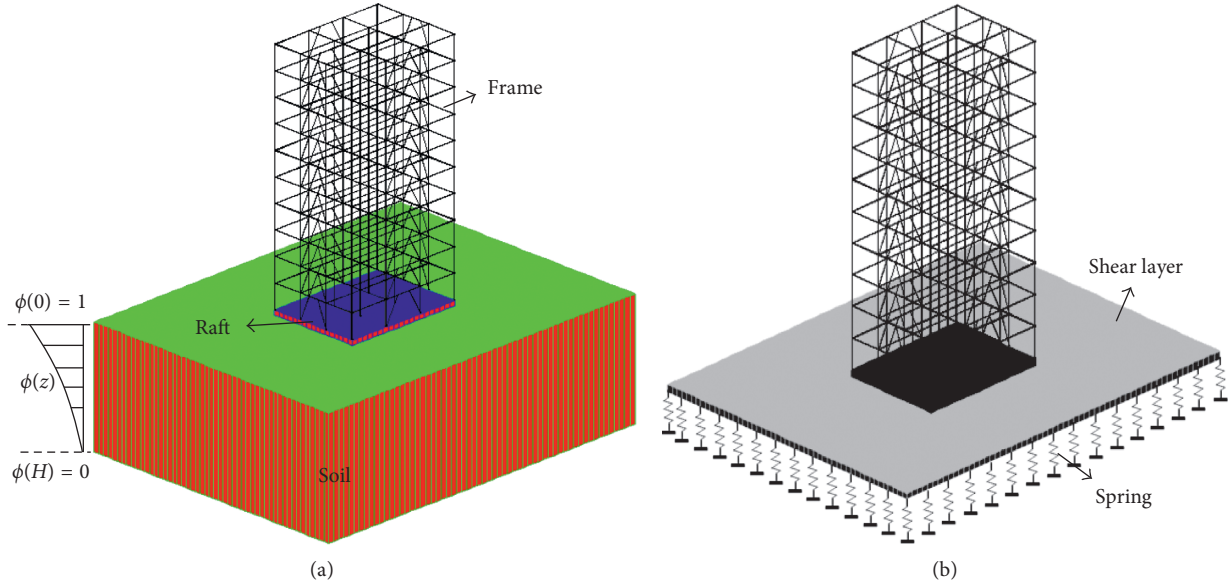


FIGURE 2: A space frame on three-parameter elastic foundation. (a) 3D frame on elastic subsoil. (b) Mathematical model.

Using the coded program, a soil model is generated such that the soil reaction modulus k is represented by elastic area springs. The interaction between springs is taken into account using shell elements connecting the top of springs. The soil shell element with one degree of freedom at each node reflects only shear behavior of the soil. The γ parameter is computed numerically in the coded program using the vertical displacements of soil shell elements. To determine the soil parameters iteratively, $\gamma = 1$ is assumed initially and k and $2t$ values are calculated. Then, the structural model is analyzed using SAP2000, and the soil surface vertical displacements are retrieved to compute a new γ value. The difference between successive values of γ is calculated and checked whether it is within a prescribed tolerance or not. If it is smaller than the tolerance, the iteration is terminated. Otherwise, the next iteration is performed, and the procedure is repeated until the convergence is fulfilled.

4. Optimization Algorithms

4.1. Harmony Search Algorithm. Harmony search (HS) algorithm method is developed by Lee and Geem [3] and mimics improvisation procedures of musical harmony. It consists of three basic procedures. Operations are conducted by the harmony memory (HM) matrix. In the first step, HM is randomly and automatically filled by the program coded in MATLAB. The form of harmony memory matrix is shown as follows:

$$H = \begin{bmatrix} x_1^1 & x_2^1 & \cdots & x_{n-1}^1 & x_n^1 \\ x_1^2 & x_2^2 & \cdots & x_{n-1}^2 & x_n^2 \\ \vdots & \vdots & \vdots & \vdots & \vdots \\ x_1^{\text{HMS}-1} & x_2^{\text{HMS}-1} & \cdots & x_{n-1}^{\text{HMS}-1} & x_n^{\text{HMS}-1} \\ x_1^{\text{HMS}} & x_2^{\text{HMS}} & \cdots & x_{n-1}^{\text{HMS}} & x_n^{\text{HMS}} \end{bmatrix} \rightarrow \begin{matrix} \varphi(x^1) \\ \varphi(x^2) \\ \vdots \\ \varphi(x^{\text{HMS}-1}) \\ \varphi(x^{\text{HMS}}) \end{matrix}, \quad (12)$$

where x_i^j is the i th design variable of the j th solution vector, n is the total number of design variables, $\varphi(x^j)$ is the j th objective function value, and HMS (harmony memory size) indicates a specified number of solutions. In the harmony memory matrix, each row presents design variables.

In the second step, the objective function values ($\varphi(x^1), \varphi(x^2), \dots, \varphi(x^{\text{HMS}-1}), \varphi(x^{\text{HMS}})$) of solution vectors in the harmony memory matrix are determined. In the third step, a new solution vector ($x^{\text{nh}} = [x_1^{\text{nh}}, x_2^{\text{nh}}, \dots, x_n^{\text{nh}}]$) is prepared by selecting each design variable from either the harmony memory matrix or the entire section list X_{sl} . Harmony memory consideration rate (HMCR) is applied as follows:

$$\begin{aligned} x_i^{\text{nh}} &\in \{x_i^1, x_i^2, \dots, x_i^{\text{HMS}}\} \text{ with probability of HMCR} \\ x_i^{\text{nh}} &\in X_{\text{sl}} \text{ with probability of } (1 - \text{HMCR}). \end{aligned} \quad (13)$$

Also, the new value of the design variable selected from the harmony memory matrix is checked whether this value should be pitch adjusted or not depending on the pitch adjustment ratio (PAR). This decision is determined as follows:

$$\begin{aligned} &\text{Yes, with probability of PAR} \\ &\text{No, with probability of } 1 - \text{PAR}. \end{aligned} \quad (14)$$

Detailed information about the HS algorithm can be found in the literature [3, 8, 9, 23].

4.2. Teaching-Learning-Based Optimization. Teaching-learning-based optimization (TLBO) was developed by Rao et al. [35]. This method mimics teaching and learning processes between a teacher and students in classroom. The person having the highest information in the class is selected as a teacher. The teacher gives his/her information to the other

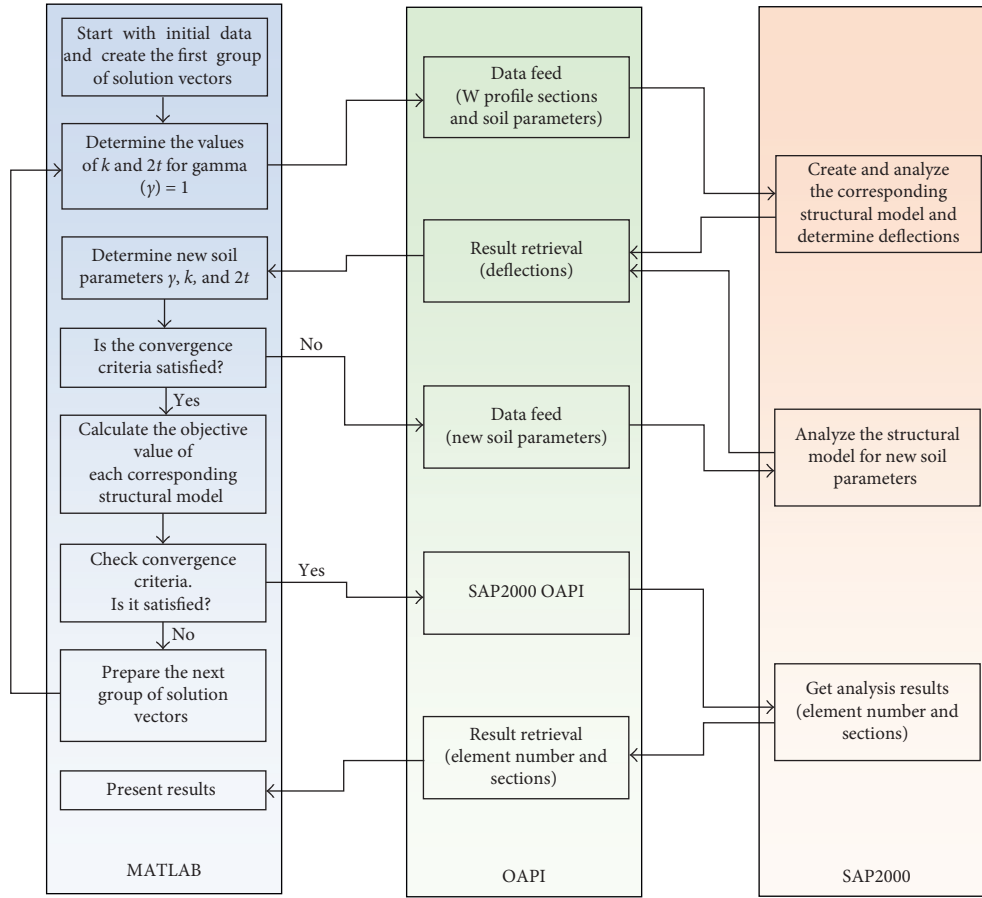


FIGURE 3: Flowchart for the optimum design algorithm by HS and TLBO for space frames on elastic foundation.

people (students) in the class. These procedures provide suitable solutions in structural optimizations. The teaching-learning-based optimization method consists of two basic steps such as teaching and learning. In the first step, the teaching step, the first population (class) is randomly filled in the matrix form presented as follows:

$$\text{class (population)} = \begin{bmatrix} x_1^1 & x_2^1 & \dots & x_{n-1}^1 & x_n^1 \\ x_1^2 & x_2^2 & \dots & x_{n-1}^2 & x_n^2 \\ \vdots & \vdots & \vdots & \vdots & \vdots \\ x_1^{S-1} & x_2^{S-1} & \dots & x_{n-1}^{S-1} & x_n^{S-1} \\ x_1^S & x_2^S & \dots & x_{n-1}^S & x_n^S \end{bmatrix} \rightarrow \begin{matrix} f(x^1) \\ f(x^2) \\ \vdots \\ f(x^{S-1}) \\ f(x^S) \end{matrix}, \quad (15)$$

where each row represents a student and gives a design solution, S is the population size (the number of students), n is the number of design variables, and $f(x^{1,2,\dots,S})$ is the unconstrained objective function value of each student in the class. The student in a class having the best information is selected as a teacher of the class. His or her objective function value is the minimum in the class. The information update of students in the class is carried out with the help of the teacher as follows:

$$x^{\text{new},i} = x^i + r(x_{\text{teacher}} - T_F x_{\text{mean}}), \quad (16)$$

where $x^{\text{new},i}$ is the new student, x^i is the current student, r is a random number in the range $[0,1]$, and T_F , a teaching factor, is either 1 or 2. x_{mean} is the mean of the class defined as $x_{\text{mean}} = (\text{mean}(x_1), \dots, \text{mean}(x_S))$. If the new student has better information ($f(x^{\text{new},i})$), the new student is replaced with the current student. In the second step, the learning step, information is shared between students. This step is similar to the first step. If the new student presents a better information, he/she is replaced with the current student. The information update of students in the class is carried out as follows:

$$\begin{aligned} \text{if } f(x^i) < f(x^j) &\Rightarrow x^{\text{new},i} = x^i + r(x^i - x^j), \\ \text{if } f(x^i) > f(x^j) &\Rightarrow x^{\text{new},i} = x^i + r(x^j - x^i). \end{aligned} \quad (17)$$

The detailed information about the TLBO algorithm can be obtained from [13, 15, 16, 20, 24, 35]. The flowchart of processes in MATLAB-SAP2000 OAPI developed to get optimum solutions is presented in Figure 3.

5. Design Example

A 10-storey braced steel space frame example taken from literature [36] is studied considering four different types of

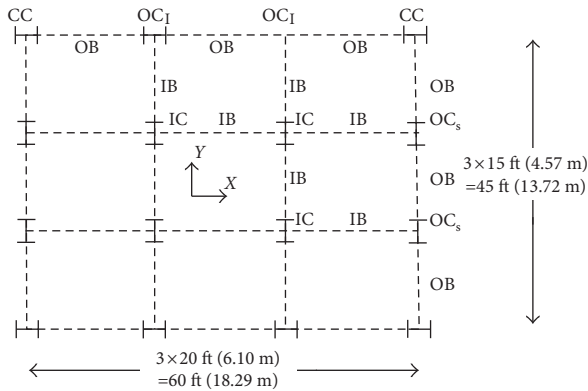


FIGURE 4: Typical plane view of a 10-storey steel frame.

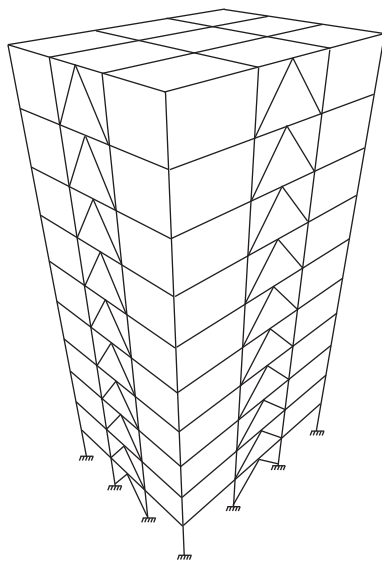


FIGURE 5: Three dimensional view of a V-braced frame.

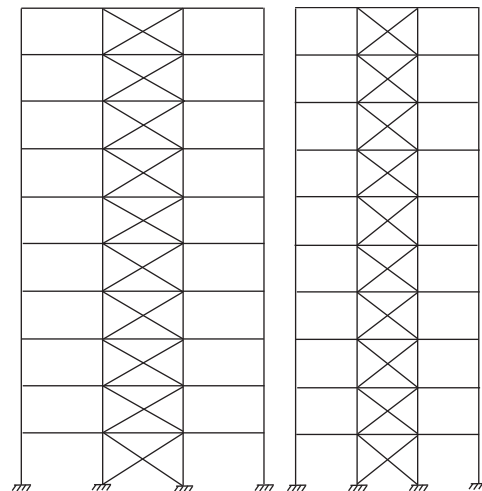
TABLE 1: Gravity loading on beams of roof and floors [36].

Beam type	Outer span beams (kN/m)	Inner span beams (kN/m)
Long span floor beams	9.79	19.59
Short span floor beams	8.04	16.07
Long span roof beams	6.75	13.50
Short span floor beams	5.54	11.07

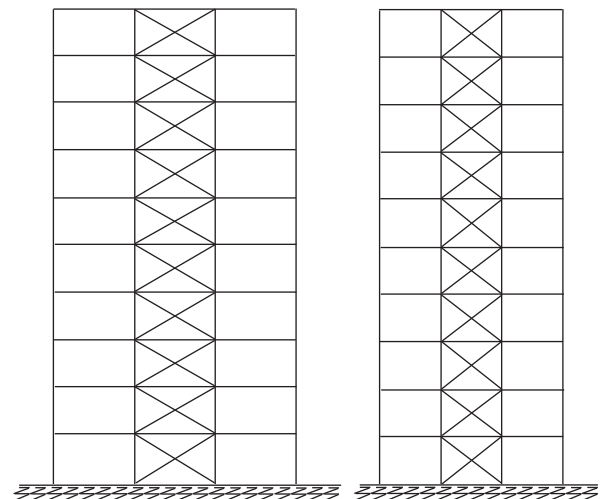
bracing such as X, V, Z, and eccentric V. The behavior of the frame is investigated with and without considering the effect of soil-structure interaction. The frame example is exposed to wind loads according to ASCE7-05 [31] in addition to dead, live, and snow loads. Optimum cross sections are practically selected from a predefined list of 128 W profiles taken from AISC. The stress constraints according to AISC-ASD [32], maximum lateral displacement constraint ($H/400$), interstorey drift constraint ($h/400$), and beam-to-column geometric constraints are subjected to the optimum design of the braced steel space frames. In the analyses, the steel modulus of elasticity, E , and yield stress, F_y , are taken as

TABLE 2: Wind loads calculated for the 10-storey braced frame [36].

Floor	X-direction		Y-direction	
	Distributed windward force (kN/m)	Distributed leeward force (kN/m)	Distributed windward force (kN/m)	Distributed leeward force (kN/m)
1	2.33	2.32	2.33	2.63
2	2.66	2.32	2.66	2.63
3	2.99	2.32	2.99	2.63
4	3.24	2.32	3.24	2.63
5	3.46	2.32	3.46	2.63
6	3.64	2.32	3.64	2.63
7	3.81	2.32	3.81	2.63
8	3.95	2.32	3.95	2.63
9	4.09	2.32	4.09	2.63
10	2.11	1.16	2.11	1.32



(a)



(b)

FIGURE 6: 2D view of the X-braced steel space frame without and with soil-structure interaction. (a) The case without soil-structure interaction. (b) The case with soil-structure interaction.

TABLE 3: Optimum results of the X-braced space frame.

Storeys	Member groups	Literature research, Hasancebi [36]	This study			
			TLBO without soil-structure interaction	TLBO with soil-structure interaction	HS without soil-structure interaction	HS with soil-structure interaction
1-2	CC	W16 × 36	W8 × 24	W8 × 28	W8 × 35	W8 × 31
	OC ₁	W12 × 65	W21 × 83	W14 × 99	W14 × 43	W12 × 50
	OC _s	W24 × 94	W44 × 224	W44 × 224	W12 × 50	W18 × 50
	IC	W12 × 120	W14 × 74	W16 × 89	W18 × 97	W18 × 119
	OB	W8 × 18	W8 × 24	W10 × 26	W8 × 24	W8 × 24
	IB	W18 × 35	W10 × 33	W14 × 48	W10 × 33	W16 × 40
	BR	W5 × 19	W8 × 15	W12 × 16	W8 × 21	W8 × 15
3-4	CC	W10 × 33	W8 × 28	W8 × 28	W14 × 48	W10 × 60
	OC ₁	W10 × 54	W12 × 87	W10 × 49	W10 × 33	W12 × 65
	OC _s	W12 × 72	W10 × 49	W12 × 53	W24 × 68	W24 × 76
	IC	W30 × 90	W24 × 62	W12 × 72	W14 × 68	W24 × 94
	OB	W8 × 18	W12 × 30	W8 × 24	W18 × 50	W18 × 50
	IB	W12 × 26	W14 × 34	W8 × 35	W10 × 33	W12 × 35
	BR	W6 × 15	W12 × 14	W12 × 14	W10 × 15	W6 × 15
5-6	CC	W16 × 31	W16 × 36	W8 × 31	W14 × 34	W14 × 43
	OC ₁	W10 × 49	W8 × 35	W14 × 34	W8 × 28	W12 × 45
	OC _s	W10 × 54	W8 × 40	W10 × 60	W14 × 38	W16 × 50
	IC	W12 × 58	W24 × 55	W14 × 53	W16 × 57	W18 × 65
	OB	W8 × 21	W16 × 36	W10 × 30	W10 × 30	W10 × 30
	IB	W12 × 26	W16 × 36	W14 × 38	W16 × 45	W18 × 50
	BR	W6 × 15	W10 × 15	W12 × 14	W12 × 22	W6 × 15
7-8	CC	W16 × 26	W8 × 24	W12 × 53	W10 × 45	W10 × 45
	OC ₁	W10 × 49	W8 × 31	W10 × 49	W12 × 45	W12 × 45
	OC _s	W10 × 49	W10 × 54	W12 × 53	W10 × 45	W14 × 48
	IC	W14 × 38	W16 × 36	W14 × 43	W14 × 48	W10 × 68
	OB	W8 × 21	W8 × 24	W10 × 30	W8 × 35	W12 × 35
	IB	W12 × 26	W14 × 34	W18 × 40	W10 × 33	W10 × 33
	BR	W6 × 9	W12 × 14	W12 × 14	W12 × 14	W12 × 14
9-10	CC	W12 × 26	W8 × 28	W8 × 24	W8 × 31	W12 × 40
	OC ₁	W8 × 31	W10 × 49	W14 × 30	W10 × 33	W14 × 53
	OC _s	W8 × 40	W8 × 31	W12 × 40	W14 × 30	W14 × 30
	IC	W8 × 28	W12 × 30	W12 × 40	W16 × 36	W12 × 45
	OB	W8 × 18	W8 × 24	W8 × 24	W21 × 44	W8 × 24
	IB	W12 × 30	W21 × 44	W10 × 33	W16 × 36	W10 × 39
	BR	W6 × 9	W10 × 15	W10 × 15	W12 × 14	W12 × 14
Weight (kN)		1092.91	1170.03	1217.91	1201.13	1265.50
Maximum lateral displacement (cm)		—	6.36	7.59	7.92	8.29
Interstorey drift (cm)		—	0.81	0.91	0.915	0.915
Maximum settlement (cm)		—	—	-0.657	—	-0.670

29000 ksi (203,893.6 MPa) and 36 ksi (253.1 MPa), respectively. Figure 4 shows the typical plane view of a 10-storey steel frame. Also, Figure 5 represents the three dimensional view of a V-braced frame. Each storey has a height of 3.66 m (12 ft). Modulus of elasticity for the concrete is taken as 32,000,000 kN/m², Poisson's ratio is 0.2, and weight per unit volume is 25 kN/m³.

All floors excluding the roof are exposed to a dead load of 2.88 kN/m² and a live load of 2.39 kN/m². The roof floor is exposed to a dead load of 2.88 kN/m² and a snow load of 0.75 kN/m². The total gravity loading on the beams of roof and floors is tabulated in Table 1 [36]. Wind loads are applied to the frame according to ASCE7-05 [31]. Wind loads calculated for the 10-storey braced frame are presented in Table 2 [36]. Modulus of elasticity of the soil, E_s , is taken to be equal to 80,000 kN/m². The depth of the soil stratum to

TABLE 4: Soil parameters for 10-storey X-braced steel space frame on elastic foundation.

Algorithm	γ	k (kN/m ³)	$2t$ (kN/m ³)
Teaching-learning-based optimization	4.52365	10882.438	70605.337
Harmony search algorithm	4.51999	10873.807	70661.621

the rigid base is taken as $H_s = 20$ m, and Poisson's ratio of the soil is equal to 0.25.

5.1. X-Braced Steel Space Frame. Figure 6 shows the typical 2D view of an X-braced steel space frame without and with soil-structure interaction. Optimum results of the X-braced space frame are given in Table 3. Soil parameters for the

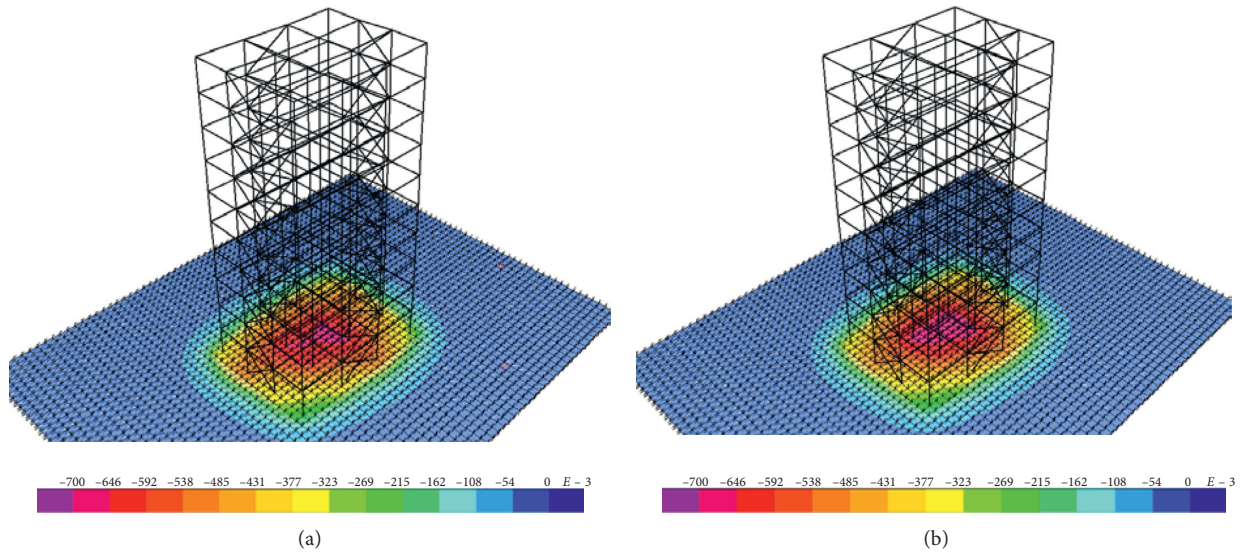


FIGURE 7: Settlements of soil surface for the X-braced steel space frame with two different algorithm methods (cm). (a) TLBO. (b) HS.

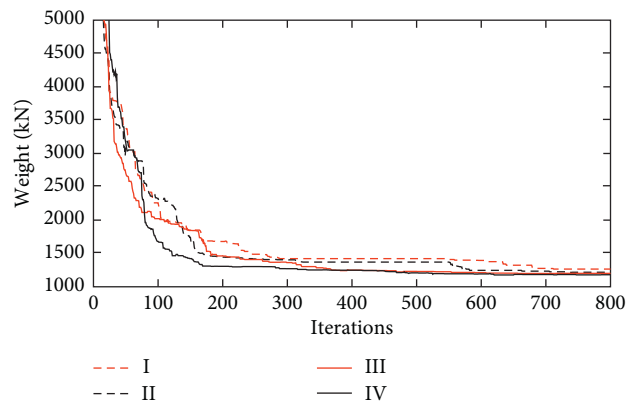


FIGURE 8: Design histories of the 10-storey X-braced steel space frame. I: HS with soil-structure interaction; II: TLBO with soil-structure interaction; III: HS without soil-structure interaction; IV: TLBO without soil-structure interaction.

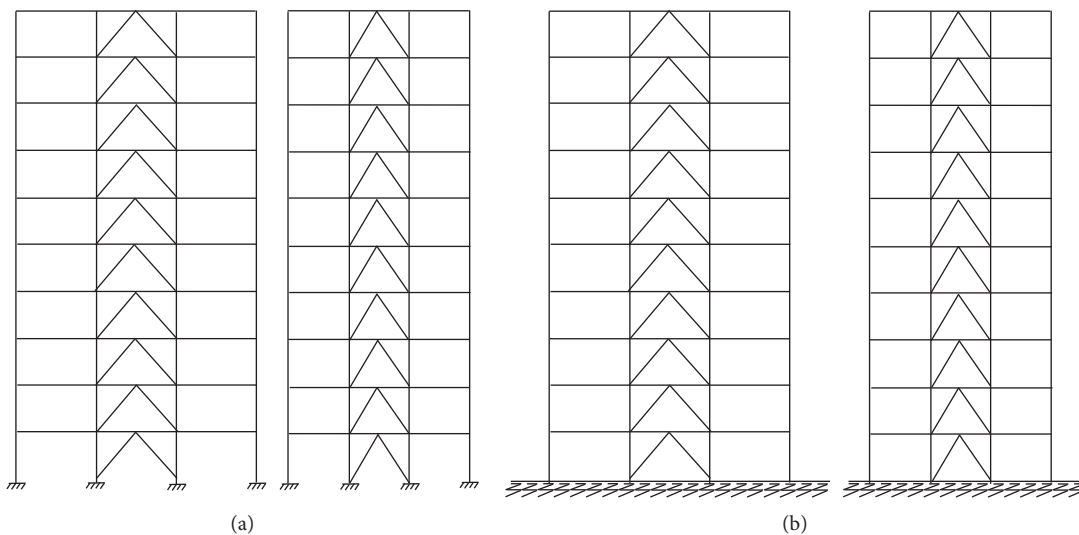


FIGURE 9: 2D view of the V-braced steel space frame without and with soil-structure interaction. (a) The case without soil-structure interaction. (b) The case with soil-structure interaction.

TABLE 5: Optimum results of the V-braced space frame.

Storeys	Member groups	Literature research, Hasancebi [36]	This study			
			TLBO without soil-structure interaction	TLBO with soil-structure interaction	HS without soil-structure interaction	HS with soil-structure interaction
1-2	CC		W8 × 28	W8 × 31	W8 × 28	W8 × 28
	OC ₁		W14 × 43	W16 × 67	W16 × 50	W12 × 50
	OC _s		W44 × 224	W27 × 161	W16 × 67	W18 × 106
	IC		W10 × 88	W18 × 106	W18 × 106	W14 × 132
	OB		W8 × 28	W14 × 34	W8 × 24	W8 × 24
	IB		W10 × 33	W10 × 33	W8 × 35	W10 × 33
	BR		W12 × 14	W6 × 15	W8 × 21	W12 × 14
3-4	CC		W8 × 24	W8 × 24	W8 × 31	W8 × 24
	OC ₁		W12 × 45	W10 × 49	W12 × 35	W21 × 44
	OC _s		W10 × 45	W18 × 86	W10 × 45	W16 × 40
	IC		W21 × 62	W21 × 68	W14 × 68	W18 × 65
	OB		W8 × 24	W10 × 30	W8 × 24	W8 × 24
	IB		W12 × 35	W8 × 35	W12 × 35	W16 × 40
	BR		W5 × 16	W8 × 21	W14 × 22	W10 × 26
5-6	CC		W12 × 30	W8 × 24	W10 × 39	W10 × 33
	OC ₁		W14 × 34	W8 × 31	W16 × 36	W16 × 36
	OC _s		W18 × 46	W14 × 48	W18 × 55	W18 × 50
	IC		W12 × 50	W18 × 55	W24 × 55	W21 × 62
	OB		W10 × 30	W8 × 24	W14 × 38	W14 × 38
	IB		W8 × 35	W16 × 36	W14 × 38	W18 × 50
	BR		W10 × 15	W12 × 19	W12 × 22	W6 × 15
7-8	CC		W8 × 28	W8 × 24	W14 × 53	W16 × 77
	OC ₁		W8 × 28	W8 × 35	W12 × 45	W8 × 35
	OC _s		W8 × 24	W12 × 30	W10 × 45	W8 × 35
	IC		W16 × 40	W16 × 45	W10 × 39	W12 × 40
	OB		W10 × 30	W8 × 24	W8 × 31	W8 × 35
	IB		W16 × 36	W14 × 34	W10 × 33	W18 × 40
	BR		W12 × 14	W12 × 16	W8 × 21	W12 × 22
9-10	CC		W12 × 30	W8 × 28	W14 × 48	W12 × 40
	OC ₁		W10 × 33	W8 × 24	W8 × 35	W8 × 40
	OC _s		W8 × 31	W8 × 24	W8 × 35	W8 × 35
	IC		W24 × 55	W12 × 26	W16 × 36	W16 × 36
	OB		W8 × 24	W8 × 24	W8 × 31	W8 × 31
	IB		W16 × 36	W18 × 40	W14 × 34	W16 × 36
	BR		W10 × 15	W10 × 15	W12 × 14	W12 × 14
Weight (kN)	1082.80	1083.80	1101.27	1118.04	1185.53	
Maximum lateral displacement (cm)	—	6.93	7.91	8.01	7.99	
Interstorey drift (cm)	—	0.91	0.91	0.915	0.91	
Maximum settlement (cm)	—	—	-0.650	—	-0.653	

TABLE 6: Soil parameters for the 10-storey V-braced steel space frame on elastic foundation.

Algorithm	γ	k (kN/m ³)	$2t$ (kN/m ³)
Teaching-learning-based optimization	4.70318	11306.947	67945.018
Harmony search algorithm	4.70957	11322.086	67853.886

space frame on elastic foundation are presented in Table 4. Moreover, Figures 7 and 8 display settlements of the soil surface for two different algorithm methods and design histories of optimum solutions, respectively.

5.2. V-Braced Steel Space Frame. Figure 9 shows the typical 2D view of a V-braced steel space frame without and with soil-structure interaction. Optimum results of the V-braced

space frame are shown in Table 5. Soil parameters for the space frame on elastic foundation are given in Table 6. Also, Figures 10 and 11 show the soil surface settlements obtained using two different algorithms and design histories of optimum solutions, respectively.

5.3. Z-Braced Steel Space Frame. Figure 12 represents the 2D side view of a Z-braced steel space frame without and with

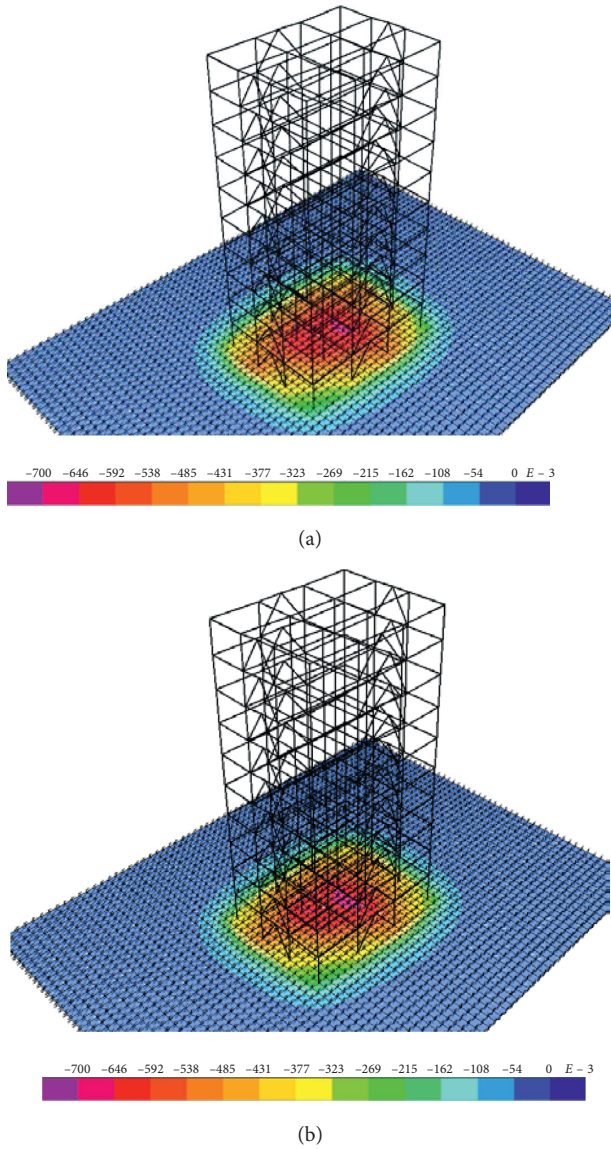


FIGURE 10: Settlements of soil surface for the V-braced steel space frame with two different algorithm methods (cm). (a) TLBO. (b) HS.

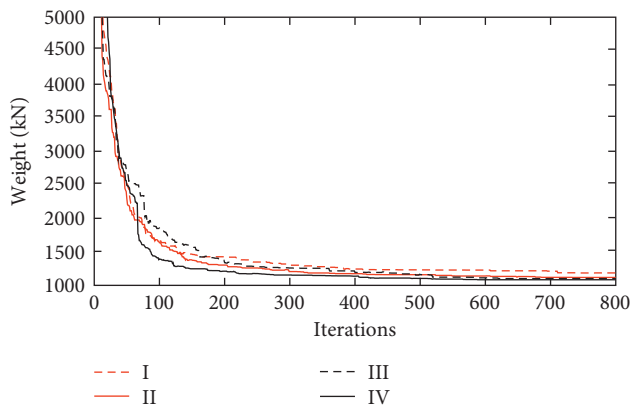


FIGURE 11: Design histories of the 10-storey V-braced steel space frame. I: HS with soil-structure interaction; II: HS without soil-structure interaction; III: TLBO with soil-structure interaction; IV: TLBO without soil-structure interaction.

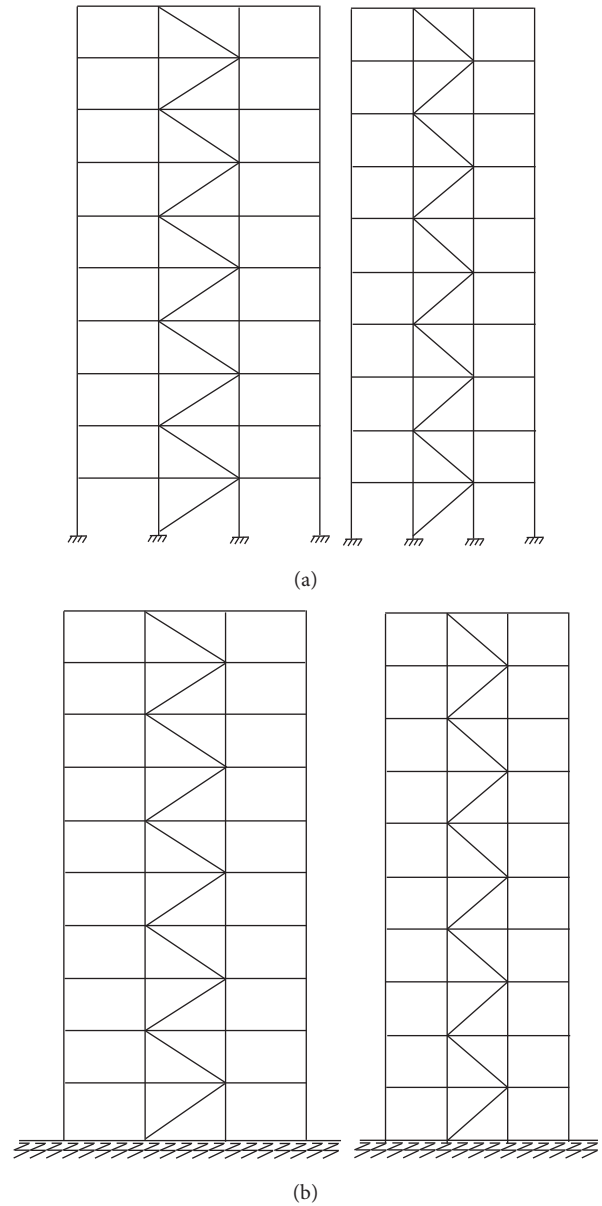


FIGURE 12: 2D view of the Z-braced steel space frame without and with soil-structure interaction. (a) The case without soil-structure interaction. (b) The case with soil-structure interaction.

soil-structure interaction. Optimum results of the Z-braced space frame are presented in Table 7. Soil parameters for the space frame on elastic foundation are given in Table 8. Moreover, Figures 13 and 14 represent settlements of the soil surface carried out with two different algorithm methods and design histories of optimum solutions, respectively.

5.4. *Eccentric V-Braced Steel Space Frame.* Figure 15 shows the 2D side view of an eccentric V-braced steel space frame without and with soil-structure interaction. The braces are connected to the beam from one-third of the beam length. Optimum results of the eccentric V-braced space frame are presented in Table 9. Soil parameters for the space frame on elastic foundation are presented in Table 10. Moreover,

TABLE 7: Optimum results of the Z-braced space frame.

Storeys	Member groups	Literature research, Hasancebi [36]	This study			
			TLBO without soil-structure interaction	TLBO with soil-structure interaction	HS without soil-structure interaction	HS with soil-structure interaction
1-2	CC		W8 × 31	W8 × 31	W8 × 35	W8 × 31
	OC ₁		W21 × 83	W16 × 67	W12 × 65	W10 × 68
	OC _s		W24 × 103	W30 × 108	W14 × 132	W30 × 108
	IC		W12 × 106	W14 × 99	W18 × 106	W14 × 109
	OB		W8 × 24	W8 × 24	W8 × 24	W8 × 28
	IB		W10 × 33	W12 × 35	W12 × 35	W14 × 43
	BR		W6 × 15	W8 × 24	W12 × 30	W8 × 15
3-4	CC		W10 × 54	W8 × 35	W16 × 36	W14 × 30
	OC ₁		W10 × 49	W14 × 90	W12 × 35	W12 × 65
	OC _s		W14 × 74	W30 × 108	W12 × 72	W18 × 55
	IC		W14 × 74	W21 × 68	W16 × 77	W21 × 73
	OB		W16 × 36	W8 × 24	W8 × 24	W8 × 24
	IB		W16 × 40	W12 × 35	W12 × 35	W14 × 38
	BR		W5 × 16	W12 × 16	W12 × 19	W8 × 24
5-6	CC		W8 × 24	W8 × 31	W8 × 35	W8 × 31
	OC ₁		W8 × 31	W10 × 49	W10 × 54	W8 × 35
	OC _s		W24 × 55	W16 × 45	W16 × 50	W21 × 68
	IC		W18 × 65	W24 × 55	W18 × 60	W24 × 62
	OB		W8 × 24	W16 × 36	W12 × 30	W16 × 36
	IB		W14 × 38	W14 × 34	W12 × 35	W14 × 34
	BR		W8 × 15	W12 × 22	W6 × 15	W8 × 28
7-8	CC		W8 × 24	W8 × 24	W8 × 31	W8 × 40
	OC ₁		W10 × 49	W8 × 31	W14 × 48	W12 × 35
	OC _s		W18 × 35	W14 × 43	W16 × 36	W14 × 48
	IC		W18 × 50	W16 × 40	W12 × 40	W27 × 84
	OB		W10 × 30	W8 × 24	W16 × 36	W12 × 35
	IB		W12 × 35	W14 × 34	W10 × 33	W10 × 33
	BR		W12 × 14	W10 × 15	W12 × 14	W10 × 15
9-10	CC		W8 × 31	W8 × 31	W14 × 34	W8 × 31
	OC ₁		W10 × 26	W8 × 35	W10 × 33	W14 × 30
	OC _s		W12 × 26	W8 × 40	W10 × 33	W10 × 33
	IC		W14 × 43	W14 × 34	W12 × 45	W12 × 45
	OB		W10 × 26	W24 × 55	W14 × 34	W14 × 30
	IB		W10 × 33	W14 × 34	W16 × 36	W16 × 36
	BR		W12 × 14	W12 × 14	W12 × 14	W12 × 14
Weight (kN)		1058.90	1095.27	1151.40	1124.00	1166.02
Maximum lateral displacement (cm)		—	7.98	7.84	7.21	8.19
Interstorey drift (cm)		—	0.91	0.915	0.915	0.915
Maximum settlement (cm)		—	—	-0.660	—	-0.669

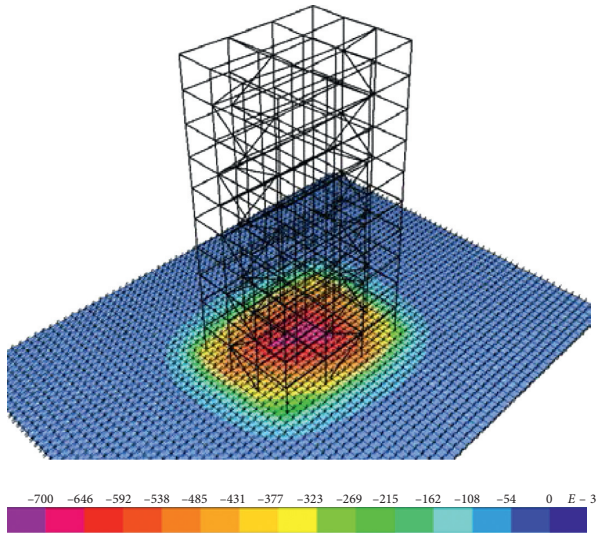
TABLE 8: Soil parameters for the 10-storey Z-braced steel space frame on elastic foundation.

Algorithm methods	γ	k (kN/m ³)	$2t$ (kN/m ³)
Teaching-learning-based optimization	4.52586	10887.654	70571.370
Harmony search algorithm	4.50073	10828.379	70959.363

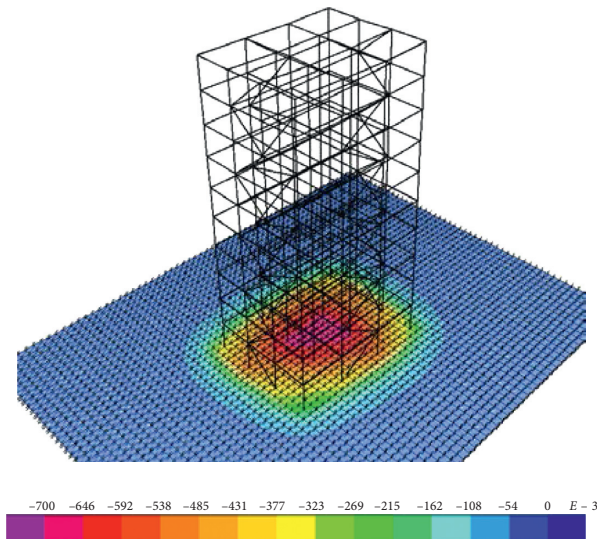
Figures 16 and 17 show settlements of the soil surface carried out with two different algorithm methods and design histories of optimum solutions, respectively.

It is observed from Tables 3, 5, and 7 that the minimum weights of the braced frames for the case without soil-structure interaction are very similar to the ones available in literature research [36]. In this study, the V-braced

type provides the lowest steel weight of 1083.80 kN by using teaching-learning-based optimization. Z-braced and X-braced types provide the second and third low weights, 1095.27 kN and 1170.03, respectively. Moreover, the minimum weight of the eccentric V-braced frame, 1275.01 kN, is nearly 15%, 14.1%, and 8.2% heavier than the minimum steel weights of the V-, Z-, and X-braced frames, respectively. On the other hand, harmony search algorithm presents 2.6–4.7% heavier minimum steel weights than the ones obtained from teaching-learning-based optimization for the case without soil-structure interaction. The tables including optimum results also show that the value of interstorey drift is very close to the limit value ($h/400$). Therefore, the displacement constraints play very crucial roles in the optimum design of the braced frames. Five



(a)



(b)

FIGURE 13: Settlements of soil surface for the Z-braced steel space frame with two different algorithm methods (cm). (a) TLBO. (b) HS.

independent runs are performed for each braced type for the case without soil-structure interaction.

In the case with soil-structure interaction, the minimum weights of all braced frames increased depending on settlements on the soil surfaces. It is observed from Tables 4, 6, 8, and 10 that the soil parameters of 10-storey braced steel frames on elastic foundation are similar for all cases. The minimum steel weights are mostly obtained by teaching-learning-based optimization. For the X-braced frame, the minimum weight obtained by TLBO for the case with soil-structure interaction is 4.01% heavier than the weight of the frame excluding soil-structure interaction. This ratio is 5.32% for the harmony search algorithm. Moreover, settlement values on the soil surfaces are nearly -0.66 cm as seen in Figure 7. For the V-braced frame including soil-structure interaction, TLBO and HS present 1.66 and 5.9% heavier weights, respectively. The settlements in this braced

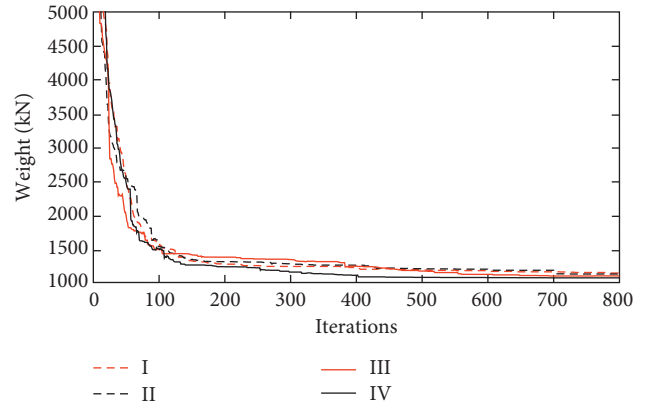
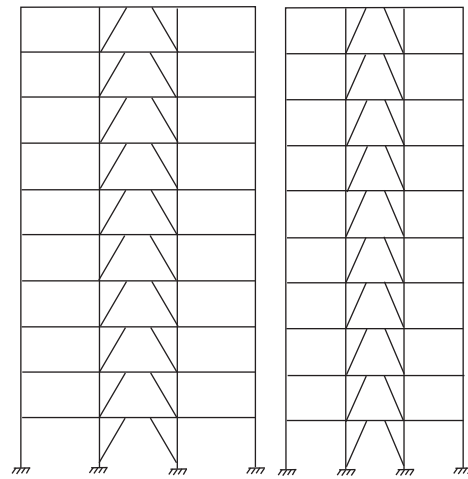
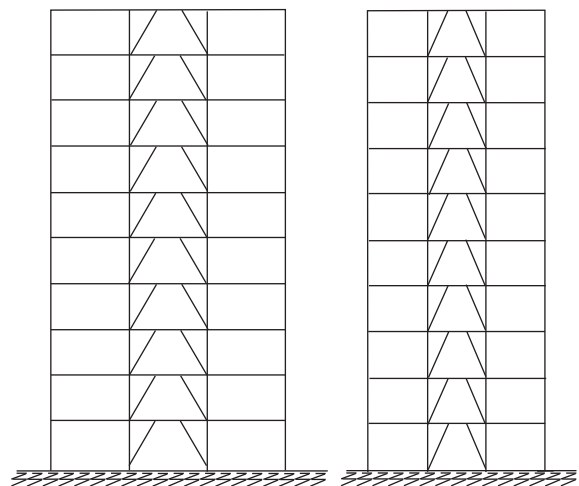


FIGURE 14: Design histories of the 10-storey Z-braced steel space frame. I: HS with soil-structure interaction; II: TLBO with soil-structure interaction; III: HS without soil-structure interaction; IV: TLBO without soil-structure interaction.



(a)



(b)

FIGURE 15: 2D view of the eccentric V-braced steel space frame without and with soil-structure interaction. (a) The case without soil-structure interaction. (b) The case with soil-structure interaction.

TABLE 9: Optimum results of the eccentric V-braced space frame.

Storeys	Member groups	This study			
		TLBO without soil-structure interaction	TLBO with soil-structure interaction	HS without soil-structure interaction	HS with soil-structure interaction
1-2	CC	W24 × 68	W14 × 14	W14 × 14	W10 × 10
	OC ₁	W24 × 24	W12 × 12	W14 × 14	W12 × 12
	OC _s	W36 × 36	W14 × 14	W10 × 10	W40 × 40
	IC	W14 × 14	W10 × 10	W18 × 18	W12 × 12
	OB	W10 × 10	W18 × 18	W18 × 18	W16 × 16
	IB	W18 × 18	W16 × 16	W8 × 8	W16 × 16
	BR	W10 × 10	W16 × 16	W10 × 10	W8 × 8
3-4	CC	W10 × 10	W12 × 12	W18 × 18	W14 × 14
	OC ₁	W12 × 12	W12 × 12	W14 × 14	W12 × 12
	OC _s	W10 × 10	W12 × 12	W12 × 12	W21 × 21
	IC	W27 × 27	W14 × 14	W14 × 14	W14 × 14
	OB	W18 × 18	W16 × 16	W16 × 16	W16 × 16
	IB	W12 × 12	W24 × 24	W10 × 10	W16 × 16
	BR	W12 × 12	W10 × 10	W10 × 10	W12 × 12
5-6	CC	W12 × 12	W12 × 12	W16 × 16	W10 × 10
	OC ₁	W12 × 12	W10 × 10	W12 × 12	W8 × 8
	OC _s	W24 × 24	W12 × 12	W12 × 12	W12 × 12
	IC	W14 × 14	W16 × 16	W24 × 24	W24 × 24
	OB	W18 × 18	W12 × 12	W14 × 14	W16 × 16
	IB	W14 × 14	W24 × 24	W16 × 16	W14 × 14
	BR	W10 × 10	W6 × 6	W12 × 12	W6 × 6
7-8	CC	W10 × 10	W12 × 12	W8 × 8	W14 × 14
	OC ₁	W16 × 16	W8 × 8	W12 × 12	W12 × 12
	OC _s	W10 × 10	W8 × 8	W16 × 16	W14 × 14
	IC	W10 × 10	W18 × 18	W10 × 10	W10 × 10
	OB	W12 × 12	W8 × 8	W16 × 16	W8 × 8
	IB	W14 × 14	W14 × 14	W10 × 10	W10 × 10
	BR	W12 × 12	W12 × 12	W12 × 12	W12 × 12
9-10	CC	W12 × 12	W8 × 8	W14 × 14	W14 × 14
	OC ₁	W8 × 8	W10 × 10	W10 × 10	W8 × 8
	OC _s	W8 × 8	W12 × 12	W10 × 10	W10 × 10
	IC	W14 × 14	W10 × 10	W14 × 14	W12 × 12
	OB	W8 × 8	W8 × 8	W10 × 10	W14 × 14
Weight (kN)	IB	W12 × 12	W10 × 10	W14 × 14	W10 × 10
	BR	W10 × 10	W12 × 12	W12 × 12	W6 × 6
	Weight (kN)	1275.01	1355.05	1335.23	1441.58
Maximum lateral displacement (cm)	7.76	8.09	7.51	7.66	
Interstorey drift (cm)	0.91	0.915	0.91	0.915	
Maximum settlement (cm)	—	-0.609	—	-0.609	

TABLE 10: Soil parameters for the 10-storey eccentric V-braced steel space frame on elastic foundation.

Algorithm	γ	k (kN/m ³)	$2t$ (kN/m ³)
Teaching-learning-based optimization	5.04545	12120.214	63375.683
Harmony search algorithm	5.01478	12047.186	63760.516

frame are nearly -0.65 cm as given in Figure 10. For the Z-braced frame with soil-structure interaction, the minimum weights obtained are 5.11% and 3.73% heavier by using TLBO and HS, respectively. The settlements in this braced frame are similar to the ones of the other braced frames. For the eccentric V-braced frame with soil-structure interaction, the minimum steel weights obtained are 6.27 and 7.94% heavier by using TLBO and HS, respectively. Moreover,

the convergences of optimum solutions with iteration steps are seen in Figures 8, 11, 13, and 17 in detail.

6. Summary and Conclusions

In this study, the optimum design of a 10-storey steel space frame braced with X, V, Z, and eccentric V-shaped bracings including soil-structure interaction is investigated. Optimum solutions are obtained using two different meta-heuristic algorithm methods: teaching-learning-based optimization (TLBO) and harmony search (HS). For this purpose, a code is developed in MATLAB computer program incorporated with SAP2000-OAPI (open application programming interface). Required cross sections are automatically selected from a list of 128 W profiles taken from AISC (American Institute of Steel Construction). The

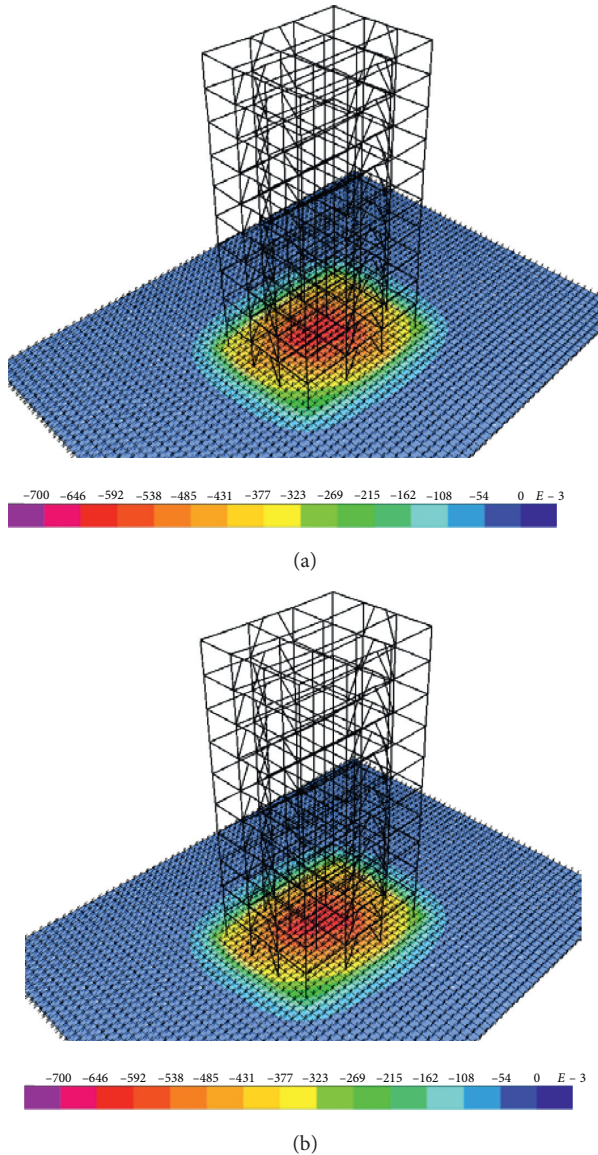


FIGURE 16: Settlements of soil surface for the eccentric V-braced steel space frame with two different algorithm methods (cm). (a) TLBO. (b) HS.

frame model is exposed to wind loads according to ASCE7-05 in addition to dead, live, and snow loads. The stress constraints in accordance with AISC-ASD (American Institute of Steel Construction-Allowable Stress Design), maximum lateral displacement constraints, interstorey drift constraints, and beam-to-column connection constraints are applied in analyses. A three-parameter Vlasov elastic foundation model is used to consider the soil-structure interaction effect. The summary of the results obtained in this study are briefly listed below:

- (i) It is observed from analyses that the minimum weight of the space frame varies by the types of bracing. The lowest steel weight, 1083.80 kN, is obtained for the V-braced steel frame by using TLBO. Z-braced and X-braced types provide the

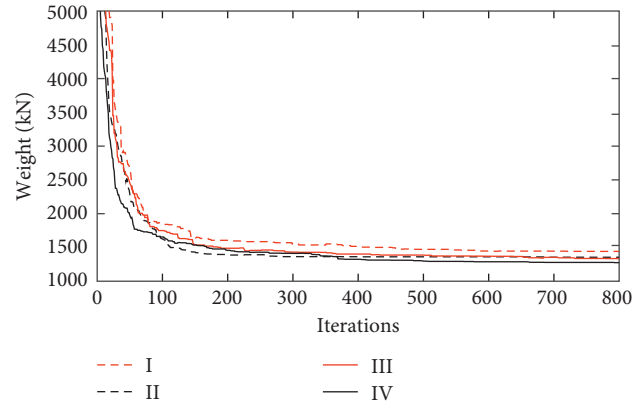


FIGURE 17: Design histories of the 10-storey eccentric V-braced steel space frame. I: HS with soil-structure interaction; II: TLBO with soil-structure interaction; III: HS without soil-structure interaction; IV: TLBO without soil-structure interaction.

second and third low weights, 1095.27 kN and 1170.03, respectively. These results are similar to the ones available in literature [36]. The heaviest among them is the minimum weight of the eccentric V-braced frame, 1275.01 kN.

- (ii) Harmony search algorithm presents 2.6–4.7% heavier steel weights than the ones obtained from teaching-learning-based optimization for the frames without soil-structure interaction. Although the lighter analysis results are obtained in TLBO, a representative structure model in TLBO is analyzed twice in an iteration step by SAP2000 programming. On the other hand, it is enough to analyze the system once in HS. This situation requires longer time for the analysis in TLBO.
- (iii) Interstorey drift values are very close to its limit value of 0.915 cm ($h/400$). Therefore, the constraints are important determinants of the optimum design of the braced frames.
- (iv) Consideration of soil-structure interaction results in heavier steel weight. For the X-braced frame including soil-structure interaction, the minimum weights are obtained to be 4.01 and 5.32% heavier by using TLBO and HS, respectively. For the V-braced frame, these values are calculated to be 1.66 and 5.9% heavier, respectively. For the Z-braced frame, these values are obtained to be 5.11% and 3.73% heavier, respectively. Moreover, for the eccentric V-braced frame, the minimum weights are obtained to be 6.27 and 7.94% heavier by these algorithm methods.
- (v) Settlement values on the soil surfaces are nearly 0.61–0.67 cm for all braced frames.
- (vi) Finally, the techniques used in optimizations seem to be quite suitable for practical applications. An adaptive setting for the parameters will be very useful and user-friendly especially for the structures with a large number of members as in the case here. This will be considered in future studies.

Conflicts of Interest

The authors declare that they have no conflicts of interest.

References

- [1] A. Daloglu and M. Armutcu, "Optimum design of plane steel frames using genetic algorithm," *Teknik Dergi*, vol. 9, pp. 483–487, 1998.
- [2] E. S. Kameshki and M. P. Saka, "Optimum design of nonlinear steel frames with semi-rigid connections using a genetic algorithm," *Computers & Structures*, vol. 79, no. 17, pp. 1593–1604, 2001.
- [3] K. S. Lee and Z. W. Geem, "A new structural optimization method based on the harmony search algorithm," *Computers & Structures*, vol. 82, no. 9-10, pp. 781–798, 2004.
- [4] M. S. Hayalioglu and S. O. Degertekin, "Minimum cost design of steel frames with semi-rigid connections and column bases via genetic optimization," *Computers & Structures*, vol. 83, no. 21-22, pp. 1849–1863, 2005.
- [5] O. Kelesoglu and M. Ülker, "Multi-objective fuzzy optimization of space trusses by Ms-Excel," *Advances in Engineering Software*, vol. 36, no. 8, pp. 549–553, 2005.
- [6] S. O. Degertekin, "A comparison of simulated annealing and genetic algorithm for optimum design of nonlinear steel space frames," *Structural and Multidisciplinary Optimization*, vol. 34, no. 4, pp. 347–359, 2007.
- [7] Y. Esen and M. Ülker, "Optimization of multi storey space steel frames, materially and geometrically properties non-linear," *Journal of the Faculty of Engineering and Architecture of Gazi University*, vol. 23, pp. 485–494, 2008.
- [8] M. P. Saka, "Optimum design of steel sway frames to BS5950 using harmony search algorithm," *Journal of Constructional Steel Research*, vol. 65, no. 1, pp. 36–43, 2009.
- [9] S. O. Degertekin and M. S. Hayalioglu, "Harmony search algorithm for minimum cost design of steel frames with semi-rigid connections and column bases," *Structural and Multidisciplinary Optimization*, vol. 42, no. 5, pp. 755–768, 2010.
- [10] O. Hasancebi, S. Carbas, E. Dogan, F. Erdal, and M. P. Saka, "Comparison of non-deterministic search techniques in the optimum design of real size steel frames," *Computers & Structures*, vol. 88, no. 17-18, pp. 1033–1048, 2010.
- [11] O. Hasancebi, S. Çarbaş, and M. P. Saka, "Improving the performance of simulated annealing in structural optimization," *Structural and Multidisciplinary Optimization*, vol. 41, no. 2, pp. 189–203, 2010.
- [12] O. Hasancebi, T. Bahcecioglu, O. Kurc, and M. P. Saka, "Optimum design of high-rise steel buildings using an evolution strategy integrated parallel algorithm," *Computers & Structures*, vol. 89, no. 21-22, pp. 2037–2051, 2011.
- [13] V. Togan, "Design of planar steel frames using teaching-learning based optimization," *Engineering Structures*, vol. 34, pp. 225–232, 2012.
- [14] I. Aydogdu and M. P. Saka, "Ant colony optimization of irregular steel frames including elemental warping effect," *Advances in Engineering Software*, vol. 44, no. 1, pp. 150–169, 2012.
- [15] T. Dede and Y. Ayvaz, "Structural optimization with teaching-learning-based optimization algorithm," *Structural Engineering and Mechanics*, vol. 47, no. 4, pp. 495–511, 2013.
- [16] T. Dede, "Optimum design of grillage structures to LRFD-AISC with teaching-learning based optimization," *Structural and Multidisciplinary Optimization*, vol. 48, no. 5, pp. 955–964, 2013.
- [17] O. Hasancebi, T. Teke, and O. Pekcan, "A bat-inspired algorithm for structural optimization," *Computers & Structures*, vol. 128, pp. 77–90, 2013.
- [18] M. P. Saka and Z. W. Geem, "Mathematical and metaheuristic applications in design optimization of steel frame structures: an extensive review," *Mathematical Problems in Engineering*, vol. 2013, Article ID 271031, 33 pages, 2013.
- [19] O. Hasancebi and S. Çarbaş, "Bat inspired algorithm for discrete size optimization of steel frames," *Advances in Engineering Software*, vol. 67, pp. 173–185, 2014.
- [20] T. Dede, "Application of teaching-learning-based-optimization algorithm for the discrete optimization of truss structures," *KSCE Journal of Civil Engineering*, vol. 18, no. 6, pp. 1759–1767, 2014.
- [21] S. K. Azad and O. Hasancebi, "Discrete sizing optimization of steel trusses under multiple displacement constraints and load case using guided stochastic search technique," *Structural and Multidisciplinary Optimization*, vol. 52, no. 2, pp. 383–404, 2015.
- [22] M. Artar and A. T. Daloglu, "Optimum design of composite steel frames with semi-rigid connections and column bases via genetic algorithm," *Steel and Composite Structures*, vol. 19, no. 4, pp. 1035–1053, 2015.
- [23] M. Artar, "Optimum design of steel space frames under earthquake effect using harmony search," *Structural Engineering and Mechanics*, vol. 58, no. 3, pp. 597–612, 2016.
- [24] M. Artar, "Optimum design of braced steel frames via teaching learning based optimization," *Steel and Composite Structures*, vol. 22, no. 4, pp. 733–744, 2016.
- [25] S. Carbas, "Design optimization of steel frames using an enhanced firefly algorithm," *Engineering Optimization*, vol. 48, no. 12, pp. 2007–2025, 2016.
- [26] A. T. Daloglu, M. Artar, K. Ozgan, and A. I. Karakas, "Optimum design of steel space frames including soil-structure interaction," *Structural and Multidisciplinary Optimization*, vol. 54, no. 1, pp. 117–131, 2016.
- [27] M. P. Saka, O. Hasancebi, and Z. W. Geem, "Metaheuristics in structural optimization and discussions on harmony search algorithm," *Swarm and Evolutionary Computation*, vol. 28, pp. 88–97, 2016.
- [28] I. Aydogdu, "Cost optimization of reinforced concrete cantilever retaining walls under seismic loading using a biogeography-based optimization algorithm with Levy flights," *Engineering Optimization*, vol. 49, no. 3, pp. 381–400, 2017.
- [29] MATLAB, *The Language of Technical Computing*, The Mathworks Inc., Natick, MA, USA, 2009.
- [30] SAP2000, *Integrated Finite Elements Analysis and Design of Structures*, Computers and Structures Inc., Berkeley, CA, USA, 2008.
- [31] ASCE7-05, *Minimum Design Loads for Building and Other Structures*, American Society of Civil Engineering, Reston, VA, USA, 2005.
- [32] AISC-ASD, *Manual of Steel Construction, Allowable Stress Design*, American Institute of Steel Construction, Chicago, IL, USA, 1989.
- [33] P. Dumonteil, "Simple equations for effective length factors," *Engineering Journal. AISC*, vol. 29, pp. 111–115, 1992.
- [34] C. V. G. Vallabhan and A. T. Daloglu, "Consistent FEM-Vlasov model for plates on layered soil," *Journal of Structural Engineering*, vol. 125, no. 1, pp. 108–113, 1999.

- [35] R. V. Rao, V. J. Savsani, and D. P. Vakharia, "Teaching-learning-based optimization: a novel method for constrained mechanical design optimization problems," *Computer-Aided Design*, vol. 43, no. 3, pp. 303–315, 2011.
- [36] O. Hasancebi, "Cost efficiency analyses of steel frameworks for economical design of multi-storey buildings," *Journal of Constructional Steel Research*, vol. 128, pp. 380–396, 2017.

Research Article

Development of Future Rule Curves for Multipurpose Reservoir Operation Using Conditional Genetic and Tabu Search Algorithms

Anongrit Kangrang ¹, Haris Prasanchum,² and Rattana Hormwichian¹

¹Faculty of Engineering, Maharakham University, Kantharawichai, Maharakham 44150, Thailand

²Faculty of Engineering, Rajamangala University of Technology Isan, Khon Kaen Campus, Muang, Khon Kaen 40000, Thailand

Correspondence should be addressed to Anongrit Kangrang; anongrit.k@msu.ac.th

Received 28 July 2017; Revised 21 October 2017; Accepted 6 November 2017; Published 11 February 2018

Academic Editor: Ravipudi V. Rao

Copyright © 2018 Anongrit Kangrang et al. This is an open access article distributed under the Creative Commons Attribution License, which permits unrestricted use, distribution, and reproduction in any medium, provided the original work is properly cited.

Optimal rule curves are necessary guidelines in the reservoir operation that have been used to assess performance of any reservoir to satisfy water supply, irrigation, industrial, hydropower, and environmental conservation requirements. This study applied the conditional genetic algorithm (CGA) and the conditional tabu search algorithm (CTSA) technique to connect with the reservoir simulation model in order to search optimal reservoir rule curves. The Ubolrat Reservoir located in the northeast region of Thailand was an illustrative application including historic monthly inflow, future inflow generated by the SWAT hydrological model using 50-year future climate data from the PRECIS regional climate model in case of B2 emission scenario by IPCC SRES, water demand, hydrologic data, and physical reservoir data. The future and synthetic inflow data of reservoirs were used to simulate reservoir system for evaluating water situation. The situations of water shortage and excess water were shown in terms of frequency magnitude and duration. The results have shown that the optimal rule curves from CGA and CTSA connected with the simulation model can mitigate drought and flood situations than the existing rule curves. The optimal future rule curves were more suitable for future situations than the other rule curves.

1. Introduction

Nowadays, water resource issues have become more complex, which is related to global climate change and land-use change due to population and economic growth, which are increasing rapidly. For water resource management, both demand management site and supply management site are often required to solve the problems. Improving the reservoir operation for increased efficiency is another way of supply management site, which does not require the physical development of reservoir. Normally, reservoir operation uses upper and lower rule curves to consider the release of water from the reservoir responding to downstream demands in long-term operation. The purpose of the rule curves for reservoir operation was divided into two main areas: (i) variation of hydrological conditions [1], such as precipitation and inflow that flows into the reservoir were affected by climate change, and (ii) water allocation for

social, economic, and engineering purposes in downstream areas has changed due to the population growth and land-use demand. The reservoir management agency (such as the Royal Irrigation Department of Thailand) needs to plan in advance the appropriate volume of water in the reservoir (at each time interval) for storage and release of water for various purposes [2], including the implementation of the plan as long as the relevant factors in the future have not changed from the original. However, if future conditions are different from those anticipated in the planning phase, performance may differ from planned to minimize water shortage or overflow. The rule curve assumptions are based on maintaining the water level (or volume of water) in the reservoir to appropriate the changing hydrological situation [3] and downstream water allocation (according to the time period, which is generally one year). The main purpose is to avoid the risk of water shortages and floods in the reservoir and downstream areas. During the dry season, reservoirs

need to maintain water volume to reduce the risk of water levels lower than minimum storage. During the rainy season, the reservoir must release water to reduce the storage volume, which can support the precipitation and inflow that flows into the reservoir. This also includes prevention of overflow situation in the reservoir [4]. The reservoir rule curves have been improved to provide the optimal solution for long-term operation. Typically, reservoir operating system has been large and complex, especially in watershed areas having both drought and flood situations [5].

To search optimal rule curves of the reservoir is a non-linear optimization problem. There are many optimization techniques that are applied to connect with the reservoir simulation model for searching optimal rule curves such as dynamic programming (DP), genetic algorithm (GA), and simulated annealing algorithm (SA) [6–10]. Those obtained rule curves are effectively applied for each area. However, these new optimization techniques have not been applied to find the optimal rule curves like the tabu search technique.

In the last decades, there are many alternative algorithms to solve complex computational problems. Tabu search is a heuristic procedure designed for solving optimization problems. It has been successfully applied to many engineering fields such as industrial engineering, electrical engineering, civil engineering, and water resources engineering [11, 12]. Tabu search is a very aggressive heuristic for overcoming local optima and searching for global optimality by exploring other regions of the solution space. Its efficiency depends on the fine-tuning of some parameters [13–15].

This study proposed a conditional tabu search algorithm (CTSA) to connect with the simulation model for searching the optimal reservoir rule curves. A minimum average water shortage was used as the objective function for the searching procedure. The proposed model has been applied to determine the optimal rule curves of the Ubolrat Reservoir in the northeast region of Thailand with the historic monthly inflow, future inflow under scenario B2, water demand, hydrologic data, and physical reservoir data. Comparison of the conditional genetic algorithm (CGA) and the CTSA was shown to demonstrate the effectiveness of the proposed CTSA model.

2. Methodology

2.1. Future Inflow into the Ubolrat Reservoir. The development of the optimal future rule curves will use data from the future inflow flowing into the Ubolrat Reservoir considering the effects of climate change using the PRECIS model. Thus, the future inflow will be produced using the SWAT hydrological model. For the future climate data in the study area, PRECIS is a regional climate model, based on the development of ECHAM4 model, displaying the data as “grid” with high solution of $22 \times 22 \text{ km}^2$ [16]. The data recorded during 1997–2014 were used as a baseline to predict those for 2015 to 2064. These data present the precipitation and maximum and minimum temperatures.

Because of the Ubolrat Reservoir and the study area located in northeastern Thailand, most of the economic characteristics are generated by the sale of major agricultural products, such as rice and sugarcane, which require water for

TABLE 1: Spatial data and observed inflow data for SWAT performance evaluation.

Data types	Period	Scale	Source
Spatial data (model input)			
DEM	2011	$30 \times 30 \text{ m}$	
River map	2011	1 : 50,000	Land Development
Soil types	2011	1 : 50,000	Department, Thailand
Land use map	2014	$30 \times 30 \text{ m}$	
Climate	1997–2014	Daily	Thai Meteorological Department, Thailand
Observed inflow (model performance assessment)			
Ubolrat Dam	1997–2014	Daily	Electricity Generating Authority of Thailand

cultivation during the rainy season as the primary source. The expansion of most urban areas in the region is slow. Therefore, this study has chosen the appropriate greenhouse gas emission projection model based on the model of socioeconomic development, population growth, and technology of the study area according to the IPCC SRES, with emphasis on regional development for the emission scenario B2—prediction of lower population growth than A2, moderate-level economic development, and oriented toward environmental protection [17].

SWAT (Soil and Water Assessment Tool) [18] is a semidistributed hydrological model developed for the measurement of the inflow, sediment, and water quality under the climate and land-use changes [19]. SWAT can be used to continually measure the daily inflow and define a longer period of time in the future. It can also connect and import the spatial data from the Geographic Information System (GIS) in order to evaluate the inflow. The spatial data and SWAT performance evaluation are presented in Table 1.

The accuracy of the SWAT results can be evaluated by comparing the simulated data with that recorded data from the observation station (i.e., Ubolrat Reservoir). Three variables including R^2 (coefficient of determination), RE (relative error), and E_{ns} (Nash-Sutcliffe simulation efficiency) were considered as the key indicator of the accuracy. In general, SWAT needs to modify the value of hydrological parameters for the model calibration and validation [20]. In this study, 8 parameter values were used including Alpha_BF, Gwqmn, Gw_Revap, Sol_Awc, Epc0, Esco, Ch_N2, and Gw_delay. Then, the SWAT with adjusted sensitivity parameters was optimized (calculated results are close to the observed data); it was considered to be suitable for calculating the future inflow. Later, the daily future climate data from PRECIS that had been downscaled were classified into 50 years in future periods; the processes of model setup are shown in Figure 1.

2.2. Reservoir Operation Model. Reservoir system comprises available water that flows from upstream into the reservoir and multipurpose downstream demand. The reservoir operation is performed using water usage criteria release, operating policies, and reservoir rule curves with monthly

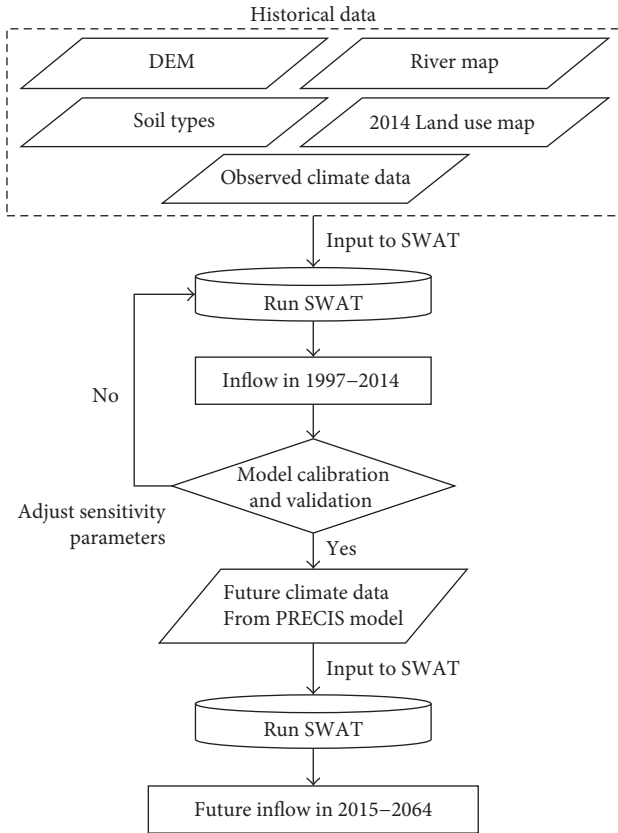


FIGURE 1: Model setup processes for future inflow.

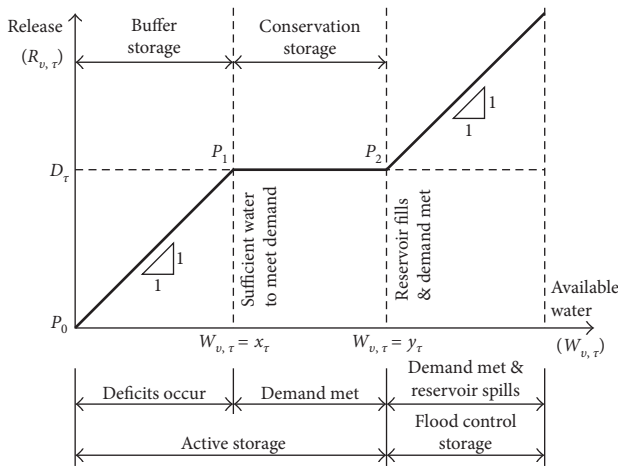


FIGURE 2: Standard operating rule.

data for long-term period. A reservoir operation model was constructed on the concept of water balance, and it can be used to simulate reservoir operation effectively. The reservoir operating policies are based on the monthly rule curves of individual reservoirs and the principles of water balance equation under the reservoir simulation model. The existing standard operating policies used for the reservoir rule curves operation are presented in Figure 2. The y -axis is defining the total water released, and the x -axis is defining the available water. The available water is represented as the total of inflow

and starting point of storage in the reservoir during the period. In case of where demand is constant, water is not conserved for future demand, and if the available water is less than water demand, all of water in the reservoir is released and the reservoir is emptied [21]. At the point P_1 , the available water is equal to the water demand, and at the point P_2 , the available water is the total of reservoir capacity and water demand. If the available storage is between P_1 and P_2 , water release is equal to water demand. The line between P_0 and P_1 makes the ratio of 1 : 1 (45°) [22]. On the other hand, if the available water exceeds the sum of active storage and water demand, the reservoir will release the excess spilled [23]. In addition, the standard operating policies can also be calculated from

$$R_{v,\tau} = \begin{cases} D_\tau + W_{v,\tau} - y_\tau & \text{for } W_{v,\tau} \geq y_\tau + D_\tau \\ D_\tau & \text{for } x_\tau \leq W_{v,\tau} < y_\tau + D_\tau \\ D_\tau + W_{v,\tau} - x_\tau & \text{for } x_\tau - D_\tau \leq W_{v,\tau} < x_\tau \\ 0 & \text{otherwise,} \end{cases} \quad (1)$$

where $R_{v,\tau}$ is the released water from the reservoir during year v and period τ ($\tau=1$ to 12, representing January to December), D_τ is the water demand of month τ ; x_τ is the lower rule curve of month τ ; y_τ is the upper rule curve of month τ , and $W_{v,\tau}$ is the available water calculating by a simple water balance, as described in

$$W_{v,\tau} = S_{v,\tau} + Q_{v,\tau} - R_{v,\tau} - E_\tau - DS, \quad (2)$$

where $S_{v,\tau}$ is the stored water at the end of month τ ; $Q_{v,\tau}$ is the monthly inflow to reservoir, E_τ is the average value of evaporation loss, and DS is the minimum reservoir storage capacity (the capacity of dead storage).

In (2) and Figure 2, if available water is in the range of the upper and lower rule levels, then demands are satisfied in full. If available water is over the top of the upper rule level, then the water is spilled from the reservoir in downstream river in order to maintain water level at the upper rule level. If available water is under the bottom of the lower rules level, a reduction of water release is performed. The operating policy usually reserves the available water ($W_{v,\tau}$) for reducing the risk of water shortage in the future, when $0 \leq W_{v,\tau} < x_\tau - D_\tau$ under long-term operation.

The released water from the reservoir was used to calculate the water shortage and excess water release situations, which can be expressed as the frequency of failures in a year and the number of excess water release, as well as the average annual shortage (as the objective function for searching the optimal rule curves in this study). The results were recorded and used to develop the CTSA model.

2.3. Application of CGA with the Reservoir Simulation Model for Searching Rule Curves.

The connection of the CGA to the reservoir simulation model was as follows. The CGA requires an encoding format to change the decision variables into the form of chromosomes. The CGA, which consists of selection, crossover, and mutation, is executed. After this stage, the genetic operations will create new chromosomes. For this study, each decision variable represents the average

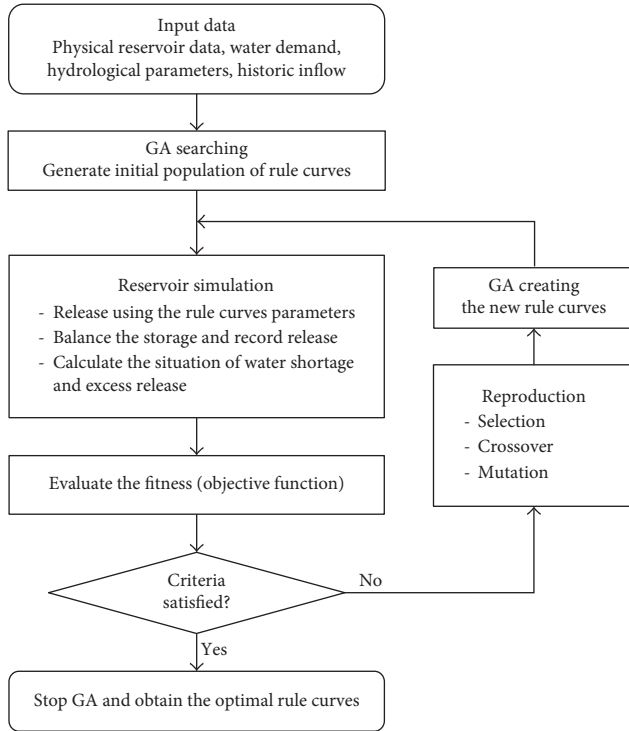


FIGURE 3: Applying CGA and reservoir simulation for searching rule curves.

monthly water storage of the rule curves in the reservoirs, which are defined as the upper bound and the lower bound. After the first set of chromosomes in the initial population have been calculated (24 decision variables, which consist of 12 values from the upper bound and 12 values from lower bound situations), the released water will be recalculated by the reservoir simulation model using these rule curves. Next, the released water is used to determine the objective function with the aim of assessing the fitness of the GA. After that, the reproduction process will create new rule curve values in the next generation. This procedure is repeated until the 24 values of rule curves are appropriate. The CGA and reservoir simulation model for searching the rule curves are described in Figure 3.

In this study, the objective function for searching the optimal reservoir rule curves is the minimum of the average water shortage ($\min_{(avr)}$) in million cubic meters (MCM) per year, as shown in

$$\min_{(avr)} = \frac{1}{n} \sum_{v=1}^n Sh_v, \quad (3)$$

where n is the total number of considered years and Sh_v is the water deficit during year v (a year that does not meet 100% of the target demand).

2.4. Applying Conditional Tabu Search Algorithm for Searching Rule Curves. The developed CTSA for searching rule curves is described as follows. The CTSA begins with an initial population $\{X_1, X_2, \dots, X_n\}$ created randomly within the feasible space. With the 24 decision variables (rule curve

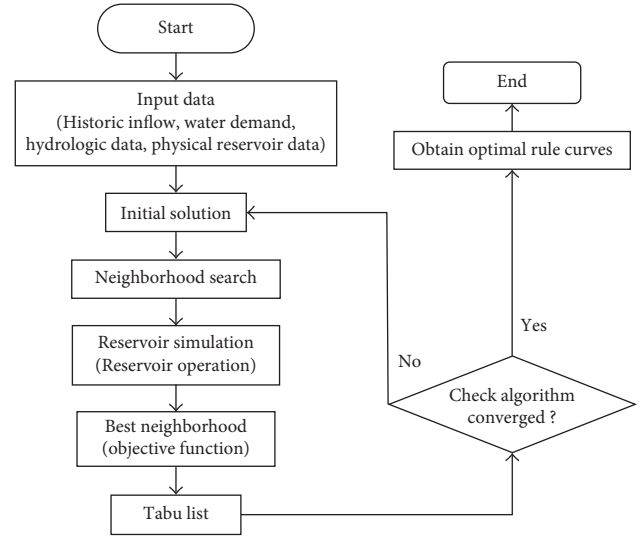


FIGURE 4: Applying tabu and reservoir simulation for searching rule curves.

variables for both upper and lower), the feasible solution of the iteration i th is represented as $X_i = [x_{i1}, x_{i2}, \dots, x_{i24}]^T$. Then, a set of rule curves is used in reservoir simulation, and the released water is calculated by the simulation model using these rule curves. Next, the released water is used to calculate the fitness function to evaluate the feasible solution. The fitness function is the minimum of the average water shortage (Z) subject to constraints on the simulation model as described in (3).

Then, the process is continued until the termination criterion is satisfied as described in Figure 4. This termination criterion is optimum; it can be expressed by a slight change in the fitness values (less than 0.10 MCM).

2.5. Illustrative Application. The Ubolrat Basin is a branch of the Chi Basin located in northeastern Thailand (Figure 5). It has an area of about 3,282 km². The average annual rainfall is 1,411 mm, and the mean annual temperature is 27°C. The Phong River lies in the middle of the basin. The Ubolrat Dam was developed by building an earth core rock fill dam across the Phong River with a height of 33 m and crest length of 7,800 m. The normal storage capacity and average annual inflow are 2,263 MCM and 2,478.591 MCM, respectively. The objectives of the Ubolrat Dam are irrigation, flood control, and industrial and domestic water supply. Schematic diagram of Ubolrat basin is described in Figure 6.

The study used CTSA in connection with a reservoir operation model to find optimal rule curves through the MATLAB toolbox. The optimal rule curve can then be applied to an actual scenario depending on whether the rule curve can be used to cover every case or event that might occur. Thus, the HEC-4 model was used to create the synthetic inflow data into the monthly inflows as a synthetic data set of 500 events. This method was based on the actual historic monthly inflow of the Ubolrat Reservoir between

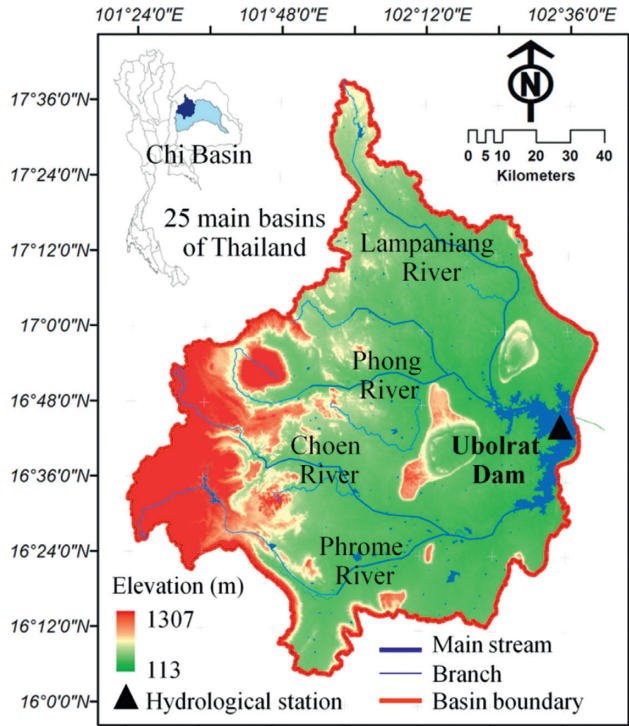


FIGURE 5: Location of the Ubolrat Dam.

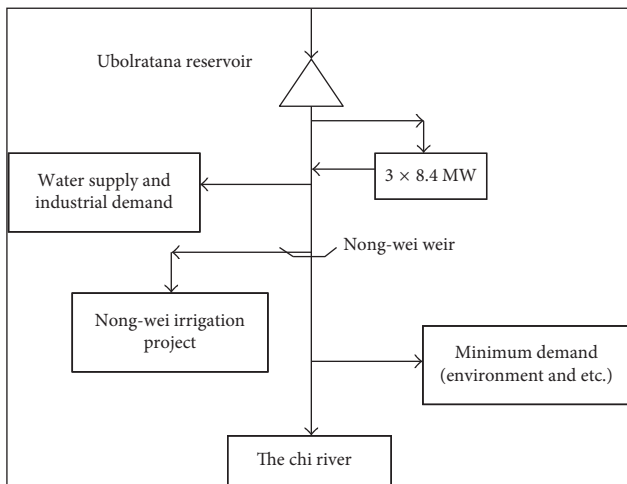


FIGURE 6: Schematic diagram of the Ubolrat basin.

years 1963 and 2014 (50 years) imported to the HEC-4 model to generate the synthetic inflow event. (1 event is a representative period of 50 years.) Therefore, the monthly inflow data are 300,000 values (50 years \times 12 months \times 500 events). Then, input synthetic inflow data were used to assess the efficiency of the new rule curves and compare them with the existing rule curves and also between the CTSA and CGA model under the same conditions. Further, the new obtained rule curves from CTSA and CGA model were used to evaluate with the future situation of B2 scenario [24]. The future inflows to reservoir were created by SWAT model that considered climate changes [25–28].

TABLE 2: SWAT sensitivity parameters.

No.	Parameter	Range	Adjusted Values
1	ALPHA_BF	0-1	0.025
2	GWQMN	0-500	0
3	GW_REVAP	0-500	1.25
4	SOL_AWC	0-1	0.28
5	EPCO	0-1	0
6	ESCO	0-1	0.52
7	CH_N2	—	0.035
8	GW_DELAY	0-500	31

TABLE 3: SWAT performance evaluation index.

Range	Average annual inflow (MCM)		Assessment index		
	Observed	Simulation	R^2	RE	E_{ns}
Calibration	2,858.8	2,413.1	0.89	15.6	0.80
Validation	1,421.4	1,380.1	0.91	2.3	0.89

3. Results and Discussion

3.1. Future Inflow into the Ubolrat Reservoir. An evaluation on SWAT accuracy used the data found during 1997–2014 (18 years; 1997–2008 for calibration and 2009–2014 for validation) for Ubolrat Reservoir station. Practically, 8 parameter values were selected and used to analyze the flexibility score as the modified parameter values of the flexibility by adjusting the inflow volume to closely match with the data from the observed station as presented in Table 2.

The inflow calculated by SWAT and compared with the data from the two observed station shows the inflow during the period of model calibration and validation; meanwhile, R^2 , RE, and E_{ns} were satisfactory and accurate as the deviation can be accepted as presented in Table 3; the goodness of fit of the data was depicted in Figure 7.

The inflow at the Ubolrat Reservoir station simulated by SWAT was divided into 2 phases: (1) baseline inflow which is the climate and spatial data recorded during 1997–2014 and (2) future inflow using the climate data from PRECIS model resulted during 2015–2064. The inflow analysis indicates that an average volume of the baseline inflow was 2,736 MCM and an average volume of the future inflow was 4,580.5 MCM. When comparing those two volumes, it was noted that the future inflow seems to be increased (1,844.5 MCM or 40.3% in 50 future years). Figure 8 illustrates the annual inflow simulated by SWAT during 2015–2064, and Figure 9 depicts the comparative result between the average baseline inflow and the average 10-year future inflow with increased trend in the future period, most of which have shown more than 4,000 MCM, except the third period. This result shows that the future inflow flows into the Ubolrat Reservoir with increased volume.

3.2. Optimal Historic Rule Curves. The historic data of inflow, evaporation, water requirement, and monthly rainfall

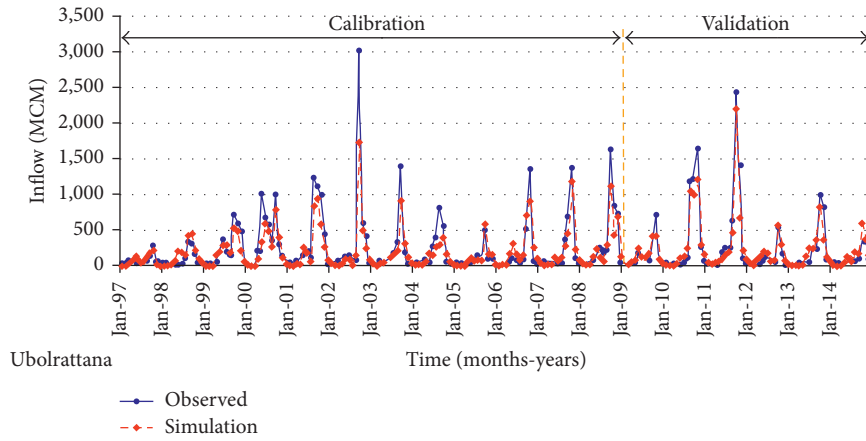


FIGURE 7: The comparison between the runoff from the observed stations and the SWAT result.

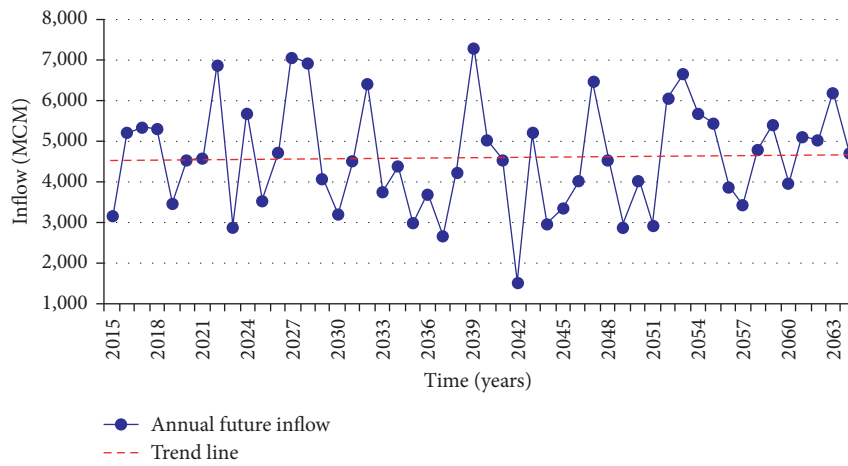


FIGURE 8: Annual future inflow flowing into Ubolrat Reservoir during 2015–2064.

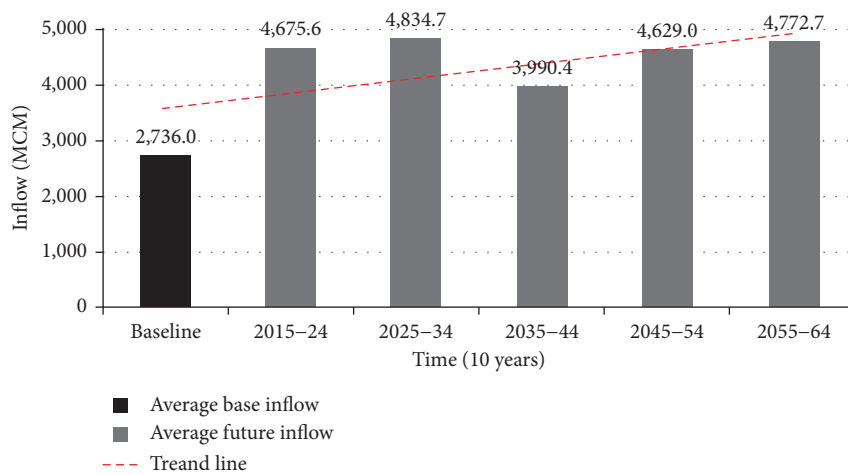


FIGURE 9: Average 10-year future inflow flowing into Ubolrat Reservoir compared with the baseline.

were imported for processing in the CGA connected to the simulation model and CTSA model, and the optimal rule curves were obtained. These obtained rule curves are plotted in order to compare them with the existing rule curves as

shown in Figure 10. They indicated the optimal upper and lower rule curves for the CTSA (RC4) compared with the existing rule curves (RC1) and the rule curves obtained using CGA (RC2). The results show that the patterns from the

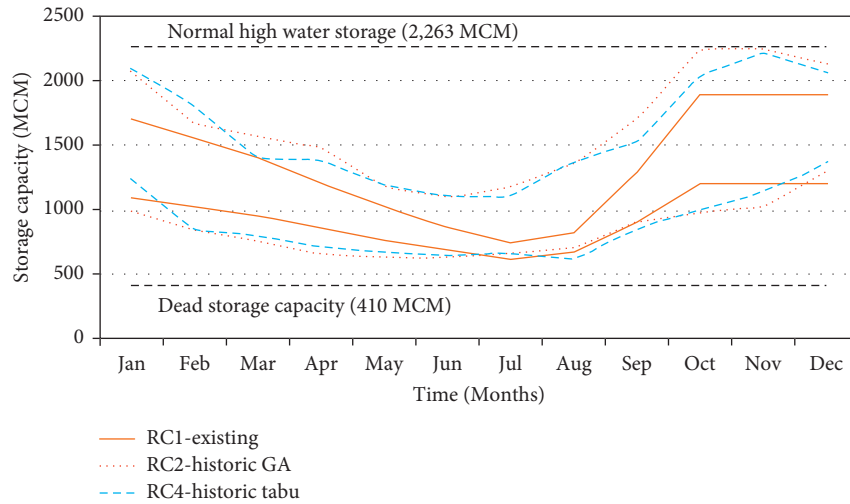


FIGURE 10: Optimal historic rule curves of the Ubolrat Reservoir.

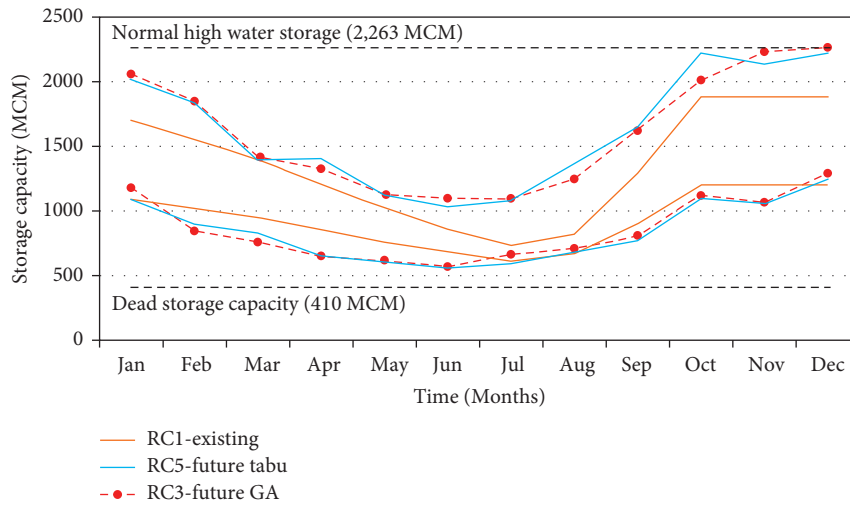


FIGURE 11: Optimal future rule curves of the Ubolrat Reservoir.

existing rule curves and the new rule curves obtained from the CTSA and CGA are similar.

The obtained rule curves also indicated that the water storage levels of the CTSA and CGA lower rule curves are lower than the existing rule curves during the dry season (February–June) in order to release more water to reduce water scarcity. In the middle of rainy season (August–October), the CTSA and CGA upper curves are higher than their existing rule curves in order to increase water storage for next dry season. This will help alleviate water shortages in the next year. These patterns of the obtained curves are similar to the pattern of the other reservoirs in Thailand on the other studies [7, 10] because of seasonal effect.

3.3. Optimal Future Rule Curves. To find the future rule curves, the average monthly inflow for the future period 2015–2064 under the B2 scenario [27] was imported into the

CGA and CTSA model, and then, the optimal future rule curves were obtained. Figure 7 shows the optimal upper and lower rule curves of the CGA (RC3) and CTSA (RC5) compared with the existing rule curves (RC1). The results show that the patterns from the existing rule curves and the new future rule curves obtained from the CGA and CTSA are similar. The storage capacity of the upper rule curves of the CGA (RC3) and CTSA (RC5) were higher than the existing upper rule curves to reduce the spill water and to keep the storage capacity full at the end of the rainy season. This will help prevent water shortages in the following year. Whereas, during the dry season (February to June), the storage capacities of the RC3 and RC5 were lower than the existing rule curves in order to release more water for alleviating the problem of water shortages. These rule curve patterns are similar to those from previous studies on reservoir rule curves in Thailand, which were affected by the seasons [7, 10].

TABLE 4: Situations of water shortage and excess release of the systems using historic inflow.

Situations	Rule curves	Frequency (times/year)	Magnitude (MCM/year)		Duration (year)	
			Average	Maximum	Average	Maximum
Water shortage	RC1 (existing)	0.857	554.918	1,594	6.000	22.000
	RC2 (CGA)	0.878	402.633	1,352	8.600	25.000
	RC4 (CTSA)	0.959	455.776	1,324	15.667	34.000
Excess release	RC1 (existing)	0.612	578.319	3,323.422	3.000	7.000
	RC2 (CGA)	0.408	423.555	2,891.616	2.857	5.000
	RC4 (CTSA)	0.469	478.789	3,000.471	2.556	6.000

TABLE 5: Situations of water shortage of the systems using synthetic inflow from historic data.

Rule curves		Frequency (times/year)	Magnitude (MCM/year)		Duration (year)	
			Average	Maximum	Average	Maximum
RC1 (existing)	μ	0.889	532.169	1,482.370	9.573	19.780
	σ	0.037	25.134	144.076	3.414	6.538
RC2 (CGA)	μ	0.883	381.586	1,465.750	9.248	20.190
	σ	0.039	29.268	180.698	3.424	7.595
RC3 (CGA)	μ	0.918	427.853	1,431.100	12.542	24.320
	σ	0.032	27.612	188.318	5.252	8.507
RC4 (CTSA)	μ	0.728	391.612	1,453.790	4.776	11.000
	σ	0.051	28.749	177.480	1.348	4.306
RC5 (CTSA)	μ	0.911	404.437	1,442.930	11.918	23.690
	σ	0.034	28.146	179.992	5.266	8.304

Note: μ = average, σ = standard deviation.

TABLE 6: Situations of excess water release of the systems using synthetic inflow from historic data.

Rule curves		Frequency (times/year)	Magnitude (MCM/year)		Duration (year)	
			Average	Maximum	Average	Maximum
RC1 (existing)	μ	0.648	550.036	3,511.112	2.817	7.140
	σ	0.045	33.939	825.296	0.534	1.939
RC2 (CGA)	μ	0.472	390.421	3,247.282	2.304	5.590
	σ	0.051	39.386	808.863	0.461	1.843
RC3 (CGA)	μ	0.495	438.704	3,310.449	2.163	5.330
	σ	0.050	36.914	785.299	0.410	1.596
RC4 (CTSA)	μ	0.482	400.120	3,197.957	2.296	5.380
	σ	0.050	38.579	814.755	0.475	1.600
RC5 (CTSA)	μ	0.504	412.739	3,225.344	2.457	5.850
	σ	0.051	37.803	801.793	0.525	1.866

Note: μ = average, σ = standard deviation.

TABLE 7: Situations of water shortage and excess release of the systems using future inflow.

Situations	Rule curves	Frequency (times/year)	Magnitude (MCM/year)		Duration (year)	
			Average	Maximum	Average	Maximum
Water shortage	RC1 (existing)	0.140	23.200	660.000	1.167	2.000
	RC2 (CGA)	0.240	9.340	412.000	1.200	2.000
	RC4 (CTSA)	0.340	32.860	418.000	1.417	4.000
	RC3 (CGA)	0.020	5.800	290.000	1.000	1.000
	RC5 (CTSA)	0.340	32.860	418.000	1.417	4.000
Excess release	RC1 (existing)	0.980	2,085.463	4,711.864	24.500	27.000
	RC2 (CGA)	0.980	2,056.182	4,697.881	24.500	27.000
	RC4 (CTSA)	0.980	2,085.965	4,702.331	24.500	27.000
	RC3 (CGA)	0.980	2,045.096	4,689.417	24.500	27.000
	RC5 (CTSA)	0.980	2,085.965	4,702.331	24.500	27.000

3.4. Performance of Optimal Rule Curves. The evaluation of the new historic rule curves and future rule curves generated from the CGA and CTSA model aimed to determine the performance of the rule curves with the synthetic historic inflow of 500 samples and the future inflows (B2 scenario), as shown in Tables 4–7. Table 4 shows the situations of water shortage and excess release of the systems when considering historic inflow. It indicated that the magnitudes of water shortage and excess release of the systems using CGA and CTSA rule curves are less than the magnitudes of using existing rule curves (402.633 and 455.776 million cubic meters (MCM)/year for average water shortage of CGA and CTSA, resp.). Whereas the frequency and duration time of water shortage and excess release of the systems using CGA and CTSA rule curves are higher than the frequency and duration of using existing rule curves.

Tables 5 and 6 show the efficiency of the five rule curves for water shortage and excess release situations by considering the synthetic historic inflow of 500 samples. It indicates that the situations of water shortage and excess release when using the historic rule curves (RC2 and RC3) are less than using the existing rule curves (RC1) and the future rule curves (RC4 and RC5).

In the case of future situation (Table 7), the future rule curves (RC4 and RC5) showed the best performance, as indicated by the frequency of the water shortage and the average and the maximum magnitudes of the water shortages. The future rule curves are more suitable for future situations than the existing rule curves and the historic rule curve. It can be concluded that rule curves created using the specific inflow periods will be the most suitable. The proposed CTSA model is another search optimal technique, so the results are near optimality that closed to the results of the other search techniques based on the same condition. However, the efficiency of each technique was carried out on many studies [7, 10].

4. Conclusion

This study proposed an alternative algorithm for searching optimal reservoir rule curves. The conditional tabu search algorithm (CTSA) and reservoir simulation model were applied to search the optimal rule curves of the Ubolrat Reservoir under historic monthly inflow and future inflow under the scenario B2. The future inflow and synthetic inflow data of reservoirs were used to simulate reservoir system for evaluating situations of water shortage and excess release. The results found that the new obtained rule curves from CTSA are more suitable for reservoir operating than the existing rule curves. The frequency and magnitude of water shortage and excess water release for using new obtained rule curves are lower than the existing rule curves. When comparing the new obtained rule curves from CTSA with the rule curves of the CGA method as well as the existing simulation method, it was found that these rule curves are similar. The proposed CTSA model is an effective method for application to find optimal reservoir rule curves. This reveals that the CTSA and GA model with future inflow are effective methods for searching optimal reservoir rule curves that are suitable for using in the future situations.

Conflicts of Interest

The authors declare that there are no conflicts of interest regarding the publication of this paper.

Acknowledgments

This research was financially supported by Mahasarakham University and National Research Council of Thailand Grant Year 2018.

References

- [1] X. Li, S. Gao, P. Liu, and G. Chen, "Dynamic control of flood limited water level for reservoir operation by considering inflow uncertainty," *Journal of Hydrology*, vol. 391, no. 1-2, pp. 124–132, 2010.
- [2] P. Liu, L. Li, G. Chen, and D. E. Rheinheimer, "Parameter uncertainty analysis of reservoir operating rules based on implicit stochastic optimization," *Journal of Hydrology*, vol. 514, pp. 102–113, 2014.
- [3] T. Zhao, X. Cai, and D. Yang, "Effect of streamflow forecast uncertainty on real-time reservoir operation," *Advances in Water Resources*, vol. 34, no. 4, pp. 495–504, 2011.
- [4] E. Fallah-Mehdipour, O. B. Haddad, and M. A. Mariño, "Real-time operation of reservoir system by genetic programming," *Water Resources Management*, vol. 26, no. 14, pp. 4091–4103, 2012.
- [5] S. K. Jain, M. K. Goel, and P. K. Agarwal, "Reservoir operation study of Sabarmati system, India," *Journal of Water Resources Planning and Management*, vol. 124, no. 1, pp. 31–38, 1998.
- [6] Electricity Generating Authority of Thailand (EGAT), "Manual for operating the Bhumibol and Sirikit Reservoirs," EGAT Research Report, Bangkok, Thailand, 2004.
- [7] C. Chaleeraktragoon and A. Kangrang, "Dynamic programming with the principle of progressive optimality for searching rule curves," *Canadian Journal of Civil Engineering*, vol. 34, no. 2, pp. 170–176, 2007.
- [8] F. J. Chang, L. Chen, and L. C. Chang, "Optimizing the reservoir operating rule curves by genetic algorithms," *Hydrological Processes*, vol. 19, no. 11, pp. 2277–2289, 2005.
- [9] C. H. Yeh, "Applying multi-objective genetic algorithms for planning of flood detention dams system," *Taiwan Water Conservancy*, vol. 45, no. 2, pp. 70–81, 1997.
- [10] A. Kangrang, S. Compliew, and R. Hormwichian, "Optimal reservoir rule curves using simulated annealing," *Proceedings of the Institution of Civil Engineers–Water Management*, vol. 164, no. 1, pp. 27–34, 2011.
- [11] T. Zhang, "A hybrid particle swarm optimization and tabu search algorithm for order planning problems of steel factories based on the make-to-stock and make-to-order management architecture," *Journal of Industrial and Management Optimization*, vol. 7, no. 1, pp. 31–51, 2011.
- [12] M. D. C. Cunha and L. Ribeiro, "Tabu search algorithms for water network optimization," *European Journal of Operational Research*, vol. 157, no. 3, pp. 746–758, 2004.
- [13] F. Glover and M. Laguna, *Tabu Search*, Kluwer Academic Publishers, Dordrecht, Netherlands, 1997.
- [14] U. Faigle and W. Kern, "Some convergence results for probabilistic tabu search," *ORSA Journal on Computing*, vol. 4, no. 1, pp. 32–37, 1992.
- [15] W. Sa-ngiamvibool, S. Pothiya, and I. Ngamroo, "Multiple tabu search algorithm for economic dispatch problem

- considering valve-point effects,” *Electrical Power and Energy Systems*, vol. 33, no. 4, pp. 846–854, 2011.
- [16] G. Lacombe, C. T. Hoanh, and V. Smakhtin, “Multi-year variability or unidirectional trends? mapping long-term precipitation and temperature changes in continental Southeast Asia using PRECIS regional climate model,” *Climatic Change*, vol. 113, no. 2, pp. 285–299, 2012.
- [17] Southeast Asia START Regional Center, “Preparation of climate change scenarios for climate change impact assessment in Thailand,” Final Report, Bangkok, Thailand, 2010.
- [18] A. G. Arnold, R. Srinivasan, R. S. Muttiah, and J. R. Williams, “Large area hydrologic modeling and assessment part I: model development,” *Journal of American Water Resource Association*, vol. 34, no. 1, pp. 73–89, 1998.
- [19] M. T. Vu, V. S. Raghavan, and S. Y. Liong, “Ensemble climate projection for hydro-meteorological drought over the river basin in central highland, Vietnam,” *KSCE Journal of Civil Engineering*, vol. 19, no. 2, pp. 427–433, 2015.
- [20] M. Meaurio, A. Zabaleta, J. Yriarte, R. Srinivasan, and I. Antigüedad, “Evaluation of SWAT models performance to simulate streamflow spatial origin. The case of a small forested watershed,” *Journal of Hydrology*, vol. 525, pp. 326–334, 2015.
- [21] A. Rittama, “Hedging policy for reservoir system operation: a case study of Mun Bon and Lam Chae Reservoirs,” *Kasetsart Journal*, vol. 43, pp. 833–842, 2009.
- [22] T. R. Neelakanta and K. Sasireka, “Hydropower reservoir operation using standard operating and standard hedging policies,” *International Journal of Engineering and Technology*, vol. 5, no. 2, pp. 1191–1196, 2013.
- [23] A. Tayebiyani, T. A. M. Ali, A. H. Ghazali, and M. A. Malek, “Optimization of exclusive release policies for hydropower reservoir operation by using genetic algorithm,” *Water Resources Management*, vol. 30, no. 3, pp. 1203–1216, 2016.
- [24] IPCC, *Summary of Policymakers: Emission Scenarios: A Special Report of IPCC Workgroup III of the Intergovernmental Panel on Climate Change*, IPCC, Geneva, Switzerland, 2000.
- [25] W. Buakhao and A. Kangrang, “DEM resolution impact on the estimation of the physical characteristics of watersheds by using SWAT,” *Advances in Civil Engineering*, vol. 2016, Article ID 8180158, 9 pages, 2016.
- [26] A. W. Alansi, M. S. M. Amin, G. Abdul Halim, H. Z. M. Shafri, and W. Aimrun, “Validation of SWAT model for stream flow simulation and forecasting in Upper Bernam humid tropical river basin, Malaysia,” *Hydrology and Earth System Sciences Discussions*, vol. 6, no. 6, pp. 7581–7609, 2009.
- [27] A. Kangrang, H. Prasanchum, and R. Hormwichian, “Future runoff under land use and climate changes in the Ubolratana Basin, Thailand,” *International Journal of Ecology & Development*, vol. 32, no. 3, pp. 53–66, 2017.
- [28] C. Chiamsathit, A. J. Adeloje, and B. S. Soundharajan, “Assessing competing policies at Ubonratana reservoir, Thailand,” *Proceeding of the Institution of Civil Engineering–Water Management*, vol. 167, no. 10, pp. 551–560, 2015.

Research Article

The Optimization of Calcareous Fly Ash-Added Cement Containing Grinding Aids and Strength-Improving Additives

Gökhan Kaplan ¹, Sadık Alper Yildizel ², Selçuk Memiş ³ and Ali Uğur Öztürk⁴

¹Kastamonu Vocational School, Kastamonu University, Kastamonu, Turkey

²Engineering Faculty, Civil Engineering Department, Karamanoglu MehmetBey University, Karaman, Turkey

³Engineering Faculty, Civil Engineering Department, Kastamonu University, Kastamonu, Turkey

⁴Engineering Faculty, Civil Engineering Department, Manisa Celal Bayar University, Manisa, Turkey

Correspondence should be addressed to Gökhan Kaplan; gkaplan@kastamonu.edu.tr

Received 29 July 2017; Revised 30 October 2017; Accepted 9 November 2017; Published 28 January 2018

Academic Editor: Arnaud Perrot

Copyright © 2018 Gökhan Kaplan et al. This is an open access article distributed under the Creative Commons Attribution License, which permits unrestricted use, distribution, and reproduction in any medium, provided the original work is properly cited.

This is an experimental study which explores the physical, mechanical, and economic factors involved in the production of type CEM II A-B/W cement. In this context, 4 cement additives were used in two different dosages (200 and 800 g/t). Class C fly ash was used for composite cement production at ratios of 5%, 20%, and 35%. It was shown that Blaine fineness increases with the increasing fly ash content. The use of fly ash at ratios of 5% and 20% was not found to have any unfavorable effects on the compressive strength at the early days. It is found that the use of additive for improving the early-age strength is preferable when fly ash is used. It is possible to produce Class 52.5 N cement using additives to improve early strength and 20% fly ash. Loss in strength was observed in cement mortars produced using glycol-based grinding aid. Increasing the dosage of chemical additive also led to loss in strength due to nonhomogeneous distribution of hydration products. As a result, grinding fly ash with clinker and the use of cement chemicals contribute to the cement sector in terms of sustainability. It is possible to produce cements with improved mechanical properties especially with the use of 20% fly ash.

1. Introduction

Today, cement consumption in the world has reached up to a level of 4 billion tons/year. The power consumed during cement production is approx. 110 kW/ton, and around 30% of this power is used during raw material preparation phases and 40% is used in order to grind the cement clinker [1–3]. This power consumption rate leads to significant increase in costs especially in those regions where power is a rare commodity [4]. Along with the obligation to process increasingly larger quantities of ores containing finely disseminated minerals, our limited energy resources and the rising costs of energy present a challenge to the process engineer. One research route that has been explored for about half a century is the development of additives to the grinding mill feed that substantially improve the efficiency of grinding. Such additives are termed grinding aids. Grinding aids are used in order to reduce the electrostatic forces

between cement particles and their agglomeration. Grinding aids most commonly consist of ethanolamines such as triethanolamine (TEA) and triisopropanolamine (TIPA) along with glycols such as diethylene glycol (DEG) and propylene glycol (PG) [5]. Grinding aids are not capable of preserving their original molecular structures after the grinding process. Moreover, grinding aids are absorbed on the cement particles in a way to alter the properties of fresh and hardened concrete [6]. For example, grinding aids reinforced with TIPA molecules increase the cement hydration reactions which allow for improved compressive strength [5]. Ramachandran reported that TEA retards hydration of C_3S and β - C_2S while resulting in a number of changes in the morphology and microstructure of the hydration products. Hydration of C_3A is accelerated in case of the use of TEA [7]. Helen and Ölmez have found that hydration and setting time of cement is prolonged when the ethanolamine concentration is increased [8]. Ichikawa et al.

published findings suggesting that TIPA increases the hydration of limestone along with improving alite and ferrite hydration and that it thickens the interfacial transition zone (ITZ) between hydrated cement paste and aggregate particles [9]. Altun et al. showed that TIPA-based grinding aids, thanks to their operational benefits and properties to help improve quality, are more suitable for dry-mixed cement applications [10]. Zhang et al. analyzed the properties of polymer-based grinding aids (PGA). This study found that PGA has a significant effect on the particle size distribution of the cement and that this implies a rather narrower grading spectrum as the PGA dosage increases [11]. Li et al. used waste oil as grinding aid during cement grinding process. As a result, it was suggested that the use of waste oil as grinding aid in cement grinding process is economically and environmentally sustainable [12]. Zhang et al. used waste glycerin, industrial lignin, and molasses as grinding aids for composite cements. Results of the research showed that the grinding aids used improved mechanical properties of the composite cement while accelerating hydration [13]. A number of studies used PCEs as grinding aids. Results of these studies showed that the use of PCEs, when compared to TEA, improves the strength of the cement while offering the same grinding efficiency [14–16]. Sun et al. produced cement under laboratory conditions using polycarboxylate-based grinding aids. The use of polycarboxylate-based grinding aids during grinding process significantly improves the viscosity of cement paste while it did not have a significant negative effect on the other properties of cement [17]. Ghiasvand and Ramezani-pour produced composite cements with two and three components. They have also used limestone as one of these components. The authors suggested that the use of grinding aids is of utmost importance in order to produce high quality PLCs due to the agglomeration of limestone particles [18]. As a rule, the concentration range of the grinding aid used is very important in terms of the performance of cement. For example, 0.02% TEA addition to Portland cement acts as a setting accelerator, while 0.25% TEA addition acts as a mild setting retarder, 0.5% TEA addition, on the other hand, acts as a setting retarder, and 1% TEA addition acts as a strong setting accelerator [8].

The expectations on the properties of the concrete used in construction industry increase as the scale of the industrial production increases. Due to insufficient energy levels and natural resources, the demand for high-performance cement has gradually increased. A significant way to meet such demand is to produce high-performance cement, cement substitutes, and high-performance composites [19–21]. Recently, cement substitutes and composite cements have become increasingly available in concrete production [22]. Among some of the cement substitutes are fly ash which is a by-product of coal combustion, silica fume which is a by-product of ferrosilicon production process, and blast-furnace slag which is a waste produced during cast iron manufacturing. Fly ash is commonly known as a pozzolana with very poor hydraulic properties; however, it accelerates the hydration of cement thanks to its surface absorption effect and heterogeneous nucleation [23–25].

Therefore, fly ash may improve the mechanical properties and strength of cement-based materials [26–28]. In addition, fly ash particles may improve the workability of the fresh cement paste, thanks to their spherical particle geometry [29]. When cement-based composite materials are supported with fly ash, their performance is significantly improved and the microstructure of the composite material becomes more complex [30]. Therefore, it is important to use fly ash in concrete and cement production with respect to its role in economical, ecological, sustainability, strength, and durability factors.

2. Materials and Method

Portland cement clinker was used in the experimental study. Chemical properties of the clinker are given in Table 1. 5% (of the weight of clinker) gypsum was used to control the setting time in the production of cement. SO_3 content of gypsum was calculated to be 39.59%. Standard sand was used for the preparation of the samples in compliance with the EN 196-1 standard. Fly ash obtained from Yatagan Thermal Power Plant was used as a replacement for clinker in cement production. As Yatagan fly ash has more than 10% reactive lime, it is classified under Class W (calcareous fly ash) as per TS EN 197-1. As it has more than 50% $\text{SiO}_2 + \text{Al}_2\text{O}_3 + \text{Fe}_2\text{O}_3$ content and more than 10% CaO, it is classified under Class C (highly calcareous) as per the ASTM C 618. Chemical properties of the fly ash are given in Table 1. Chemical properties of the cement (0, 5, 20, and 35%) produced using fly ash and cement chemical are given in Table 1. Table 1 also shows the specific weight of fly ash and cements with fly ash.

Four cement chemicals were used in cement production, namely, two grinding aids and two strength enhancers for improving the early and final cement strength. The chemical additives used in cement production are commercially available and commonly used in cement factories operating in Turkey. Properties of the cement chemicals are given in Table 2.

Grinding technique was used in cement produced using clinker, limestone, and fly ash. A type bond ball mill was used to grind cement material. After placing clinker, limestone, and fly ash in the mill, chemicals were added on top of the mix. Cement chemicals with grinding aid and strength enhancing properties were used in dosages of 200 and 800 g/t, respectively. Fly ash, on the other hand, was used as a replacement for clinker at ratios of 5%, 20%, and 35%. A fixed grinding time of 120 minutes was used for all cement samples. Cement samples were produced in three groups. A total number of 33 cement samples, 24 of which including cement chemical and fly ash, 8 of which including cement chemical without fly ash, and 1 reference sample (without the use of fly ash and cement chemical), were prepared.

First, Blaine fineness of the cements produced was defined. Cement : aggregate : water content of the mortars was kept constant at 1 : 3 : 0.5, respectively. Hardened mortar samples were taken out of the cast after 24 hours and cured in limewater at 20°C until the experiment day. Uniaxial compression tests were conducted on the hardened mortar samples at 2nd, 7th, and 28th day. It was found that increased

TABLE 1: The chemical properties of clinker, fly ash, and cement.

(%)	OPC clinker	Fly ash	0%	5%	20%	35%
CaO	66.26	12.86	63.71	61.73	56.11	47.04
SiO ₂	21.77	50.41	19.45	23.49	27.21	32.08
Al ₂ O ₃	5.6	22.68	5.55	6.72	8.93	11.81
Fe ₂ O ₃	3.67	6.55	3.48	3.84	4.22	4.71
MgO	1.52	1.19	1.71	1.50	1.46	1.40
Na ₂ O	0.27	0.43	0.22	0.28	0.30	0.33
K ₂ O	0.37	1.69	0.63	0.45	0.62	0.85
SO ₃	0.26	1.71	2.98	2.80	2.33	1.95
Cl	0.0159	—	0.02	0.02	0.02	0.02
Loss on ignition	0.10	1.03	2.11	0.16	0.28	0.43
S. CaO	1.99					
C ₃ S	52.59					
C ₂ S	22.75					
C ₃ A	8.64					
C ₄ AF	11.16					
Specific weight		2.15	3.14	3.08	2.94	2.81

TABLE 2: Properties of cement additives.

Additive	Function of additive	Raw material	Density	pH	Color
Grinding aid (Ö1)	Grinding aid/energy saving	Polyethanolamine acetate	1.14	6–7	Light brown
Grinding aid (Ö2)	Grinding aid/energy saving	Polyethanolamine acetate modified with glycol	1.12	6–7	Brown
Strength enhancer (E)	Early-age strength enhancer	Modified hydroxylamines	1.15	10–12	Brown
Strength enhancer (N)	Final-age strength enhancer	Modified hydroxylamines	1.16	11–12	Brown

fly ash ratio has an unfavorable effect on the workability of the cement mortars. A number of pretests were performed in order to reduce such unfavorable effect, and the use of fly ash in combination with lime was studied. In terms of workability, as the use of 35% fly ash has an adverse impact on the mortar thickness, 35% fly ash was used with 5% lime dust which led to the production of the 34th cement type separate from the series. The reason behind this production was that lime, when it has the optimal fineness, reduces water need and bleeding while improving workability and strength. As particle size distribution of the cement is improved with lime addition, hardened mortar properties have also improved. Nevertheless, as lime accelerates the hydration of especially C₃S component of cement, it may improve its early-age strength. Lime forms nuclei regions for the sedimentation of CH crystals. With this nucleus effect, it accelerates the hydration of clinker particles, especially C₃S, which translates into improved early-age strength. Therefore, fresh and hardened mortar properties are analyzed adding 5% lime into the cement with 35% fly ash content.

3. Results and Discussion

3.1. Physical Properties of Cements. Blaine fineness of the cement samples were defined as part of the experimental

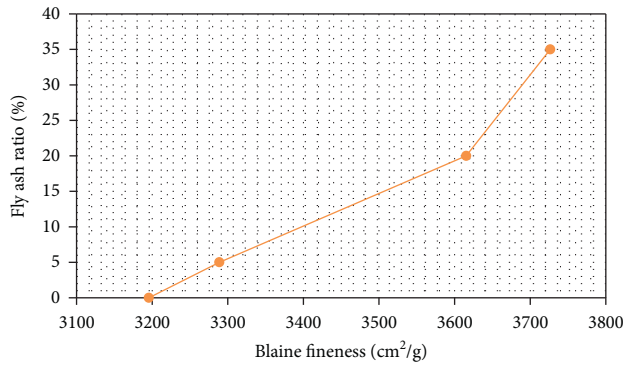
TABLE 3: Results of ANOVA test for Blaine fineness (significance level- $\alpha = 0.05$).

Blaine fineness	P value	Significance
Cement chemical	0.987	NS
Dosage of chem. additive	0.548	NS
Fly ash	0.000	S

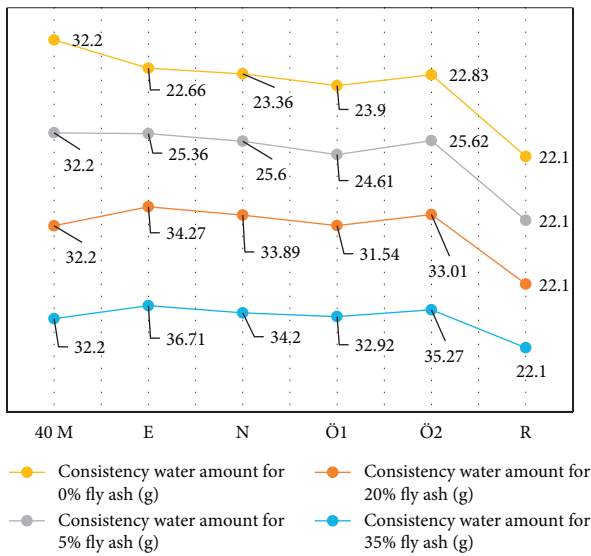
NS, not significant; S, significant.

study. ANOVA showed that the type and dosage of cement chemical used do not have an effect on the Blaine fineness. However, it was found that the ratio of fly ash used affects Blaine fineness. Results of ANOVA are given in Table 3. As shown in Table 3, the type and dosage of the cement chemical do not have an effect on the Blaine fineness as their P value is larger than 0.05. Figure 1 shows the effect of fly ash on Blaine fineness.

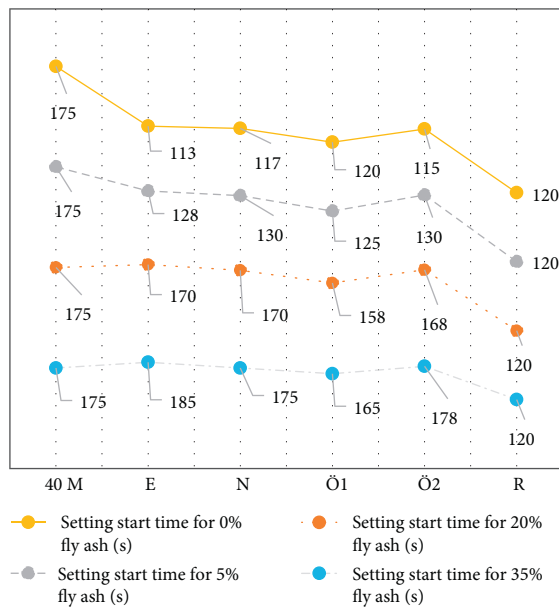
According to ANOVA shown in Table 3, parameters affecting the Blaine fineness were explored having identified their levels of impact. According to this impact analysis, the type ($0.987 > 0.05$, $P > \alpha$) and dosage of chemical additive ($0.548 > 0.05$, $P > \alpha$) do not affect the fineness of cement. The main parameter which affects the fineness of cement was found to be the fly ash content used. The reason behind the finding that fly ash has a higher impact level was that it has



(a)



(b)



(c)

FIGURE 1: (a) Effect of fly ash ratio on Blaine fineness. (b) Effect of fly ash ratio on consistency water amount. (c) Effect of fly ash ratio on setting start time (s).

a finer particle size distribution than clinker at the offset. Although chemical additives affect the grindability of clinkers under normal conditions, the use of mineral additives with finer particle sizes than clinker such as fly ash alters the importance of this effect. According to ANOVA analysis, the ratio of fly ash used in composite cement production directly affects the Blaine fineness values.

Blaine fineness of the cement produced without fly ash and using only cement chemical (0%) was 7% higher than that of the reference cement. However, it was shown that Blaine fineness increases significantly with the increasing fly ash content. Especially in the case where fly ash content was 20%, Blaine fineness was found in a range between 3570 and 3660 cm²/g. Where fly ash content was 35%, on the other hand, Blaine fineness was found to reach up to approx. 3800 cm²/g. Blaine fineness of the cement produced using 35% fly ash and 5% lime dust (% 40 M) was found to be 3770 cm²/g. Increasing level of fly ash also increases the Blaine fineness. Grinding fly ash with clinker plays an important role in increasing cement fineness.

ANOVA showed that the type and dosage of cement chemical used do not have an effect on water demand and setting time (Table 4). Also showed by the ANOVA was the fact that the ratio of fly ash affects water demand and setting time. Results of the ANOVA performed for water demand and setting time are given in Table 4.

Water demand and initial setting time are increased with the increase in the fly ash content used. Initial setting time is delayed as the clinker used is reduced in weight. As a result of increased fly ash content, Blaine fineness is increased and therefore water demand of the cement paste is also increased. Increasing level of fly ash also increases the water demand of the paste. The increase in water demand, on the other hand, is another factor in increasing setting time.

Figure 1(b) shows the effect of fly ash content on water demand. Water demand of the cements produced using only cement chemical is higher than that of the reference cement. This can be explained with the fact that Blaine fineness of the reference cement is lower. When the fly ash content was 35%, the water demand changed between 33.5% and 36.0%. The water demand of the cement with 5% lime dust in order to offset the loss in workability due to the increased fly ash content was 32.2%. Here, the use of lime dust is found to reduce the water demand notwithstanding the high Blaine fineness. Figure 1(c) shows the effect of fly ash content on initial setting time. The increase in fly ash content also increases initial setting time. Initial setting time of the cement with cement chemical and without fly ash (0%) was shorter than that of the reference cement. Setting times of the cement with 5% lime dust (% 40 M), on the other hand, were quite similar to those of cement with 35% fly ash content.

3.2. Compressive Strength of Cements

3.2.1. The Effect of Fly Ash Content on the Compressive Strength. Figure 2(a) shows the effect of fly ash content on 2-day compressive strength. Where the fly ash content is 5%, it was found that compressive strength increases. Compressive

TABLE 4: Results of ANOVA test for water demand and setting time (significance level $\alpha = 0.05$).

Water demand	P value	Significance	Setting time	P value	Significance
Cement chemical	0.958	NS	Cement chemical	0.912	NS
Dosage of chem. additive	0.367	NS	Dosage of chem. additive	0.299	NS
Fly ash	0.000	S	Fly ash	0.000	S

NS, not significant; S, significant.

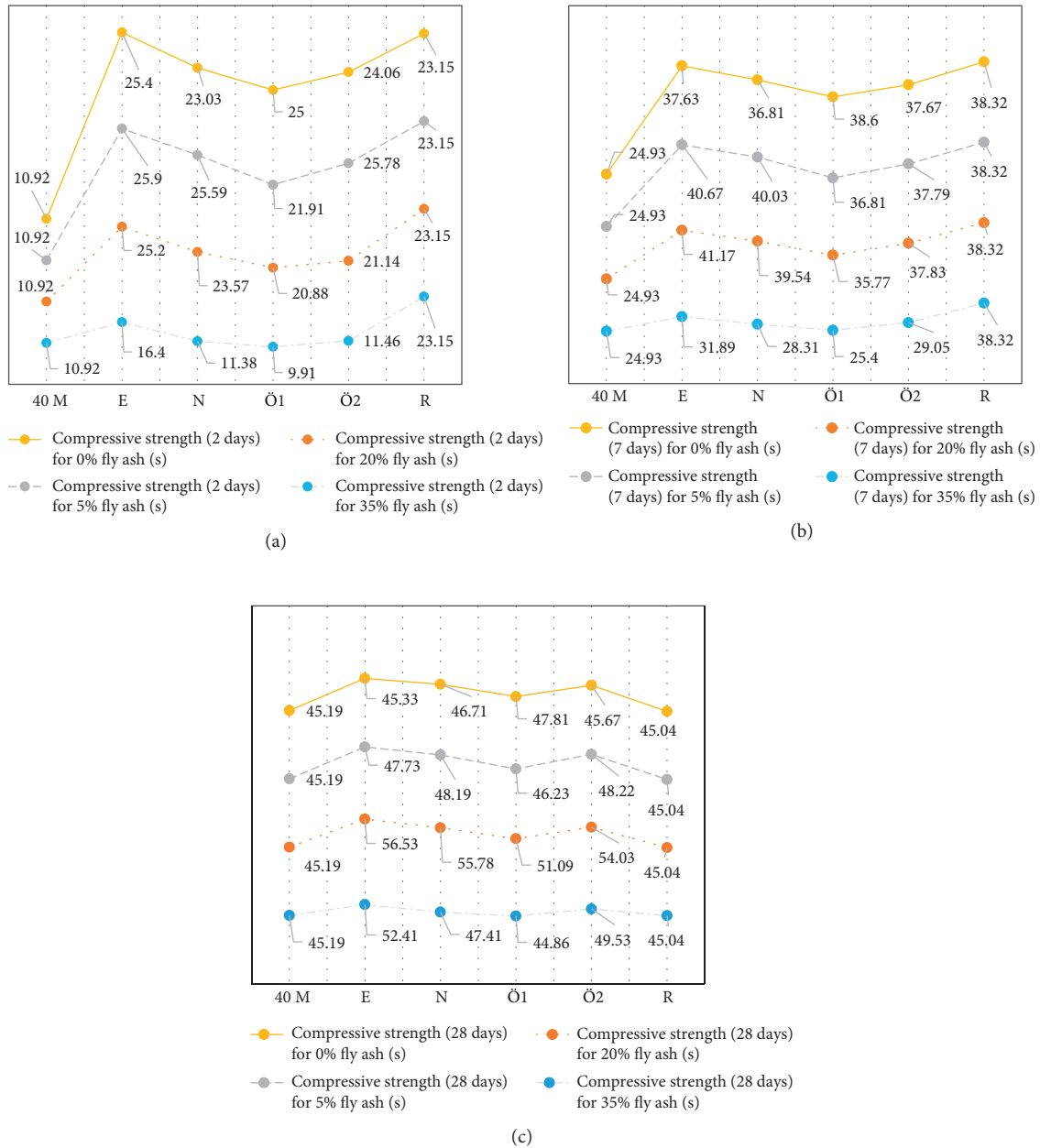


FIGURE 2: (a) Effect of fly ash ratio on early compressive strength (MPa). (b) Effect of fly ash ratio on 7-day compressive strength (MPa). (c) Effect of fly ash ratio on 28-day compressive strength (MPa).

strength was in the range between 22.97 and 26.62 MPa when the fly ash content was 5%; 20.87–24.52 MPa when the fly ash content was 20%; and 10.46–14.11 when the fly ash content was 35%. 2-day compressive strength of the cement with cement chemical and without fly ash (0%) was in the

range between 22.54 and 26.19 MPa. When the fly ash content was 5%, compressive strength was approx. 7.1% higher than that of the reference cement; when the fly ash content was 35%, compressive strength was approx. 46.9% lower than that of the reference cement. Compressive

strength of the cement produced using 35% fly ash and 5% lime dust (% 40 M) was found to be 10.92 MPa.

Figure 2(b) shows the effect of fly ash content on 7-day compressive strength. Where the fly ash content is 5% and 20%, it was found that 7-day compressive strength increases. 7-day compressive strength was in the range between 36.94 and 40.71 MPa when the fly ash content was 5%; 36.69–40.69 MPa when the fly ash content was 20%; and 26.77–30.55 when the fly ash content was 35%. Where the fly ash content was 5% and 20%, compressive strength was approx. 0.75% higher than that of the reference cement. However, 7-day compressive strength decreases by approx. 25.3% when fly ash content is 35%. Cement with 40% mineral additive (% 40 M) has a 7-day compressive strength of 25 MPa. Cement produced with cement chemical and without fly ash is found to have a compressive strength similar to that of the reference cement.

A closer look into 28-day compressive strength values showed that these values differ greatly from 2-day and 7-day compressive strength values (Figure 2(c)). Especially, the use of 35% fly ash was found to significantly increase 28-day compressive strength. 28-day compressive strength was in the range between 45.07 and 50.11 MPa when the fly ash content was 5%; 51.84–56.87 MPa when the fly ash content was 20%; and 46.03–51.07 when the fly ash content was 35%. 28-day compressive strength of the cement with cement chemical and without fly ash (0%) was in the range between 43.86 and 48.66 MPa. However, 28-day compressive strength increases by approx. 20.7% when the fly ash content is 20%. Nevertheless, compressive strength of the cement with 35% fly ash content with rather low 2-day and 7-day compressive strengths was found to increase by 7.8%. 28-day compressive strength of the cement produced using 35% fly ash and 5% lime dust was found to be similar to that of the reference cement as shown in Figure 2(c).

Two-day compressive strength is found to be in the range between 16.38 and 24.83 MPa when additive Ö1 is used; 16.66–25.12 MPa when additive N is used; 19.00–27.45 MPa when additive E is used; and 15.19–23.65 MPa when additive Ö2 is used. Affecting the early-age strength, additive E offers a 2-day compressive strength similar to that of the reference cement. Additives Ö1 and N offer similar 2-day compressive strength patterns. Additive Ö2, a grinding aid, was found to have negligible effect on the strength (for early ages). The fact that additive E is a hydroxylamine-based additive (TEA/TIPA) accelerates the hydration of C_3S available in the clinker. Similar effect was also observed when additive N was used. As additive Ö2 has a glycol content, it resulted in mild reductions in the compressive strength.

Additives Ö1 and N offer similar 28-day compressive strength patterns. Compressive strength of the additives Ö1 and N was in the range between 46.00 and 52.88 MPa. Compressive strength is increased by 12.1% when compared to the reference cement when additive E is used. When additive Ö2 is used, 28-day compressive strength was in the range between 44.13 and 50.82 MPa. Although additive Ö2 did not have a positive effect on the 2-day and 7-day compressive strength, it was found to have a significant effect on the 28-day compressive strength.

Among the grinding aids, additive Ö2 containing glycol consistently gave low compressive strength values throughout

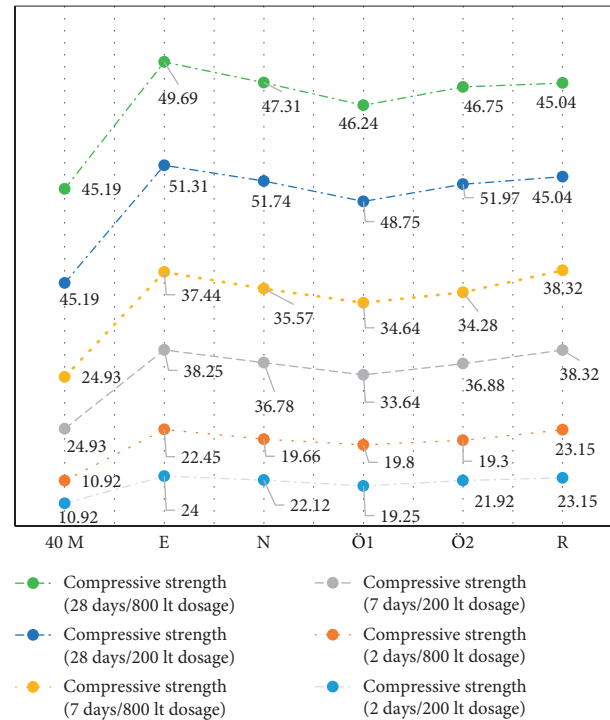


FIGURE 3: Effect of cement chemical additive dosage on compressive strength.

the tests. However, these differences were negligible. The literature reported increased compressive strength with the use of glycol-based additives. But this study found loss in compressive strength. It is believed that chemical properties of the clinker or the temperature in the mill during grinding may account for this result. Additive E with hydroxylamine, on the other hand, has a rather positive effect on both early and final strengths of the cement. Such an effect can be accounted for with the use of TEA and TIPA in strength enhancers.

3.2.2. The Effect of Cement Chemical Dosage on Compressive Strength. The effects of cement chemical dosage on compressive strength are shown in Figure 3. When the chemical is used at a dosage of 200 g/t, 2-day compressive strength was in the range between 18.88 and 24.76 MPa. When the chemical is used at a dosage of 800 g/t, 2-day compressive strength was approx. 12.5% lower than that of the reference cement. Figure 3 shows that increasing chemical dosage decreases compressive strength.

A closer look into 7-day compressive strength results shows that increasing chemical dosage results in decreased strength. The strength was found to be lower than that of the reference cement especially in the case where cement chemical was used at a dosage of 800 g/t. When the chemical is used at a dosage of 200 g/t, 7-day compressive strength was 38.94 MPa for the cements produced.

The effects of cement chemical dosage on 28-day compressive strength are shown in Figure 3. Increasing the cement chemical dosage has an unfavorable effect on the 28-day compressive strength as it was the case for 2-day and 7-day compressive strengths. When the chemical is used at a dosage

TABLE 5: Unit prices of the material used in cement production (in Turkey).

		Unit price (\$/ton)
Clinker		23.03
Limestone		14.11
Fly ash		7.11
Chem. admix.	E	0.16
	N	0.19
	Ö1	0.22
	Ö2	0.27
Electrical energy (kw/h)		10.69

of 200 g/t, the compressive strength was approx. 13.1% higher than that of the reference cement. However, 28-day compressive strength increases by approx. 5.5% when the dosage is 800 g/t. Figure 3 shows that cement with lime dust (% 40 M) and reference cement have similar properties. Moreover, the reduction in compressive strength due to increased additive dosage is accounted for with the agglomeration. In some cases where excessive amounts of chemical additive are used, agglomeration may reoccur. Furthermore, increased additive dosage decreases the initial setting time. When the dosage is 800 g/t, the mortar loses its water content very fast and it hardens. The result is nonhomogeneous distribution of hydration products in the structure and crack development in the structure which are the causes of lower strength.

3.3. Cost and Optimization. Table 5 shows the unit prices (for Turkey) of clinker, limestone, fly ash, chemical additive, and electrical energy used in the cement production. Prices listed refer to the price for 1 ton.

As the cost of additives Ö1 and Ö2 is higher in terms of chemical type used, it is more affordable to use additives E and N. Increase in the amount of fly ash used often increases the cement cost. Cost analysis shows that the use of additive E is more beneficial. The fly ash content also plays a role in cement cost reduction (Figure 4). When the fly ash content is 20%, the cost of cement is in the range between 20 and 25 \$/ton. Considering also the strength of the cement as a factor, the use of 20% fly ash is the optimal solution.

An optimization study was conducted for the cement samples with fly ash content under laboratory conditions. Cement with lime was also included in this optimization process. Optimization process included only the cement with fly ash and chemical additive. Compressive strength and cost are the most important parameters in cement production. TS EN 197-1 standard imposes restriction on the 2-day and 28-day compressive strengths of cements. Therefore, the optimization process aimed for maximum level of 2-day and 28-day compressive strengths. And the cost parameter was aimed to be minimal for the cements produced. Functions used in the optimization process are shown in Table 6.

According to the parameters shown in Table 6, the most viable cement properties are obtained with 20% fly ash, additive E, and grinding at a dosage of 200 g/t. Table 7 shows

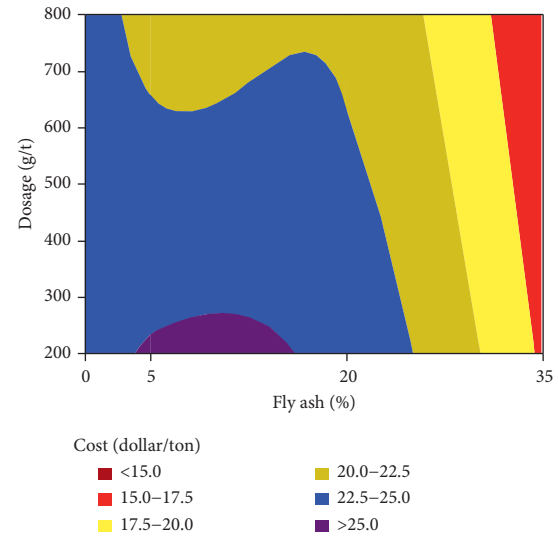


FIGURE 4: The effect of fly ash content and additive dosage on the cost (in Turkey).

TABLE 6: Optimization parameters used in cement production.

Objective function	Characteristic
2-day compressive strength (MPa)	Maximize
28-day compressive strength (MPa)	Maximize
Cost (\$)	Minimize

TABLE 7: A comparison of the reference cement and the optimal cement.

	Reference cement	Optimal cement	Difference (%)
2-day compressive strength (MPa)	23.15	25.66	10.8
28-day compressive strength (MPa)	45.04	56.57	25.6
Cost (\$)	26.78	24.19	9.7

a comparison of the cement produced using the above-mentioned properties with the reference cement.

4. Results

This study analyzed the production of type CEM II A-B/W cement with the replacement of Portland cement clinker with Class C fly ash at ratios of 5%, 20%, and 35%. During the cement grinding process, 4 different cement chemicals were included at dosages of 200 and 800 g/t. The following findings were obtained as a result of this study:

- (1) The impact of the type and dosage of cement chemical on the water demand and setting times was insignificant. The fly ash content did not affect setting time and water demand. Increase in the fly ash

content also increases water demand. Nevertheless, increase in fly ash content also increases initial setting time and final setting time.

- (2) Increasing fly ash content directly affects the Blaine fineness of cements. Cements with approx. $3800 \text{ cm}^2/\text{g}$ Blaine fineness were produced using fly ash at a ratio of 35%. Blaine fineness of the cement produced without fly ash and using only cement chemical was 7% higher than that of the reference cement.
- (3) An increase in the fly ash content decreases early-age strength (2 and 7 days); however, such an increase has a favorable impact on the final-age strength. Especially, the use of 20% fly ash makes it possible to produce cement with 52.5 N strength class. Where the fly ash content is 35%, it is possible to produce cement with 42.5 N strength class. Moreover, using 35% fly ash content, it was possible to obtain cement complying with 52.5 L strength class for type CEM III cements.
- (4) Additives E and N (strength enhancers) had a positive impact on the mechanical properties of the cements. However, increasing the additive dosage decreases compressive strength of cements. The use of strength enhancers offers better results in cements with fly ash.
- (5) As a result, it is possible to produce high-performance cement using fly ash. Especially, the use of fly ash at the ratios of 20% and 35% plays an important role in reducing CO_2 emissions. The use of strength enhancers is more suitable in cement with fly ash.

Conflicts of Interest

The authors declare that they have no conflicts of interest.

References

- [1] A. Jankovic, W. Valery, and E. Davis, "Cement grinding optimisation," *Minerals Engineering*, vol. 17, no. 11-12, pp. 1075-1081, 2004.
- [2] H. Dundar, H. Benzer, N. A. Aydogan et al., "Simulation assisted capacity improvement of cement grinding circuit: case study cement plant," *Minerals Engineering*, vol. 24, no. 3-4, pp. 205-210, 2011.
- [3] H. Benzer, L. Ergün, M. Öner, and A. J. Lynch, "Simulation of open circuit clinker grinding," *Minerals Engineering*, vol. 14, no. 7, pp. 701-710, 2001.
- [4] G. Atesok, M. Ozer, F. Boylu, and H. Dincer, "The effect of anionic dispersants on grindability of different rank coals," *International Journal of Mineral Processing*, vol. 77, no. 4, pp. 199-207, 2005.
- [5] J. J. Assaad, "Industrial versus Laboratory clinker processing using grinding aids (scale effect)," *Advances in Materials Science and Engineering*, vol. 2015, Article ID 938176, 12 pages, 2015.
- [6] J. J. Assaad and C. A. Issa, "Effect of clinker grinding aids on flow of cement-based materials," *Cement and Concrete Research*, vol. 63, pp. 1-11, 2014.
- [7] V. S. Ramachandran, "Hydration of cement—role of triethanolamine," *Cement and Concrete Research*, vol. 6, no. 5, pp. 623-631, 1976.
- [8] Z. Heren and H. Ölmez, "The influence of ethanolamines on the hydration and mechanical properties of Portland cement," *Cement and Concrete Research*, vol. 26, no. 5, pp. 701-705, 1996.
- [9] M. Ichikawa, M. Kanaya, and S. Sano, "Effect of triisopropanolamine on hydration and strength development of cements with different character," in *Proceedings of the 10th International Congress on the Chemistry of Cement*, vol. 3, p. 3iii005, Gothenburg, Sweden, 1997.
- [10] O. Altun, H. Benzer, A. Toprak, and U. Enderle, "Utilization of grinding aids in dry horizontal stirred milling," *Powder Technology*, vol. 286, pp. 610-615, 2015.
- [11] T. Zhang, J. Gao, and J. Hu, "Preparation of polymer-based cement grinding aid and their performance on grindability," *Construction and Building Materials*, vol. 75, pp. 163-168, 2015.
- [12] H. Li, J. Zhao, Y. Huang et al., "Investigation on the potential of waste cooking oil as a grinding aid in Portland cement," *Journal of Environmental Management*, vol. 184, pp. 545-551, 2016.
- [13] Y. Zhang, A. Fei, and D. Li, "Utilization of waste glycerin, industry lignin and cane molasses as grinding aids in blended cement," *Construction and Building Materials*, vol. 123, pp. 785-791, 2016.
- [14] T. Heller, T. Müller, and D. Honert, "Cement additives based on PCE," *ZKG International*, vol. 64, no. 2, pp. 40-48, 2011.
- [15] E. Sakai, A. Ishida, and A. Ohta, "New trends in the development of chemical admixtures in Japan," *Journal of Advanced Concrete Technology*, vol. 4, no. 2, pp. 211-223, 2006.
- [16] J. Plank, E. Sakai, C. W. Miao, C. Yu, and J. X. Hong, "Chemical admixtures—chemistry, applications and their impact on concrete microstructure and durability," *Cement and Concrete Research*, vol. 78, pp. 81-99, 2015.
- [17] Z. Sun, H. Yanga, L. Shui et al., "Preparation of polycarboxylate-based grinding aid and its influence on cement properties under laboratory condition," *Construction and Building Materials*, vol. 127, pp. 363-368, 2016.
- [18] E. Ghiasvand and A. A. Ramezani-pour, "Effect of grinding method and particle size distribution on long term properties of binary and ternary cements," *Construction and Building Materials*, vol. 134, pp. 75-82, 2017.
- [19] K. H. Yang, Y. B. Jung, M. S. Cho, and S. H. Tae, "Effect of supplementary cementitious materials on reduction of CO_2 emissions from concrete," *Journal of Cleaner Production*, vol. 103, pp. 774-783, 2015.
- [20] T. Sato and J. J. Beaudoin, "Effect of nano- CaCO_3 on hydration of cement containing supplementary cementitious materials," *Advances in Cement Research*, vol. 23, no. 1, pp. 33-43, 2011.
- [21] Z. Liu, Y. Zhang, and Q. Jiang, "Continuous tracking of the relationship between resistivity and pore structure of cement pastes," *Construction and Building Materials*, vol. 53, pp. 26-31, 2014.
- [22] R. Snellings, "Assessing, understanding and unlocking supplementary cementitious materials," *RILEM Technical Letters*, vol. 1, p. 50, 2016.
- [23] L. Lam, Y. L. Wong, and C. S. Poon, "Degree of hydration and gel/space ratio of high-volume fly ash/cement systems," *Cement and Concrete Research*, vol. 30, no. 5, pp. 747-756, 2000.
- [24] P. Hou, S. Kawashima, D. Kong, D. J. Corr, J. Qian, and S. P. Shah, "Modification effects of colloidal nano SiO_2 on

- cement hydration and its gel property,” *Composites Part B: Engineering*, vol. 45, no. 1, pp. 440–448, 2013.
- [25] M. Ahmaruzzaman, “A review on the utilization of fly ash,” *Progress in Energy and Combustion Science*, vol. 36, no. 3, pp. 327–363, 2010.
- [26] J. David Raja Selvam, D. S. Robinson Smart, and I. Dinaharan, “Microstructure and some mechanical properties of fly ash particulate reinforced AA6061 aluminum alloy composites prepared by compositing,” *Materials & Design*, vol. 49, pp. 28–34, 2013.
- [27] R. Feldman, L. R. Prudencio, and G. Chan, “Rapid chloride permeability test on blended cement and other concretes: correlations between charge, initial current and conductivity,” *Construction and Building Materials*, vol. 13, no. 3, pp. 149–154, 1999.
- [28] S. W. M. Supit and F. U. A. Shaikh, “Durability properties of high volume fly ash concrete containing nano-silica,” *Materials and Structures*, vol. 48, no. 8, pp. 2431–2445, 2014.
- [29] N. Neithalath and J. Jain, “Relating rapid chloride transport parameters of concretes to microstructural features extracted from electrical impedance,” *Cement and Concrete Research*, vol. 40, no. 7, pp. 1041–1051, 2010.
- [30] Z. Liu, D. Xu, and Y. Zhang, “Experimental investigation and quantitative calculation of the degree of hydration and products in fly ash-cement mixtures,” *Advances in Materials Science and Engineering*, vol. 2017, Article ID 2437270, 12 pages, 2017.

Research Article

Optimal Cement Mixtures Containing Mineral Admixtures under Multiple and Conflicting Criteria

Nitza M. García,¹ Hildélix L. Soto-Toro ,² Mauricio Cabrera-Ríos,¹ and Oscar Marcelo Suárez ³

¹Department of Industrial Engineering, University of Puerto Rico, Mayagüez, PR, USA

²Department of Civil Engineering and Surveying, University of Puerto Rico, Mayagüez, PR, USA

³Department of Engineering Science and Materials, University of Puerto Rico, Mayagüez, PR, USA

Correspondence should be addressed to Hildélix L. Soto-Toro; hildelix.soto@upr.edu

Received 6 July 2017; Revised 3 November 2017; Accepted 15 November 2017; Published 17 January 2018

Academic Editor: Tayfun Dede

Copyright © 2018 Nitza M. García et al. This is an open access article distributed under the Creative Commons Attribution License, which permits unrestricted use, distribution, and reproduction in any medium, provided the original work is properly cited.

In modern construction industry, fabrication of sustainable concrete has turned the decision-making process into a challenging endeavor. One alternative is using fly ash and nanostructured silica as cement replacements. In these modern mixtures, proper concrete bulk density, percentage of voids, and compressive strength normally cannot be optimized individually. Hereby, a decision-making strategy on the replacement of those components is presented while taking into account those three performance measurements. The relationships among those components upon concrete fabrication required a design of experiments of mixtures to characterize those mineral admixtures. This approach integrates different objective functions that are in conflict and obtains the best compromise mixtures for the performance measures being considered. This optimization strategy permitted to recommend the combined use of fly ash and nanosilica to improve the concrete properties at its early age.

1. Introduction

In recent years, the environmental damages caused by the production of building materials have compelled the construction industry to seek for sustainable alternatives [1]. The partial replacement of cement by fly ash (FA), a manufacturing waste of the burning coal process, has turned into an increasingly popular alternative. Further, the addition of nanostructured SiO₂ or nanosilica (nS) is highly recommended to counterbalance the loss of concrete compressive strength at early age caused by FA. These nanoparticles improve some valuable concrete properties such as the density, porosity, and compressive strength [2–5]. Of those properties, concrete compressive strength is the most relevant mechanical property and, therefore, the most studied [6]. Moreover, assessment of concrete porosity is necessary as this is related to concrete's durability and permeability [7, 8]. Those characteristics depend on the number, size, and distribution of pores in the cement paste and the aggregates [9].

Hence, a range of values of the mechanical and physical properties of concrete are preferred when mineral admixtures

are utilized [10, 11], as the desired characteristics depend on the proposed application. Previous works demonstrated that the specimens with higher compressive strength not necessarily corresponded to the ones with higher density and lower porosity, which are usually the desirable properties in concrete structures [12, 13]. That is why, in some cases, designers have to prioritize, for example, one characteristic over other ones. Therefore, there arises a conflict among the different performance measures of concrete. As a result, one must utilize a multiple criteria optimization method to maximize simultaneously compressive strength and density to minimize the concrete porosity. Finally, the use of this approach helps to design a multifunctional structural material by identifying the mixtures that belong to a Pareto-efficient frontier [14, 15]. The resulting optimized mixtures would become the best compromise among all performance measures between the set of mixtures under evaluation.

Optimization is, therefore, a decision-making tool of great importance issue in the construction industry [16], where simultaneous attention is required for the environmental aspects and design factors. These frequently

contradict each other especially when recycled materials (with their inherent behavioral variability) are involved.

Often, researchers have used regression models to predict performance measures, such as compressive strength, density, and porosity [17–20]. Sometimes, via neural networks, some were able to predict concrete behavior [19]. In addition, although a visual representation of the results facilitates the comparison process, other statistical methodologies can be used to compare the mixtures from a mathematical viewpoint rather than from a more subjective approach. Therefore, researchers have employed a variety of optimization approaches to find the best possible solutions in a single objective [1, 17, 21–26]. Recommendations based on all the performance measures of interest to the user are more appropriate when compared with only the selection of a single solution pertaining to the measured objective.

To address this situation, different attempts to incorporate multiple performance measures can be found [27, 28]. For instance, the ϵ -constraint method, which is a formal approach to multicriteria optimization, permitted to resolve a multiobjective reliability-based optimum problem of prestressed concrete beams [29]. Most methods provided by the literature require target values—necessarily defined *a priori*—or reduce the multiobjective problem into a single objective optimization problem to find the optimal set. As a consequence, we posit a methodology that does not involve any of the previously mentioned issues that has been developed at the University of Puerto Rico-Mayagüez (UPRM) [13, 14, 30]. This methodology renders the Pareto-optimal solution set by just defining the objectives and their respective (maximization/minimization) directions. Often, when solving a multiple criteria optimization problem, one can find a set of efficient solutions. Such a set is also known as “Pareto-optimal solutions” [14, 30, 31]. These solutions are the best balances among all performance measures under evaluation; they are equally optimal since a gain in one objective results in a sacrifice in at least another objective. The optimal solutions form the Pareto-efficient frontier.

In order to identify those optimal solutions, one utilizes the Pareto-optimality conditions as described in Deb’s work [31]. In this work, the author stated that “A solution $x^{(1)}$ is said to dominate the other solution $x^{(2)}$, if both the following conditions are true:

- (1) The solution $x^{(1)}$ is no worse than $x^{(2)}$ in all objectives. Thus, the solutions are compared based on their objective function values (or location of the corresponding points ($z^{(1)}$ and $z^{(2)}$) on the objective space).
- (2) The solution $x^{(1)}$ is strictly better than $x^{(2)}$ in at least one objective.”

Consequently, based on the said concepts and findings, the present work focuses on the characterization of concrete-containing mineral admixtures and the subsequent multiple criteria optimization. First, a statistical design of experiments for mixtures allowed computing the mixture proportions to evaluate. Subsequently, the optimal tradeoff mixtures among compressive strength, bulk density, and percentage of voids

followed. Utilizing the above conditions, we performed a full pairwise comparison between the solutions to eventually find the Pareto-efficient frontier or the nondominated set. Accordingly, we present a decision-making strategy on the replacement of concrete components while taking into account the material’s physical and mechanical properties.

2. Experimental Methodology

2.1. Material Selection. Via a sieve analysis (ASTM 136) [32], the experimental proportions of the aggregates were determined as 30% of gravel grade #7 (ASTM C33) [33], 35% of processed aggregate (limestone), and 35% of clean sand. To determine the quantity of polycarboxylate superplasticizer (SP) necessary for each mixture, we took into account the following characteristics of the mixtures: segregation, bleeding, slump, and consistency. This mini-slump test was used for the mixtures at 5, 30, and 60 minutes after the mixing along with a trial-and-error method to find the right proportion of superplasticizer for each mix. The evaluation criteria for slump were 100–152 mm to obtain optimum SP quantity (ASTM C143) [34].

2.1.1. Aggregates. We used gravel as coarse aggregate, with a maximum nominal size of 19.0 mm. Moreover, the processed aggregate (limestone) had a maximum nominal size of 9.5 mm. The fineness modulus of the fine aggregate was 3.0 as given in Table 1.

2.1.2. Portland Cement. We used ordinary Portland cement (OPC) Type I (ASTM C150) [35], which is classified as applicable to general purposes and have fairly high C_3S content for good early strength development with a specific gravity of 3.06.

2.1.3. Fly Ash. The FA class F (ASTM C618) [36] with a specific gravity of 2.38 was selected.

2.1.4. Nanosilica. Nissan Chemical Industries provided the nS used, which was opalescent and odorless amorphous silica dispersed in water, with a particle mean size of 69.40 nm and specific gravity of 2.03. The amounts of nS in the mixes are calculated based on the percentage by weight of solid in the colloidal solution. In the case of these nanoparticles, only 45% by weight is SiO_2 . To calculate the amounts of nS for the mixtures, the amount of water and solids is considered, thus making an adjustment to the amounts of both nS and water, in order to then reach the percent established for the design. For instance, the amount of nanosilica was computed as follows:

Mix design k : 9 = (PC: 0.57, FA: 0.40, and nS: 0.03)

Total cementitious quantity: 672 kg/m^3

nS (solids) = $45 * 45\% = 20 \text{ kg/m}^3$

FA = 269 kg/m^3

PC = 383 kg/m^3

Sum = 672 kg/m^3

TABLE 1: Properties of the aggregates.

Aggregate	Apparent specific gravity	Specific gravity (oven-dry)	Specific gravity (SSD)	Absorption (%)	Unit weight (kg/m ³)
Gravel	2.88	2.71	2.77	2.09	1584.70
Limestone	2.77	2.50	2.59	3.86	1740.57
Beach sand	2.65	2.42	2.51	3.48	1460.54

2.1.5. *Superplasticizer.* The polycarboxylate superplasticizer used followed the ASTM 494 standard [37] and was provided by a company in Puerto Rico.

2.1.6. *Water.* To prepare the mixtures, we employed tap water at room temperature available at the UPRM Construction Materials Laboratory.

2.2. *Fabrication and Testing Procedures.* A gear-driven, high-torque transmission 5 L mixer (Globe SP20) manufactured by Globe Food Equipment was used to mix the concrete components. The coarse and fine aggregates were first dry-mixed and then placed into the mixer for 0.25 min at 120 rpm, followed by half of the required water. Then, we added the PC and later the FA (if required by the specific experiment) with the mixture working for 0.25 min at 60 rpm. The nS and SP were diluted in water in order to obtain a uniform particle distribution throughout the mixture and poured into the mixer (when used) for 4.30 min at 120 rpm. The cylindrical molds were filled by the rodding method according to ASTM C192 [38]. We removed the cylinders formwork 24 hours after casting; thereupon, we immersed them into limewater until tested at normal curing conditions (20–23°C and RH = 100%). The temperature (23–25°C) was relatively constant in the laboratory.

Following ASTM C642-13 standard [39], we measured the density and percentage of voids of five specimens at 7 and 28 days of curing. We considered the specimen oven-dry mass, its saturated mass after immersion in water, its saturated mass after boiling, and its immersed apparent mass. These values were used to calculate the bulk density and the volume of permeable pore space or percentage of voids of the specimens. The dimensions of the test cylinders were 76 mm in diameter and 152 mm in length to meet the minimum volume required by the standard.

For the compressive strength test, the dimensions of the test cylinders were 50 mm in diameter and 100 mm in length. We tested the compressive strength of six cylinders at 7 and 28 days of curing, using a 3000 kN Forney universal test machine according to ASTM C39 [40].

2.3. *Design of Experiments.* In order to generate the different combinations of the cement mixture components, that is, PC, FA, and nS [24, 41], we set up a design of experiments for mixtures. This methodology is explained in detail in our previous publication [3]. In the present work, the upper bound was set at 3% of nS and 40% of FA. In addition, the water-to-binder ratio utilized for all mixtures remained constant at 0.3.

TABLE 2: Mixture proportion combinations evaluated of cement mixtures.

k	Mixture proportions (PC/FA/nS)	PC kg/m ³	FA kg/m ³	nS kg/m ³	Gravel kg/m ³	Sands kg/m ³
1	0.800/0.20/0.000	538	134	0	1001	431
2	1.000/0.00/0.000	672	0	0	1001	462
3	0.600/0.40/0.000	403	269	0	1001	400
4	0.585/0.40/0.015	393	269	22	1001	396
5	0.770/0.20/0.030	518	134	45	1001	423
6	0.985/0.00/0.015	662	0	22	1001	458
7	0.970/0.00/0.030	652	0	45	1001	454
8	0.785/0.20/0.015	528	134	22	1001	427
9	0.570/0.40/0.030	383	269	45	1001	392

TABLE 3: Setup of the multiple criteria optimization problem.

Decision variables	PC, FA, and nS
Maximization of	$f_1(x)$: compression strength $f_2(x)$: bulk density
Minimization of	$f_3(x)$: percentage of voids
Subject to these constraints	$0.57 \leq \text{PC} \leq 1.00$ $0.00 \leq \text{FA} \leq 0.40$ $0.00 \leq \text{nS} \leq 0.03$

Table 2 presents the nine-component combinations or mixtures evaluated, as fractions of 1.00 (total mass of the mixture). Each mixture represents a solution k with different characteristics in terms of physical and mechanical properties of the resulting concrete. A multiple criteria optimization method helped us in the decision-making process of recommending some of these mixtures.

In this multiple criteria optimization problem, we were interested in recommending a set of alternatives (k^*) selected from the different mixture proportions of PC, FA, and nS. In view of that, the final decision-making would be based on the following material performance measures: compressive strength, bulk density, and percentage of voids. Naturally, the desired outcomes were higher compressive strength and density and lower percentage of voids. Thus, the strategy for the multiple criteria optimization problem is presented in Table 3.

We intended to restrict the problem described above to a manageable number of sampling experimental solutions generated through a mixture design of experiments (DOE), as mentioned previously. Furthermore, the best tradeoffs among the competing criteria were identified with the application of Pareto-optimality conditions, as advocated in prior research [14, 15, 42]. This method is exact (as opposed to a heuristic approach [18]) and has been utilized

TABLE 4: Average result of performance measures at day 7.

k	Component fractions (PC/FA/nS)	Compressive strength		Bulk density		Volume of permeable pore space	
		Average MPa	Std. dev. MPa	Average kg/m ³	Std. dev. kg/m ³	Average %	Std. dev. %
1	0.800/0.20/0.000	27.37	1.15	2165.88	37.32	15.59	0.98
2	1.000/0.00/0.000	31.11	7.22	2218.43	34.71	13.85	0.75
3	0.600/0.40/0.000	33.71	3.19	2117.88	13.27	17.42	0.32
4	0.585/0.40/0.015	31.58	5.32	2125.56	29.80	16.58	0.70
5	0.770/0.20/0.030	29.75	5.24	2186.46	16.19	15.93	0.63
6	0.985/0.00/0.015	27.03	5.65	2188.51	37.78	16.00	1.05
7	0.970/0.00/0.030	24.19	8.24	2189.98	14.19	16.04	0.31
8	0.785/0.20/0.015	40.40	2.47	2156.64	6.26	17.00	0.28
9	0.570/0.40/0.030	33.35	4.63	2163.49	23.10	12.49	0.78

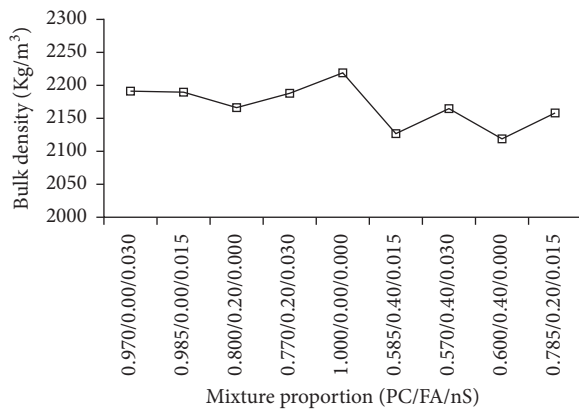


FIGURE 1: Mean bulk density measured at aging day 7.

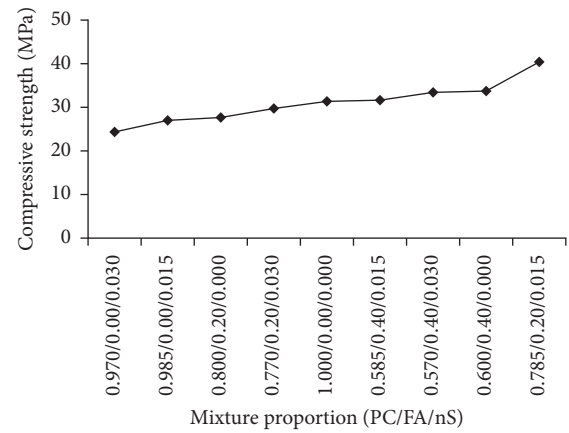


FIGURE 2: Mean compressive strengths measured at aging day 7.

previously to solve engineering and science problems [14, 15]. In this research, we applied the method to find the proportion (or fractional) combinations of a cement mixture that belong to the best possible balances in the presence of the conflicting performance measures, or more formally, the solutions in the Pareto-efficient frontier.

To further demonstrate its straightforwardness, we coded the method in a commercially available spreadsheet program. Utilizing the Pareto-optimality conditions, as aforementioned, we carried out a full pairwise comparison between the solutions to eventually find the Pareto-efficient frontier or the nondominated set. A detailed description of the multiple criteria optimization method utilized in this work can be found in the literature [43].

3. Experimental Results

In this section, we present the experimental results organized for different curing ages. Their graphical representations have been used in the decision-making analysis and the optimization methodology.

3.1. Seven Days of Aging. Table 4 presents the results obtained on aging day 7. One must note that the mean compressive strength was obtained from 6 replicates,

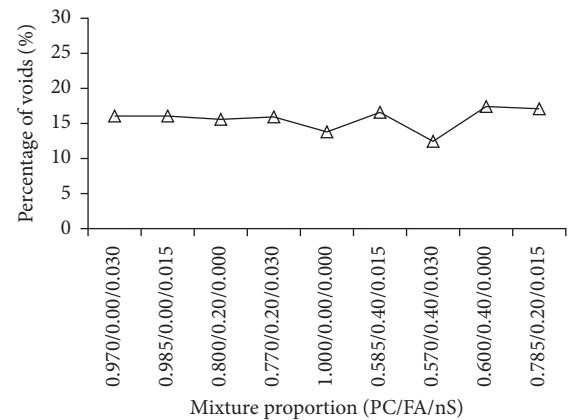


FIGURE 3: Mean percent of voids measured at aging day 7.

whereas the mean bulk density and average percentage of voids were from 5 replicates, due to few experimental flaws. It is apparent that if we consider each one of the performance measures separately, they will aim at different solutions (Figures 1–3). In other words, the performance measures are in conflict. Each one of the mixture combination will represent a solution or alternative k for the multiple criteria optimization problem (Table 4).

TABLE 5: Matrix A_1 compares all the solutions k from objective f_1 .

f_1 versus f_1	37.23	33.49	30.89	33.02	34.85	37.56	40.40	24.19	31.25
37.23	0	1000	1000	1000	1000	-1	-1	1000	1000
33.49	-1	0	1000	1000	-1	-1	-1	1000	1000
30.89	-1	-1	0	-1	-1	-1	-1	1000	-1
33.02	-1	-1	1000	0	-1	-1	-1	1000	1000
34.85	-1	1000	1000	1000	0	-1	-1	1000	1000
37.56	1000	1000	1000	1000	1000	0	-1	1000	1000
40.40	1000	1000	1000	1000	1000	1000	0	1000	1000
24.19	-1	-1	-1	-1	-1	-1	-1	0	-1
31.25	-1	-1	1000	-1	-1	-1	-1	1000	0

TABLE 6: Matrix A_2 compares all the solutions k from objective f_2 .

f_2 versus f_2	2170.43	2117.88	2218.43	2210.75	2149.85	2147.80	2146.33	2179.68	2172.82
2170.43	0	1000	-1	-1	1000	1000	1000	-1	-1
2117.88	-1	0	-1	-1	-1	-1	-1	-1	-1
2218.43	1000	1000	0	1000	1000	1000	1000	1000	1000
2210.75	1000	1000	-1	0	1000	1000	1000	1000	1000
2149.85	-1	1000	-1	-1	0	1000	1000	-1	-1
2147.80	-1	1000	-1	-1	-1	0	1000	-1	-1
2146.33	-1	1000	-1	-1	-1	-1	0	-1	-1
2179.68	1000	1000	-1	-1	1000	1000	1000	0	1000
2172.82	1000	1000	-1	-1	1000	1000	1000	-1	0

TABLE 7: Matrix A_3 compares all the solutions k from objective f_3 .

f_3 versus f_3	15.59	13.85	17.42	16.58	15.93	16.00	16.04	17.00	12.49
15.59	0	1000	-1	-1	-1	-1	-1	-1	1000
13.85	-1	0	-1	-1	-1	-1	-1	-1	1000
17.42	1000	1000	0	1000	1000	1000	1000	1000	1000
16.58	1000	1000	-1	0	1000	1000	1000	-1	1000
15.93	1000	1000	-1	-1	0	-1	-1	-1	1000
16.00	1000	1000	-1	-1	1000	0	-1	-1	1000
16.04	1000	1000	-1	-1	1000	1000	0	-1	1000
17.00	1000	1000	-1	1000	1000	1000	1000	0	1000
12.49	-1	-1	-1	-1	-1	-1	-1	-1	0

Compressive strength, bulk density, and percentage of voids are labeled f_1 , f_2 , and f_3 , respectively. Then, the values of our performance measures, that is, f_1 , f_2 , and f_3 , were utilized to create three matrices A_1 , A_2 , and A_3 in order to compare all the solutions n in each objective.

In order to assess the first Pareto-optimality condition, the following states were employed [14]:

$$A_j(a, b) = \begin{cases} -1, & f_j(x^a) < f_j(x^b) \\ 0, & f_j(x^a) = f_j(x^b) \\ 1000, & f_j(x^a) > f_j(x^b) \end{cases} \quad (1)$$

For example, if $A_1(37.23, 40.40)$ is evaluated, the result will be -1 for the solution; 37.23 is smaller than solution 40.40 (Table 5). In this context, smaller means better because

we are trying to minimize each performance measurement. Then, one can perform the same comparison in each objective for all its solutions (Table 6 and 7).

Now, matrix S is constructed to compare all the objectives and evaluate the second Pareto-optimality condition (Table 8). By this means, one can identify the nondominated solution set using the following conditions:

$$S(a, b) = \begin{cases} 1500, & \sum_{j=1}^3 A_j(a, b) = 0 \\ 1500, & \sum_{j=1}^3 A_j(a, b) = 1000 \\ 1500, & \sum_{j=1}^3 A_j(a, b) = 2000 \\ 3000, & \sum_{j=1}^3 A_j(a, b) \geq 3000 \\ 0, & \text{otherwise} \end{cases} \quad (2)$$

TABLE 8: Matrix S to evaluate the second condition of Pareto.

k	f_1 versus f_2 versus f_3											
1	37.23	2170.43	15.59	1500	3000	0	0	0	0	0	0	0
2	33.49	2117.88	13.85	0	1500	0	0	0	0	0	0	0
3	30.89	2218.43	17.42	0	0	1500	0	0	0	0	3000	0
4	33.02	2210.75	16.58	0	0	0	1500	0	0	0	0	3000
5	34.85	2149.85	15.93	0	3000	0	0	1500	0	0	0	0
6	37.56	2147.80	16.00	0	3000	0	0	0	1500	0	0	0
7	40.40	2146.33	16.04	0	3000	0	0	0	0	1500	0	0
8	24.19	2179.68	17.00	0	0	0	0	0	0	0	1500	0
9	31.25	2172.82	12.49	0	0	0	0	0	0	0	0	1500

TABLE 9: Mixtures in bold belong to the Pareto-efficient frontier for day 7.

k	Mixture proportions (PC/FA/nS)	f_1 MPa	f_2 kg/m ³	f_3 %
1	0.800/0.20/0.000	27.37	2165.88	15.59
2	1.000/0.00/0.000	31.11	2218.43	13.85
3	0.600/0.40/0.000	33.71	2117.88	17.42
4	0.585/0.40/0.015	31.58	2125.56	16.58
5	0.770/0.20/0.030	29.75	2186.46	15.93
6	0.985/0.00/0.015	27.03	2188.51	16.00
7	0.970/0.00/0.030	24.19	2189.98	16.04
8	0.785/0.20/0.015	40.40	2156.64	17.00
9	0.570/0.40/0.030	33.35	2163.49	12.49

Finally, when we sum each row of matrix S , we can identify the solutions that are part of the Pareto-efficient frontier, that is, the sum associated with that row (solution) is less than 3000 (in this case).

After applying the multiple criteria optimization method, Table 9 shows in bold the efficient solutions for aging day 7. These were the mixtures numbered 2, 8, and 9. Mixture number 2 is the control mixture with only Portland cement (no replacement). We expected that this mixture be in the optimal set since its properties were very competitive during its early age. However, we found particularly interesting that the other two mixtures, that is, 8 and 9, that belong to the Pareto-efficient frontier contained FA and nS. Mixture 8 had 78.5% PC, 20% FA, and 1.5% nS, while mixture 9 possessed 57% PC, 40% FA, and 3% nS. Although mixture 9 had 40% of FA (high level of replacement), the addition of only 3% nS makes it a competitive combination with adequate physical and mechanical properties. In contrast, mixture 3 is made of 60% PC, 40% FA, and no nanoparticles (0% nS), which has a high level of replacement; notwithstanding, this mixture does not belong to the Pareto-efficient frontier. Intriguingly, mixture 1 (20% FA and no nS) had a similar behavior. Hence, the difference between *being and not being* part of the Pareto-efficient frontier appeared to be the presence of the silica nanoparticles. This was a consequential finding that is discussed later.

As we analyzed three performance measures, the results yielded the 3D graph in Figure 4. In addition, one can

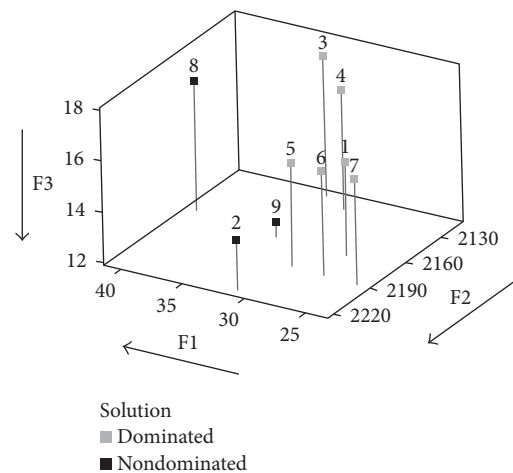


FIGURE 4: Graphical representation of the results of the solution set evaluated at 7 days (rotated view).

employ a cone of Pareto dominance to visualize the dominated and nondominated solutions. Figure 4 shows all the solutions k (mixtures) in the criteria space with a rotated view to make easier the visualization of the efficient frontier.

3.2. Twenty-Eight Days of Aging. Table 10 shows the average results of the three performance measures evaluated at 28 days of aging. Clearly, mixture 8 had a higher compressive strength, whereas mixture 6 bears a larger bulk density and lower percentage of voids. This leads, once again, to a conflict between the objectives.

As in the analysis of day 7, at day 28, we sought to maximize the compressive strength and bulk density and to minimize the percentage of voids. Table 11 presents the results obtained from the multiple criteria optimization strategy, which indicates that four solutions belong to the Pareto-efficient frontier: mixtures 2, 6, 7, and 8. The Pareto-optimality conditions can be used to ensure that these sets of mixtures are always better in at least one objective and the same or worse in the other objective.

We did expect mixture number 2 to be part of the Pareto-efficient frontier since it is the control mixture with only PC. Mixtures 6 and 7 contain PC and 1.5% and 3.0% nS, respectively, without any FA, that is, one of the replacements

TABLE 10: Average result of performance measures at day 28.

k	Mixture proportions (PC/FA/nS)	Compressive strength		Bulk density		Volume of permeable pore space	
		Average MPa	Std. dev. MPa	Average kg/m^3	Std. dev. kg/m^3	Average %	Std. dev. %
1	0.800/0.20/0.000	34.48	5.49	2141.12	52.85	15.77	1.20
2	1.000/0.00/0.000	41.91	9.59	2192.05	42.05	14.75	1.06
3	0.600/0.40/0.000	44.09	2.94	2098.88	19.94	17.26	0.61
4	0.585/0.40/0.015	38.92	9.38	2096.61	45.25	17.17	1.24
5	0.770/0.20/0.030	36.59	5.79	2168.71	27.31	16.06	0.86
6	0.985/0.00/0.015	31.29	3.41	2226.15	28.65	14.25	0.63
7	0.970/0.00/0.030	31.81	4.64	2197.49	22.35	15.35	0.43
8	0.785/0.20/0.015	47.27	6.58	2179.52	12.47	16.12	0.25
9	0.570/0.40/0.030	41.5	3.23	2131.97	18.65	16.02	0.57

TABLE 11: Optimization results at day 28 where the mixtures in bold belong to the Pareto-efficient frontier.

k	Mixture proportions (PC/FA/nS)	f_1 MPa	f_2 kg/m^3	f_3 %
1	0.800/0.20/0.000	34.48	2141.12	15.77
2	1.000/0.00/0.000	41.91	2192.05	14.75
3	0.600/0.40/0.000	44.09	2098.88	17.26
4	0.585/0.40/0.015	38.92	2096.61	17.17
5	0.770/0.20/0.030	36.59	2168.71	16.06
6	0.985/0.00/0.015	31.29	2226.15	14.25
7	0.970/0.00/0.030	31.81	2197.49	15.35
8	0.785/0.20/0.015	47.27	2179.52	16.12
9	0.570/0.40/0.030	41.5	2131.97	16.02

of interest. Conversely, mixture 8, which contains 20% FA (with 78.5% PC and 1.5% nS), is also efficient. The solutions can be observed in the criteria space in Figure 5 with a rotated view for visualization convenience.

4. Discussion of Results

The results obtained from the multiple criteria optimization are the best tradeoff mixtures recommended to the decision-makers who can then select a single mixture among the efficient set presented in this work. Naturally, such a decision should be based on the characteristics of the mixtures presented in each performance measures. Also, they should consider the proportion of each component in the mixture. This depends on the user's (or structural designer's) interest about the mineral admixtures and the specific application of each concrete mixture.

The optimization process revealed that mixtures with FA and no nS did not belong to the Pareto-efficient frontier. This behavior was observed throughout the analysis, denoting that the addition of silica nanoparticles is necessary when FA is presented as cement replacement. This beneficial interaction had already been observed in prior works [4]. In such concretes, the nanoparticles do improve the physical and mechanical properties of the

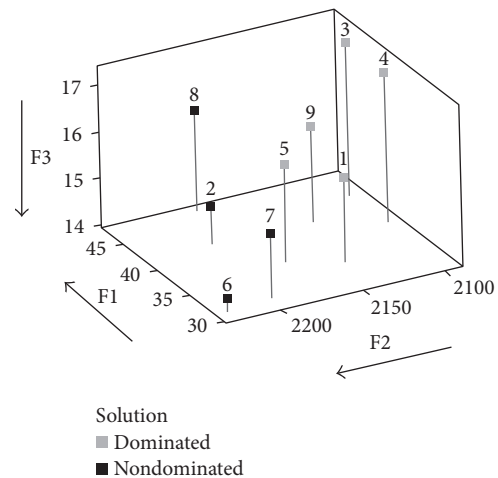


FIGURE 5: Graphical results of the solution set evaluated at 28 days (rotated view).

resulting concrete. Toutanji et al. [44] discovered that a combination of different supplementary materials, as silica fume, increased the compressive strength. Previous works support these findings [17], where the use of FA and nS was found to improve the concrete microstructure and rate of strength gain. Microstructure analysis of concrete by scanning, scanning transmission, and transmission electron microscopy revealed that nS particles fill the CSH-gel structure voids and act as nuclei, tightly bonded with the CSH particles [45]. This tight packing densifies concrete, protecting it from chemical attacks and leaching, while enhancing its durability and mechanical properties.

As aforementioned, after seven days of aging, there were three efficient mixtures. In the analysis at day 28, the efficient mixtures were four. Examining this pool of efficient mixtures reveals that two were efficient in all the analysis conducted: (a) the control mixture with 100% PC, 0% FA, and 0% nS and (b) the mixture with 78.5% PC, 20% FA, and 1.5% nS. In other words, for the two ages tested, the regular mix (control) can be replaced by mixture 8, which even has higher compression strength at the expense of a slight increase in porosity. This result further proves how

nanosilica can counteract some strength loss induced by the FA presence [2, 5, 17, 46]. This is an important finding as it points to the formulation of a sustainable concrete, that is, one that requires less cement to attain structural behavior, using an industrial waste, that is, fly ash and nanostructured SiO₂ particles. In effect, less consumption of cement would lead to a smaller carbon footprint upon its fabrication, without compromising the structural strength of the mixture.

However, the cost of large amounts of nS, as a construction project would demand, poses an economic challenge. On the other hand, FA is one of the low-priced mineral admixtures, which could balance the final cost of concrete. Therefore, to finally propose the use of nS and FA in structural concrete, we deem critical to an optimization strategy that includes an exhaustive cost analysis.

Finally, the full pairwise comparison between solutions that led us to the Pareto-efficient frontier was implemented in a readily available spreadsheet package. This means that no computational intricacy was required to render a robust analysis of the data to assist in the decision-making process. We recognize that the multiple criteria optimization method, in our case, studied only three material characteristics, that is, compressive strength, density, and void presence. Concrete is a versatile material with numerous potential variables arising from its fabrication process. Nonetheless, the multiple criteria optimization method is a versatile and scalable strategy that could be expanded to include other performance measures more relevant to other specific applications of concrete mixtures.

5. Conclusions

The present work proposes the use of an optimization procedure to determine for nanosilica-containing concrete mixtures the best ones to achieve specific performance measures: concrete compressive strength, bulk density, and percentage of voids (porosity). These performance measurements were measured after 7 and 28 days. The nine proportion combinations evaluated contained different percentages of PC, FA, and nS. The use of the multiple criteria optimization helped find the mixtures that were the best balances among the studied objectives. At day 7, three mixtures were part of the Pareto-efficient frontier. Two of them were mixtures with cement replacement, that is, FA and nS at different levels. On the other hand, four mixtures were part of the Pareto-efficient frontier at day 28. This time, one mixture has cement replacement (FA and nS). In addition, two mixtures were efficient at either day 7 or day 28.

As a consequence, the multiple criteria optimization strategy permitted to recommend the use of FA and nS to improve the concrete properties. However, if the analysis is performed considering only one performance measurement, such as compressive strength, the option of cement replacement by FA is not recommended. Hence, taking into consideration several performance measurements, the use of mineral admixtures is suggested. This is because a mixture with mineral admixtures will be equally

optimal than a control mixture with just PC when more properties are considered. Consequently, as the decision-makers know the best tradeoff mixtures for an individual application, the final recommendation is easier to make.

Conflicts of Interest

The authors declare that they have no conflicts of interest.

Acknowledgments

This material is based upon the work supported by the National Science Foundation under Grants nos. HRD 0833112 and 1345156 (CREST program). Additional support was provided by the US Department of Education through Grant no. P120A120097 (MSEIP program). The authors would like to thank the technical personnel of the Nanotechnology Center and the Construction Materials Laboratory of the University of Puerto Rico for their invaluable assistance in the completion of this work.

References

- [1] J. Oliver-Sola, A. Josa, J. Rieradevall, and X. Gabarrell, "Environmental optimization of concrete sidewalks in urban areas," *International Journal of Life Cycle Assessment*, vol. 14, no. 4, pp. 302–312, 2009.
- [2] L. E. Zapata, G. Portela, O. M. Suárez, and O. Carrasquillo, "Rheological performance and compressive strength of superplasticized cementitious mixtures with micro/nano-SiO₂ additions," *Construction and Building Materials*, vol. 41, pp. 708–716, 2013.
- [3] N. M. García, L. E. Zapata, O. M. Suárez, and M. Cabrera-Ríos, "Effect of fly ash and nanosilica on compressive strength of concrete at early age," *Advances in Applied Ceramics*, vol. 114, no. 2, pp. 99–106, 2015.
- [4] L. E. Zapata-Ordúz, G. Portela, and O. M. Suárez, "Tensile behavior by Weibull analysis in binary, ternary, and quaternary concretes designed with micro and nano-silica additions," in *Maintenance, Monitoring, Safety, Risk and Resilience of Bridges and Bridge Networks*, pp. 1254–1261, CRC Press, Boca Raton, FL, USA, 2016.
- [5] L. E. Zapata-Ordúz, G. Portela, and O. M. Suárez, "Weibull statistical analysis of splitting tensile strength of concretes containing class F fly ash, micro/nano-SiO₂," *Ceramics International*, vol. 40, no. 5, pp. 7373–7388, 2014.
- [6] G. Shakhmenko, I. Juhnevica, and A. Korjajins, "Influence of sol-gel nanosilica on hardening processes and physically-mechanical properties of cement paste," *Procedia Engineering*, vol. 57, pp. 1013–1021, 2013.
- [7] J. G. Cabrera, P. A. Claisse, and D. N. Hunt, "Measurement of porosity as a predictor of the durability performance of concrete with and without condensed silica fume," *Advances in Cement Research*, vol. 13, no. 4, pp. 165–174, 2001.
- [8] L. Basheer, J. Kropp, and D. J. Cleland, "Assessment of the durability of concrete from its permeation properties: a review," *Construction and Building Materials*, vol. 15, no. 2-3, pp. 93–103, 2001.
- [9] C. Lian, Y. Zhuge, and S. Beecham, "The relationship between porosity and strength for porous concrete," *Construction and Building Materials*, vol. 25, no. 11, pp. 4294–4298, 2011.

- [10] I. Kaur and R. Siddique, *Mechanical Properties of High Volume Fly Ash (HVFA) Concrete Subjected to Elevated Temperatures up to 120°C*, M.E. thesis, Thapar Institute of Engineering & Technology University, Patiala, India, 2005.
- [11] P. Lawrence, M. Cyr, and E. Ringot, "Mineral admixtures in mortars effect of type, amount and fineness of fine constituents on compressive strength," *Cement and Concrete Research*, vol. 35, no. 6, pp. 1092–1105, 2005.
- [12] J. Sunku, "Advantages of using fly ash as supplementary cementing material (SCM) in fibre cement sheets," in *Proceedings of 10th International Inorganic-bonded Fiber Composites Conference*, pp. 25–32, São Paulo, Brazil, November 2006.
- [13] R. S. Ravindrarajah, "Bleeding of fresh concrete containing cement supplementary materials," in *Proceedings of 9th East Asia-Pacific Conference on Structural Engineering and Construction*, pp. 16–18, Bali, Indonesia, December 2003.
- [14] C. J. Burgos, J. M. Pizarro, K. I. Camacho-Cáceres, and M. Cabrera-Ríos, "A visual basic tool for multiple criteria optimization," in *Proceedings of the 2014 Industrial and Systems Engineering Research Conference*, Montreal, Canada, November 2014.
- [15] B. Rodríguez-Yañez, Y. M. Méndez-Vázquez, and M. Cabrera-Ríos, "Simulation-based process windows simultaneously considering two and three conflicting criteria in injection molding," *Production & Manufacturing Research*, vol. 2, no. 1, pp. 603–623, 2014.
- [16] D. Jato-Espino, E. Castillo-Lopez, J. Rodriguez-Hernandez, and J. C. Canteras-Jordana, "A review of application of multi-criteria decision making methods in construction," *Automation in Construction*, vol. 45, pp. 151–162, 2014.
- [17] L. E. Zapata Orduz, *Rheological and Mechanical Characterization of Portland Cement Mixes Containing Micro and Nano Amorphous Silica Particles*, Ph.D. dissertation, University of Puerto Rico, Mayaguez, PR, USA, 2013.
- [18] A. Baykasoğlu, A. Öztaş, and E. Özbay, "Prediction and multi-objective optimization of high-strength concrete parameters via soft computing approaches," *Expert Systems with Applications*, vol. 36, no. 3, pp. 6145–6155, 2009.
- [19] K. S. Kulkarni, S. C. Yaragal, and K. S. Babu Narayan, "An overview of high performance concrete at elevated temperatures," *International Journal of Applied Engineering and Technology*, vol. 1, pp. 48–60, 2011.
- [20] E. Ghafari, H. Costa, E. Júlio, A. Portugal, and L. Durães, "The effect of nanosilica addition on flowability, strength and transport properties of ultra high performance concrete," *Materials & Design*, vol. 59, pp. 1–9, 2014.
- [21] M. A. Hassanain and R. E. Loov, "Cost optimization of concrete bridge infrastructure," *Canadian Journal of Civil Engineering*, vol. 30, no. 5, pp. 841–849, 2003.
- [22] C. Perea, I. Payá, V. Yepes, and F. González, "Heuristic optimization of reinforced concrete building frames," in *Proceedings of the 2nd International FIB Congress*, p. 9, Naples, Italy, June 2006.
- [23] M. Anson-Cartwright, *Optimization of Aggregate Gradation Combinations to Improve Concrete Sustainability*, M.S. Thesis, University of Toronto, Toronto, ON, Canada, 2011.
- [24] O. Akalin, K. U. Akay, B. Sennaroglu, and M. Tez, "Optimization of chemical admixture for concrete on mortar performance tests using mixture experiments," *Chemometrics and Intelligent Laboratory Systems*, vol. 104, no. 2, pp. 233–242, 2010.
- [25] E. M. R. Fairbairn, M. M. Silvano, R. D. Toledo Filho, J. L. D. Alves, and N. F. F. Ebecken, "Optimization of mass concrete construction using genetic algorithms," *Computers & Structures*, vol. 82, no. 2-3, pp. 281–299, 2004.
- [26] A. Rudy and J. Olek, "Optimization of mixture proportions for concrete pavements—influence of supplementary cementitious materials, paste content and aggregate gradation, joint transportation research program," FHWA/IN/JTRP-2012/34, Indiana Department of Transportation and Purdue University, West Lafayette, IN, USA, 2012.
- [27] B. Şimşek, Y. T. İç, and E. H. Şimşek, "A TOPSIS-based Taguchi optimization to determine optimal mixture proportions of the high strength self-compacting concrete," *Chemometrics and Intelligent Laboratory Systems*, vol. 125, pp. 18–32, 2013.
- [28] M. F. Ghazy and M. F. A. El Hameed, "Optimization of lightweight concrete process by Gray-Taguchi method," *ACI Materials Journal*, vol. 112, no. 3, pp. 365–374, 2014.
- [29] S. Barakat, K. Bani-Hani, and M. Q. Taha, "Multi-objective reliability-based optimization of prestressed concrete beams," *Structural Safety*, vol. 26, no. 3, pp. 311–342, 2004.
- [30] X. K. Zou, C. M. Chan, G. Li, and Q. Wang, "Multiobjective optimization for performance-based design of reinforced concrete frames," *Journal of Structural Engineering*, vol. 133, no. 10, pp. 1462–1474, 2007.
- [31] K. Deb, *Multi-Objective Evolutionary Optimisation for Product Design and Manufacturing*, L. Wang, A. Ng, and K. Deb, Eds., pp. 1–24, Springer, London, UK, 2011.
- [32] ASTM Standard C136, *Standard Test Method for Sieve Analysis of Fine and Coarse Aggregates*, vol. 14, pp. 1–5, ASTM International, West Conshohocken, PA, USA, 2001.
- [33] ASTM Standard C33, *Standard Specification for Concrete Aggregates*, p. 11, ASTM International, West Conshohocken, PA, USA, 2003.
- [34] ASTM Standard C143, *Standard Test Method for Slump of Hydraulic-Cement Concrete*, pp. 1–4, ASTM International, West Conshohocken, PA, USA, 2005.
- [35] ASTM Standard C150/C150M-12, *Standard Specification for Portland Cement*, p. 9, ASTM International, West Conshohocken, PA, USA, 2012.
- [36] ASTM Standard C618-12a, *Standard Specification for Coal Fly Ash and Raw or Calcined Natural Pozzolan for Use in Concrete*, p. 5, ASTM International, West Conshohocken, PA, USA, 2012.
- [37] ASTM Standard C494/C494M-13, *Standard Specification for Chemical Admixtures for Concrete*, p. 10, ASTM International, West Conshohocken, PA, USA, 2013.
- [38] ASTM Standard C192/C192M–13a, *Standard Practice for Making and Curing Concrete Test Specimens in the Laboratory*, pp. 1–8, ASTM International, West Conshohocken, PA, USA, 2013.
- [39] ASTM Standard C642, *Standard Test Method for Density, Absorption, and Voids in Hardened Concrete*, pp. 4–6, ASTM International, West Conshohocken, PA, USA, 2013.
- [40] ASTM Standard C39, *Standard Test Method for Compressive Strength of Cylindrical Concrete Specimens*, pp. 1–8, ASTM International, West Conshohocken, PA, USA, 2004.
- [41] R. H. Myers and D. Montgomery, *Response Surface Methodology*, John Wiley and Sons, Danvers, MA, USA, 2002.
- [42] M. L. Sánchez-Peña, C. E. Isaza, J. Pérez-Morales, C. Rodríguez-Padilla, J. M. Castro, and M. Cabrera-Ríos, "Identification of potential biomarkers from microarray experiments using multiple criteria optimization," *Cancer Medicine*, vol. 2, no. 2, pp. 253–265, 2013.
- [43] K. I. Camacho, *Optimization-Driven Meta-Analysis: The Simultaneous Search for Cancer Biomarkers with Multiple*

- Microarray Experiments*, M.S. thesis, University of Puerto Rico, Mayagüez, PR, USA, 2014.
- [44] H. Toutanji, N. Delatte, S. Aggoun, R. Duval, and A. Danson, "Effect of supplementary cementitious materials on the compressive strength and durability of short-term cured concrete," *Cement and Concrete Research*, vol. 34, no. 2, pp. 311–319, 2004.
- [45] G. Quercia and H. J. H. Brouwers, "Application of nano-silica (nS) in concrete mixtures," in *Proceedings of 8th fib International Ph.D. Symposium in Civil Engineering*, pp. 1–6, Kongens Lyngby, Denmark, June 2010.
- [46] L. E. Zapata Orduz, G. Portela, O. M. Suárez, and A. D. Cáceres, "Compatibility analysis between Portland cement type I and micro/nano-SiO₂ in the presence of polycarboxylate-type superplasticizers," *Cogent Engineering*, vol. 3, no. 1, pp. 1–18, 2016.